

**TESI DI DOTTORATO IN INGEGNERIA AEROSPAZIALE, NAVALE E DELLA QUALITÀ
CICLO XX**

**An improved data reduction technique for heat transfer
measurements in hypersonic flows**

Gennaro dello Ioio



**DIAS, Facoltà di Ingegneria
UNIVERSITÀ DEGLI STUDI DI NAPOLI "FEDERICO II"
Napoli, Italia 2008**

**TESI DI DOTTORATO IN INGEGNERIA AEROSPAZIALE, NAVALE E DELLA QUALITÀ
CICLO XX**

**An improved data reduction technique for heat transfer
measurements in hypersonic flows**

GENNARO DELLO IOIO

Il presente lavoro è stato svolto presso il laboratorio di gasdinamica del Dipartimento di Ingegneria Aerospaziale della Facoltà di Ingegneria.

UNIVERSITÀ DEGLI STUDI DI NAPOLI “FEDERICO II”

TUTORI: **PROF. ING. GENNARO CARDONE**
 PROF. ING. GIOVANNI MARIA CARLOMAGNO

COORDINATORE: **PROF. ING. ANTONIO MOCCIA**

Napoli, 2008

Table of Contents

INTRODUCTION	1
CHAPTER 1: INFRARED THERMOGRAPHY	3
1.1 Principles of radiative heat transfer	3
1.2 IR detectors and their characteristics	7
1.3 Scanning methods	10
1.3.1 Opto-mechanical systems	10
1.3.2 Focal Plane Array	11
1.4 Distinguishing characteristics of thermographs	13
1.5 Thermographs used in this work	15
1.6 Thermograph calibration	17
1.7 Emissivity calculation	21
CHAPTER 2: THE PINHOLE MODEL	23
2.1 The Tsai algorithm	24
2.1.1 The pinhole model	24
2.1.2 The advantages of a versatile calibration technique	25
2.1.3 Introduction to the calibration algorithm	26
2.1.4 The Transformation from the “object” reference frame to the “image” reference frame	27
2.1.5 The set of calibration constants	32
2.2 The calibration process	33
CHAPTER 3: HEAT FLUX SENSOR	35
3.1 Heat flux measurements	35
3.2 Thin film sensor	36
3.2.1 Numerical solution	38
3.3 Limits of the thin film sensor	39
3.4 New heat flux sensor	41
3.4.1 Mathematical model	41
3.4.2 Iterative method	43
3.4.3 Optimization methods	44
3.5 Dimensional analysis	46
3.5.1 Acceptable limits for adimensional parameters	48
3.6 Numerical validation	50
3.6.1 Method	51
3.6.2 Type and intensity of noise	53
3.6.3 Error parameters	54
3.6.4 Sampling rate	55
3.7 Results: two-parameter optimization	56
3.8 Results: one-parameter optimization	63

3.9	Conclusions.....	69
CHAPTER 4: EXPERIMENTAL ANALYSIS – CAST TC-1A.....		71
4.1	Introduction: the CAST Project and the Test Case TC-1a.....	71
4.2	Hypersonic double cone flow	72
4.3	Experimental apparatus.....	74
	4.3.1 The HEAT facility	74
	4.3.2 The thermograph.....	75
4.4	Test article design	77
	4.4.1 Geometry.....	77
	4.4.2 Material.....	78
4.5	Design of the target.....	80
4.6	The test campaign	82
4.7	Experimental problems	83
4.8	Transient temperature measurement	85
4.9	Heat flux measurement	89
4.10	Results.....	91
	4.10.1 Temperature maps.....	91
	4.10.2 Heat flux maps	94
	4.10.3 Time history temperature diagrams	97
4.11	Comparison with literature.....	103
4.12	Comparison with thin film	106
4.13	Conclusions.....	108
CHAPTER 5: EXPERIMENTAL ANALYSIS – CLAE EXPERT		109
5.1	Introduction: The EXPERT Program.....	109
5.2	Experimental apparatus.....	110
	5.2.1 The “Scirocco” Plasma Wind Tunnel.....	110
	5.2.2 The thermograph.....	111
5.3	Test article design	112
	5.3.1 Geometry.....	112
	5.3.2 Materials.....	112
5.4	Design of the target.....	115
5.5	The test.....	117
5.6	Transient temperature measurement	118
5.7	Heat flux measurement	121
5.8	Results.....	122
	5.8.1 Temperature maps.....	122
	5.8.2 Heat flux maps	125
	5.8.3 Time history temperature diagrams	128
5.9	Conclusions.....	130

CONCLUSION	131
APPENDIX 1: NUMERICAL SOLUTION OF THE HEAT CONDUCTION EQUATION	134
APPENDIX 2: BUCKINGHAM π -THEOREM	137
APPENDIX 3: DESCRIPTION OF THE CODE	138
BIBLIOGRAPHY	139

INTRODUCTION

The re-entry phase is one of the most critical phases in the lifetime of most space missions. When the spacecraft comes into contact with the atmosphere, it is exposed to intense stresses, both mechanical and thermal. The experimental analysis of this phase is therefore of primary importance for the design of spacecrafts and for the dimensioning of thermal protection systems. High enthalpy wind tunnels are designed to simulate the extreme conditions and the complex flow phenomena which develop during re-entry.

It is therefore understood how the measurement of heat fluxes is one of the crucial goals of the tests in high enthalpy wind tunnel. The measurement of heat fluxes generally is not made directly but starting from transient temperature measurements on the surface of the model; as such, this is a typical inverse problem and usually implies great sensitivity to measurement errors.

The purpose of this work has been to develop a new heat flux sensor to improve the accuracy and stability of the sensors currently used, and it is based on the minimization of the functional of the sum of the mean square errors between temperature transients measured experimentally and temperature transients generated by the numerical solution of the heat conduction equation inside the model, through an optimization process in which the physical parameters h and T_{aw} , on which the temperature rise depends, are estimated.

Experimental temperature measurements are performed by means of infrared thermography. To increase the accuracy of thermographic measurements, a new method of optical/geometrical reconstruction has been developed. This method allows to identify with precision the point on the three-dimensional surface of the model on the IR image, and it also permits to take directional emissivity into account to improve the accuracy of the thermographic measurements.

In chapter one a general introduction on infrared thermography is given, and the reason why a geometrical reconstruction technique is desirable is made clear. The resection technique, based on the well established pinhole camera model, is subsequently explained in chapter two.

The new heat flux sensor is illustrated in chapter three; the limits of the classical thin film, the most widely used heat flux sensor, are highlighted and the mathematical model on which the new sensor is based is explained. A full numerical validation of the sensor and of its limits of applicability has been performed showing that the sensor, in its one-parameter estimation form, can be used in a wide variety of test conditions.

The experimental implementation, both of the new geometrical reconstruction technique and of the new heat flux sensor, is illustrated in chapter 4 and 5. The experiments in chapter 4 have been performed in Alta's HEAT wind tunnel on a double cone model. This is a classical test for which both previous experimental results and numerical simulations are available. It has infact been designed *ad hoc* for the purpose of code validation within the CAST project.

The test illustrated in chapter five has been performed in CIRA's Scirocco wind tunnel. The purpose of the test was to investigate the shock wave boundary layer interaction on a full-scale model of EXPERT 20deg flap. The materials used in the test are those intended to be used on the capsule itself.

The two test cases illustrated in this work have provided a good initial experimental validation for the new heat flux sensor and have shown that it can be successfully used, coupled with the implemented geometrical reconstruction technique, both in test cases designed *ad hoc* and in simulations of real life models, which do not require any preliminary preparation for the sensor to be used.

CHAPTER 1: INFRARED THERMOGRAPHY

Infrared thermography is a technique of temperature measurement from the distance. This measurement is performed by the infrared camera (or thermograph), which is an instrument capable to perform fully two-dimensional measurements of the radiation emitted in a band of the infrared spectrum by the surface of a body (opaque in that band) and to convert it in an electronic signal. As a matter of fact, the energy radiated by the body passes through an interposed fluid (air, for example), then passes through a system of lenses, a filter, and it finally reaches the thermal sensor which is responsible of the transduction into an electronic signal. When surface emissivity of the body is known, it possible to associate the radiation map to a temperature map with the help of a calibration diagram.

Nowadays the infrared systems for scientific applications are mostly used in conjunction with personal computers both for the visualization of the 2D measurements and for their quantitative analysis. The electronic signal produced by the sensor is therefore elaborated by a dedicated hardware which outputs the results in the form of computer files containing general information about the scanning conditions and the camera and the intensity of radiation for each point of the two-dimensional radiation map. These files are called IR images or thermograms, and dedicated software can subsequently be used to visualize them or for specific further elaboration, as in the case of this work.

Modern thermographs for qualitative measurements make wide use of FPA sensors (see §1.3.2), and the thermograms can be usually visualized directly on the thermograph.

Since IR thermography is based on the measurement of emitted radiation, basic principles of radiative heat transfer are illustrated in the next paragraph; infrared systems and their characteristic will subsequently be described and, in the end of the chapter, the important practical aspects of the calibration of the thermograph and of the calculation of surface emissivity will be illustrated.

1.1 Principles of radiative heat transfer

It is known that all bodies radiate energy in the form of electromagnetic waves and that the emission spectrum, which is the evolution of emitted energy as a function of wavelength, depends on temperature and on the characteristics of the surfaces of the bodies.

The laws which describe this emission spectrum make use of the concept of blackbody. The blackbody is a body that emits and absorbs the maximum possible amount of radiation at any given wavelength and it represents a theoretical concept that sets an upper

limit to the emission of radiation in accordance with the second law of thermodynamics. The energy emitted by a blackbody is given by Planck's law

$$E_{\lambda_0}(T) = \frac{C_1}{\lambda^5 (e^{C_2/\lambda T} - 1)} \quad (1.1)$$

where $E_{\lambda_0}(T)$, measured in $Wm^{-2}\mu m^{-1}$, is the monochromatic emissive power of a blackbody at absolute temperature T at the wavelength λ , and C_1 and C_2 are the first and second radiation constants:

$$\begin{cases} C_1 = 2\pi^5 \hbar c^2 = 3.74 \times 10^8 [W\mu m^4 m^{-2}] \\ C_2 = \frac{\hbar c}{k} = 1.44 \times 10^4 [\mu m K] \end{cases} \quad (1.2)$$

Planck's law is shown in figure 1.1.

The total energy emitted by a blackbody is the integral of (1.1) over the entire wavelength spectrum and is expressed by Stefan-Boltzmann law:

$$E_0 = \int_0^{\infty} E_{\lambda_0}(T) \cdot d\lambda = \sigma T^4 \quad (1.3)$$

where $\sigma = 5.76 \times 10^{-8} [Wm^{-2}K^{-4}]$ is the Stefan-Boltzmann constant.

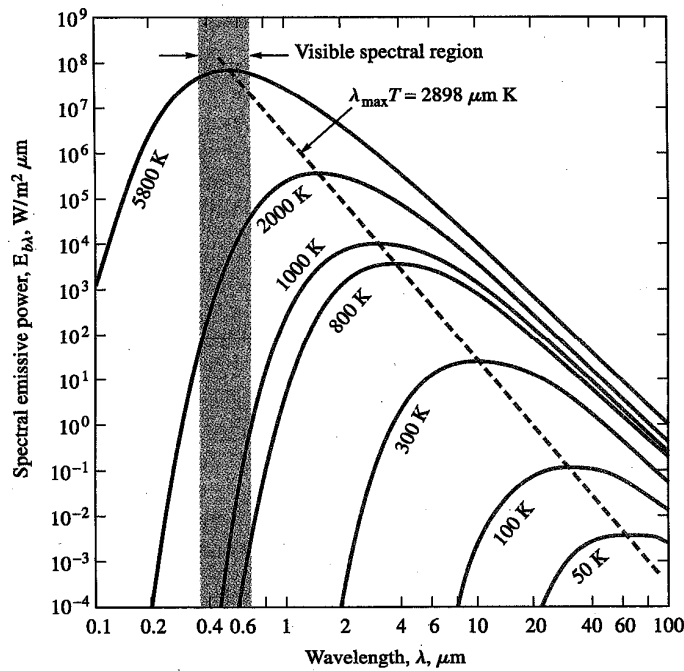


Figure 1.1: Monochromatic blackbody emissive power

Wien's displacement law relates the wavelength λ_{max} at which maximum temperature is emitted with the temperature itself:

$$\lambda_{max} \cdot T = 2,898 \mu m K.$$

This relation shown that at ambient temperature $\lambda_{\max} \cong 10\mu m$.

Real bodies generally emit only a fraction of the energy emitted by a blackbody at the same temperature (figure 1.2); this fraction is expressed by the monochromatic hemispherical emissivity ε_λ , which depends on the surface of the body, on its temperature and wavelength, on the direction of emission and so on. Equations (1.1) and (1.3) therefore become

$$E_\lambda = \varepsilon_\lambda E_{\lambda_0}(T) = \frac{\varepsilon_\lambda C_1}{\lambda^5 (e^{C_2/\lambda T} - 1)}$$

and

$$E = \int_0^\infty \varepsilon_\lambda \cdot E_{\lambda_0}(T) \cdot d\lambda.$$

A body characterized by an ε_λ independent of the wavelength is called gray body. A gray body emits at every wavelength always the same fraction of the energy emitted by a blackbody. For a gray body

$$E = \varepsilon \sigma T^4 \tag{1.4}$$

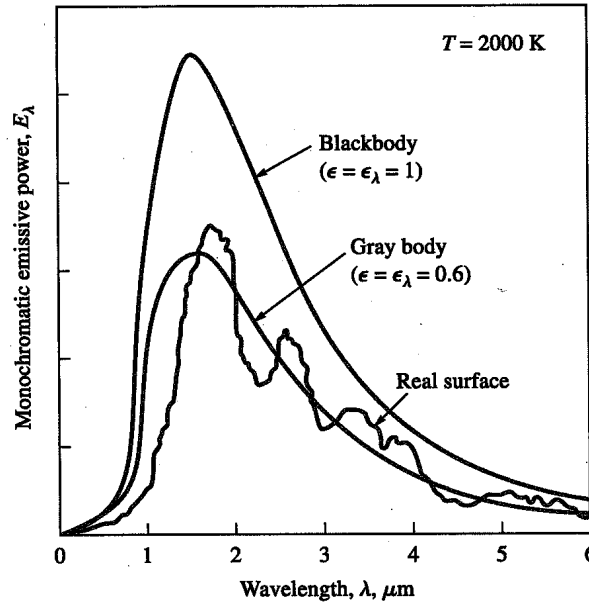


Figure 1.2: Comparison of hemispherical monochromatic emission for a blackbody, a gray body and a real surface

It is important to point up that the emissivity ε characterizes all real surfaces. It must be therefore known and given in input to the thermograph in order to measure surface temperatures. It is also important to notice that ε depends on the angle of view θ and it decreases dramatically when θ becomes higher than about 60° (see figure 1.3).

This considerations imply that in experiments it is often needed to perform a calibration process on the actual test model to characterize its emissivity. This calibration is described in paragraph 1.6.

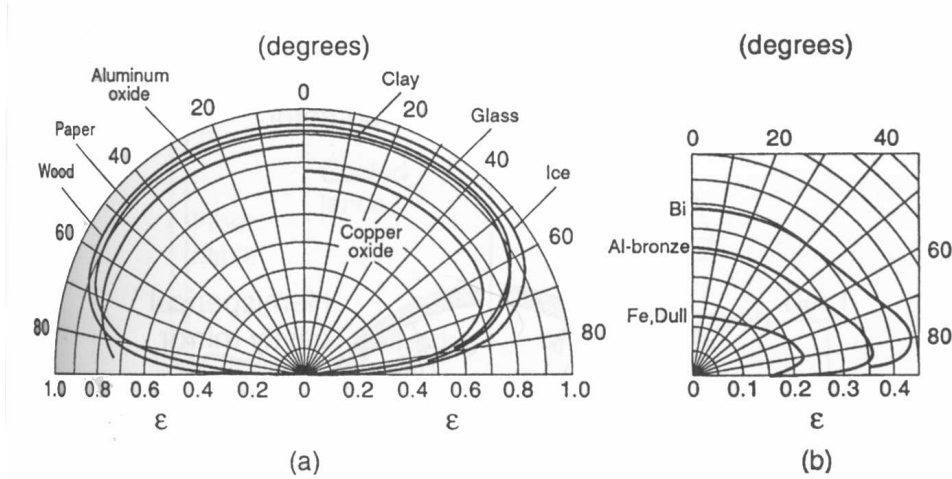


Figure 1.3: Directional emissivity for various materials

The sensor of a thermograph is usually sensitive only to a limited band of the infrared, therefore the measurements basically follow Planck’s law. The infrared band has wavelength comprised between 0.72 and 1,000 μm and is usually subdivided in four zones:

- Near IR, with radiation wavelength comprised between 0.75 and 3 μm ;
- Intermediate IR, with radiation wavelength comprised between 3 and 6 μm ;
- Far IR, with radiation wavelength comprised between 6 and 15 μm ;
- Extreme IR μm , with radiation wavelength comprised between 15 and 1000 μm

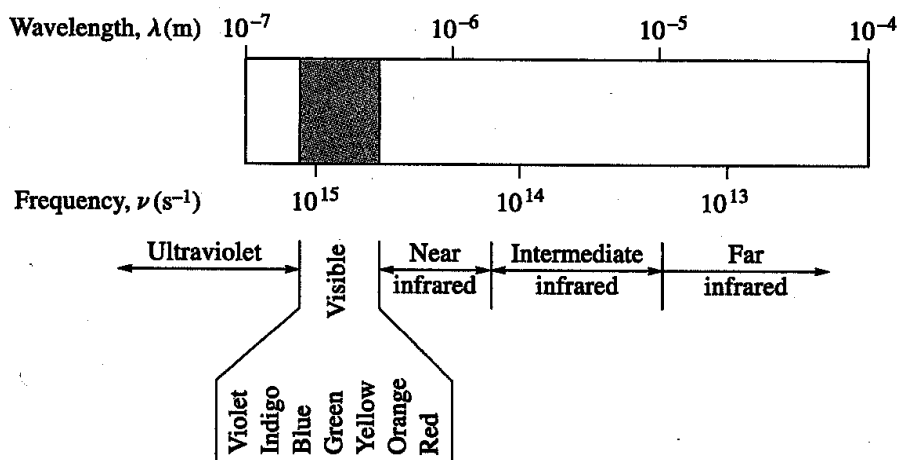


Figure 1.4: Electromagnetic spectrum and thermal radiation portion of the electromagnetic spectrum

1.2 IR detectors and their characteristics

The purpose of the infrared detector is to transform the electromagnetic radiation they absorb in an electric signal. There are two main families of sensors: thermal detectors and photon detectors.

Thermal detectors used to be the most widespread and they are based on the variation of electrical resistance of a film of semiconductor when it is hit by an incident radiation. The main characteristics of this family of detectors are a flat output signal, which can be considered practically constant in a large band of wavelengths, and response times relatively long when compared to photon detectors. The signal P emitted by a thermal detector may be considered proportional to the input radiative power:

$$P(T) = \int_{\lambda_c}^{\lambda_c + \Delta\lambda} E_\lambda(T) \cdot \varepsilon_\lambda(T, \beta) \cdot R(\lambda) \cdot d\lambda \quad (1.5)$$

where $R(\lambda)$ is the response of the instrument, β is the angle of view between sensor and radiating surface and $\Delta\lambda$ the sensitivity band of the instrument.

In the hypothesis of gray body, equation (1.5) becomes:

$$P(T) = \varepsilon(\beta) \cdot \int_{\lambda_c}^{\lambda_c + \Delta\lambda} E_\lambda(T) \cdot R(\lambda) \cdot d\lambda = \varepsilon(\beta) \cdot P_0(T)$$

where $P_0(T)$ is the signal obtained by a blackbody at the same temperature

Photon detectors are instead characterized by semiconductors which emit a number of electrons directly proportional to incident radiating energy. The incident photons are captured by the detector and converted into a variation of electrical potential in the case of photoconductive detectors, and in a variation of electrical resistance in the case of photovoltaic detectors. The energy of the photons is inversely proportional to their associated wavelength and the disappearance of photoelectric activity at wavelengths higher than the "cut off" wavevavelength λ_c indicates that in this case the energy associated with photons is not sufficient to generate the emission of electrons. Photons must therefore have an energy higher than the so called *forbidden energy gap* E_g characteristic of each semiconductor. The cut off frequency is given by

$$\lambda_c = \frac{hc}{E_g} \quad (1.6)$$

where E_g is expressed in Joule.

In general E_g is low at ambient temperature and increases as temperature decreases. This is the reason why these sensor need to be cooled and must operate at very low temperatures (usually of the order of 75 K), see figure 1.6).

The energy associated to a single photon at a given wavelength is $Q = \hbar c / \lambda$, so the total number of emitted photons is obtained dividing equation (1.1) by Q to obtain the number N_{λ_0} of emitted photons at a single wavelength and integrating over the whole spectrum to obtain:

$$N_0 = \int_0^{\infty} N_{\lambda_0} \cdot d\lambda = \frac{0.37}{k} \cdot \sigma \cdot T^3 \quad (1.7)$$

which has dimensions of $photons \cdot cm^2 s^{-2}$ and expresses the dependence of blackbody total emission from the cube of temperature.

Almost all infrared detectors are sensitive only to a limited wavelength band; the integral in equation (1.7) needs therefore be calculated not in $(0, \infty)$ but in $(\lambda_c, \lambda_c + \Delta\lambda)$, which is of course the sensitivity band of the sensor. Thermographs work in the majority of cases in air and, as a consequence, the sensitivity bands used for infrared sensors are those in which the transmittance of air is highest. Under this point of view, two main bands (or "windows") are recognized and commonly used for IR detectors (see figure 1.5): the *short wave band* and the *long wave band*.

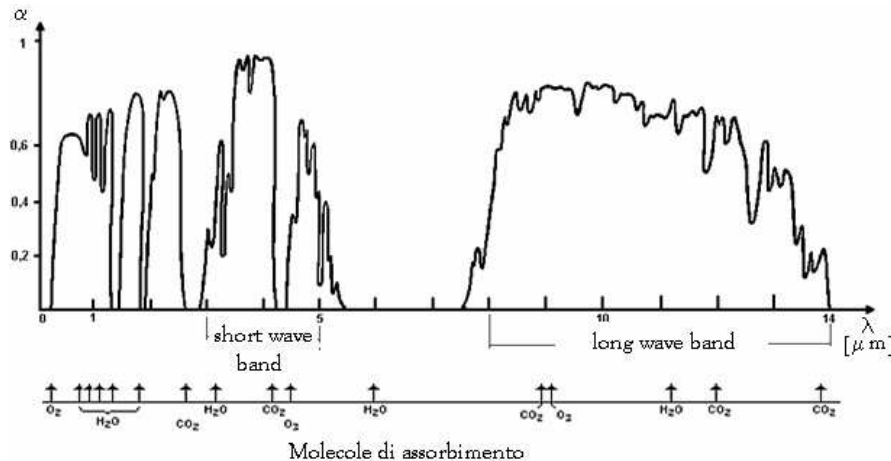


Figure 1.5: Transmittance of air

Several materials are used in the realization of IR detectors. The most widely used in the short wave band are Indium Antimonide (InSb) and Platinum Silicide (PtSi), while in the long wave band Mercury-Cadmium-Tellurite (MCT or HgCdTe) and Gallium Arsenide

(GaAs) are worth mentioning. Figure 1.6 reports shows the spectral response for these and other detectors.

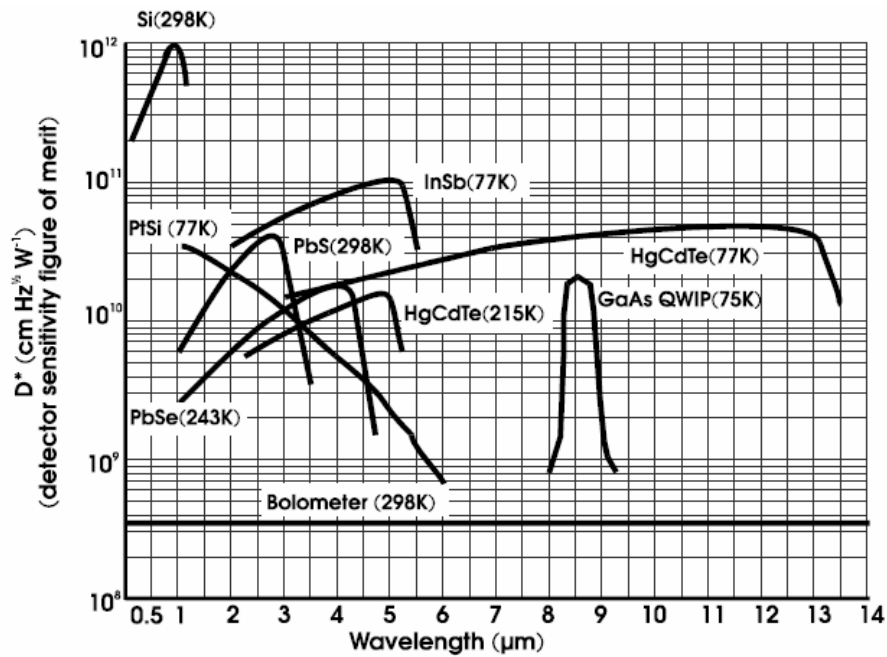


Figure 1.6: Spectral response for various detectors

The choice of operative wavelength, hence of the thermograph with the appropriate sensor, depends on several factors, the most important of which is related with the transmittance of the fluid in which the surface under exam is immersed. As mentioned, this is usually air but several applications are not done in air, most notably the application of this work described in chapter 5 must take into account the transmittance of the plasma present in CIRA's Scirocco wind tunnel¹. In air, longer wavelengths are preferred when the distance between sensor and body is high, because the presence of water vapour can create problems in the short-wave window. Another important factor to be considered is the surface emissivity coefficient, which for some materials is higher at shorter wavelengths.

¹ For a comprehensive analysis of the characteristics of plasmas in high enthalpy wind tunnels and of the associated appropriate choice of thermographs, see Cardone (2007).

1.3 Scanning methods

As already highlighted several times, thermographs perform full two-dimensional measurements of the surfaces under exam. In order to investigate the whole field two different systems are used: when the thermograph uses a single sensitive element, an opto-mechanical system is needed to let radiation emitted by different points of the surface hit the sensor. Modern cameras make instead use of the so called Focal Plane Array (FPA), in which thousands of detectors are situated on a square array; with this arrangement each detector measures radiation from a portion of the field of view and no additional device is needed to measure the whole field of view.

1.3.1 Opto-mechanical systems

The scanning system for single-sensor thermographs is usually located between the lens and the detector, and it is used to define the viewing direction of the thermograph.

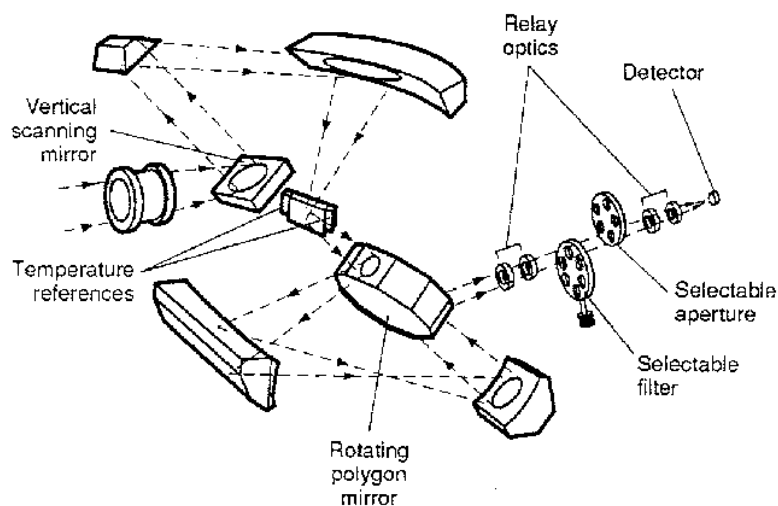


Figure 1.7: opto-mechanical scanning system with rotating mirrors

As shown in figure 1.7, this system makes use of a complicated assembly which involves a rotating prism, an oscillating mirror and several other fixed mirrors. When high frequencies of acquisition are needed, the rotational speed of the prism can reach high velocities; for example, the thermograph AGEMA 900 features a prism which can rotate at a speed of 16,000 *rpm*.

Although of older concept, these systems can be extremely accurate and are still sometimes preferred when the limitations of the FPA systems, described in the next paragraph, are considered unacceptable.

1.3.2 Focal Plane Array

The two-dimensional sensor Focal Plane Array (FPA) is used by most recent thermographic cameras. It is constituted by a square or rectangle substrate on which an elevated number of detectors are integrated. The most common detectors in use in FPA sensors (see §1.2 and figure 1.6) are:

- *Platinum Silicide* (PtSi): it operates in the first atmospheric window from 2 to 5 μm ; it is characterized by a great degree of simplicity hence low costs. It has a good thermal resolution (of the order of the tenth of degree) but it's unstable and needs calibration every time the thermograph is switched on; furthermore it requires a cryogenic cooling through a Stirling cycle
- *Indium Antimonide* (InSb): it operates in the 2-5.6 μm window, it is characterized by great sensitivity, it is very stable and doesn't need frequent calibration, and it has a very good thermal resolution (about 0.025 K) and a reasonable scanning frequency. It is cooled by a closed Stirling cycle. For its characteristics it is much more expensive than the PtSi sensor
- *Gallium Arsenide Quantum Well Infrared Photodetector* (GaAs QWIP): it operates at long wavelength, 8-9 μm . It is characterized by even greater performance than the InSb both in thermal resolution and in scanning frequency.
- *Non-cooled two-dimensional sensor* (microbolometric): mostly used for qualitative applications.

The presence of an elevated number of detectors represents a fundamental change with respect to the classical thermographic systems, because the image viewed by the thermograph focuses on the FPA and is subdivided among all of its detectors (see figure 1.8). This design allows FPA IR systems to avoid the need of mechanical scanning system, as the rotating polygons or galvanometric mirrors, which used in classic IR systems and described in the previous paragraph.

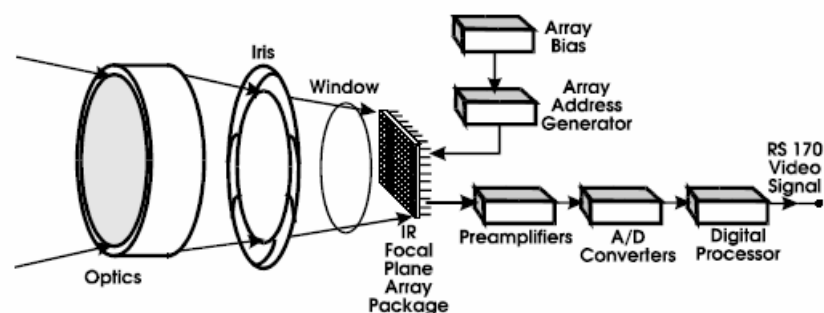


Figure 1.8: Schematic of a thermograph with an FPA sensor.

One consequence of this is that FPA sensors can have an integration time from 1/30 to 1/60 of second, which is much longer than the nanoseconds usually associated with classic IR systems; thanks to longer integration times, FPA based thermographs can have higher sensitivity and low electronic noise.

An FPA sensor is made by thousands of sensitive elements, and each one of them can have a slightly different reaction when hit by the same infrared radiation; this can result in non uniform images even when viewing surfaces at constant temperature. This problem is present in all FPA cameras, and is solved by appropriately regulating the gain of each pixel; this process of internal calibration is performed every time the camera is switched on, and it can also be forced via control software. Another problem related with FPA sensors is the unavoidable presence of dead or defective pixels. When a dead pixel is detected the thermograph automatically substitutes its measurement with interpolated values from nearby pixels. The percentage of dead pixels can range from less than 1% to about 2% for less expensive devices.

The FPA sensor is becoming the market standard thanks to its good spatial resolution and to the elimination of the costly and more fragile opto-mechanical scanning systems needed by classic IR systems.

1.4 Distinguishing characteristics of thermographs

The quantitative performance of a thermograph depends on some fundamental parameters which define its characteristics: thermal sensitivity, frequency of acquisition, spatial resolution and signal intensity resolution.

- The *sensitivity* of a thermograph is expressed by the NETD (Noise Equivalent Temperature Difference), which is the difference in temperature between two images generating a signal equal to the background noise: when the difference in temperature between two images is lower than the NETD the thermograph won't sense that difference. The NETD is evaluated at a known temperature of the sample, and can vary from 0.07 to 0.5 °C for measurements at ambient temperature.
- The *frequency of acquisition* represents the speed at which images are recorded by the thermograph. The whole field of view is investigated by horizontal or vertical scanning systems in a given number of lines or columns; a frequency of acquisition per line can therefore be defined and some thermograph, to attain a higher frequency of acquisition, can record a limited number of lines rather than its full field of view.
- The *spatial resolution* is the capacity of the system to distinguish elements of the surface of small dimension and to correctly measure their temperature. For a given frequency of acquisition the spatial resolution of the images is in general determined by the dimension of the sensor. In general the spatial resolution is defined by the Instantaneous Field Of View (IFOV) of the sensor or, better yet, by the number of IFOV which are comprised in the total field of view. In theory, the IFOV is the ratio between the dimension of the sensor and the focal length of the lens, but this is only an idealized geometrical definition; in practice the quantity of interest is the smallest size distinguishable by the thermograph.

The evaluation of the spatial resolution is fundamental for experimental applications, when it is not always possible to place the thermograph close to the measured surface. In such cases it is also important to check if the chosen thermograph has the possibility to mount telephoto lenses.

- The *intensity resolution* is usually described in terms of the number of gray level used to digitalize the thermal image, and it therefore also defines the minimum temperature difference which is digitalized with two different gray levels. For example, a 12 bit thermograph digitalizes the image in $2^{12} = 4,096$ gray levels; if the temperature interval measured by the thermograph is, say, -30 °C to 150 °C then its intensity resolution in terms

$180/4,096 = 0.044 \text{ } ^\circ\text{C}$. Usually thermographs include the possibility to change the measurable temperature interval with the use of proper filters.

1.5 Thermographs used in this work

Two thermographs have been used in this work: the FLIR SC3000 for the experiments performed in the Alta's high enthalpy HEAT wind tunnel (see chapter 4) and the AGEMA Thermovision 900 for the experiments performed CIRA's Scirocco Plasma Wind Tunnel (see chapter 5).

Both systems work in conjunction with personal computers, are operated by their proprietary control software, and generate sequences of IR images in output. Rather than describing their functioning in detail, a list of their fundamental characteristics, as outlined in this chapter, will be given.

The FLIR SC3000 is the thermograph used in the DIAS laboratory for a wide variety of applications. It has a long wave FPA sensor, making it apt for measurements in plasma flows, where long wave sensors are needed (Cardone, 2007). Its characteristics are listed in table 1.1

Detector type	GaAs QWIP, 320×240 pixels
Spectral range	8 to 9 μm
Field of view	20°×15°
IFOV	1.1 <i>mrad</i>
Frequency of acquisition	50/60 <i>Hz</i> non interlaced up to 750/900 <i>Hz</i>
Temperature range	-20 °C to +500 °C. 3 selectable ranges, up to 2000°C
Accuracy	±1 °C up to 150°C, ±2 °C above
Intensity resolution	14 bit

Table 1.1: Characteristics of the FLIR SC3000 thermograph

The Agema Thermovision SC300 is the thermograph used in CIRA for thermographic measurements in Plasma Wind Tunnel tests. It has a single long wave sensor; its characteristics are listed in table 1.2

Detector type	CDM
Spectral range	8 to 12 μm
Field of view	20°×10°
IFOV	230
Frequency of acquisition	15 Hz full frame, 2,551 Hz per line
NETD	0.07 °C up to 30 °C
Intensity resolution	13 bit
Image dimension	272×136

Table 1.2: Characteristics of the Agema Thermovision 900 thermograph

1.6 Thermograph calibration

When thermographic measurements are made, it is important to minimize all causes which can have negative effects on the precision of the measurements. The elaboration of the digital output of the thermograph should be done taking into account that:

- The relationship between temperature and the intensity of radiation reaching the sensor is not linear.
- The electromagnetic signal can be altered by the presence of bodies, such as wind tunnel windows, in the optical path.
- The external environment can source of direct or reflected emissions and can therefore influence the radiation absorbed by the sensor.

The most important variables influencing the quality of the measurement are: the emissivity of the body under exam - hereinafter considered opaque - the angle of view, the characteristics of the fluid interposed between the thermograph and the body and the possible presence of other transparent or reflective bodies in the optical path. The emissivity of the body must be as high as possible to improve the sensitivity of the system, and must be a known characteristic of the body under exam. The Kirchoff law states that the reflection coefficient ρ for an opaque body is given by

$$\rho = 1 - \varepsilon. \quad (1.8)$$

As a consequence, a low-emissivity body presents two simultaneous problems: it emits less than an ideal black body and reflects the energy irradiated by the environment more than higher-emissivity bodies. To minimize the effects of these reflections, it is important that ρ is kept as low as possible and that the environment is kept at a uniform and known temperature, so that existing reflections can be properly calculated

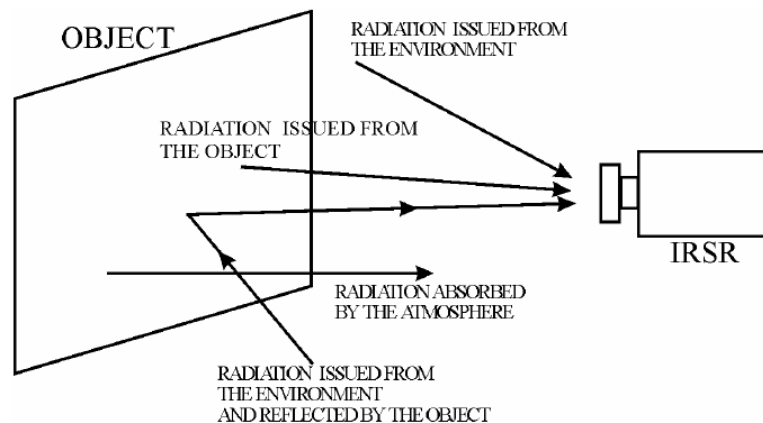


Figure 1.9: Schematic of the radiations which reach the thermograph

The fluid interposed between camera and body, usually atmosphere, influences the measurement through its absorption coefficient. If this coefficient is high, the fluid absorbs a significant percentage of the radiations emitted by the body and only the not-absorbed fraction of the radiation can reach the camera. Furthermore, the fluid itself is source of radiation.

For an opaque body (see figure 1.9), if S' is the radiation absorbed by the sensor and S_b , S_a and S_{atm} are the radiations emitted, respectively, by the body under measurement, by the environment (including interposed access windows) and by the atmosphere, a balance of emitted and absorbed *photons/s* can be done, to obtain:

$$S' = \tau \varepsilon S_b + \tau(1 - \varepsilon)S_a + (1 - \tau)S_{atm} \quad (1.9)$$

Where τ is the transmittance coefficient of the interposed fluid. This relationship between radiations can be transformed in a relationship between *Isotherm Units*, which are proportional to the number of absorbed photons through a constant C characteristic of each sensor, $I' = C \times S'$; this relation can be substituted in (1.9) to obtain:

$$I' = \tau \varepsilon I_b + \tau(1 - \varepsilon)I_a + (1 - \tau)I_{atm} \quad (1.10)$$

The values of I_b , I_a and I_{atm} are those corresponding, respectively, to the temperatures of the body, of the environment and of the atmosphere. I' is the value measured by the thermograph.

In equation (1.10) I' is measured by the thermograph, I_a and I_{atm} are known once the temperatures of the environment and of the interposed fluid are known. Similarly, the values of τ and of ε are known experimental values. I_b is therefore the only unknown quantity in (1.10) and it can therefore be calculated. Once I_b is known, the surface temperature of the body can be determined with the help of a calibration diagram.

Since the power that a body radiates in the infrared increases with temperature following a non-linear law, in order to correlate the isotherm units measured by the thermograph with the temperature of the body it is necessary to use a proper calibration diagram for the instrument. As already mentioned, the best relationship correlating the measurement of the thermograph to the temperature of the body is given by the Planck law:

$$I = \frac{R}{e^{B/T} - F} \quad (1.11)$$

where R , B and F are the three calibration constants which depend on the characteristic of the thermograph, of its lens, on interposed optical access windows etc. The calibration constants relative to the whole measurement field of the thermograph are given by the manufacturer; in

this case they can only take into account the characteristic of the thermograph, and not all other parameters just mentioned. As a consequence, when the thermograph is used for precise quantitative measurements it is preferred to measure these constants *in situ* through a calibration process done in test conditions. Equation (1.11) can be inverted to give T as a function of I :

$$T = \frac{B}{\ln\left(F + \frac{R}{I}\right)} \quad (1.12)$$

equation (1.12) is used to build the calibration diagrams.

The calibration diagrams are obtained using a blackbody. In this work, this has been made with a hollow copper body in which a hole of small dimensions has been drilled. The external surfaces have been insulated to make the body adiabatic. The internal surfaces of the body are characterized by high emissivity and are kept at known temperature by a copper circuit in which is circulated a fluid at controlled temperature coming from a high precision thermostatic bath. Because of the way the blackbody has been realized, it can be assumed that it always is at the same temperature of the thermostatic bath.

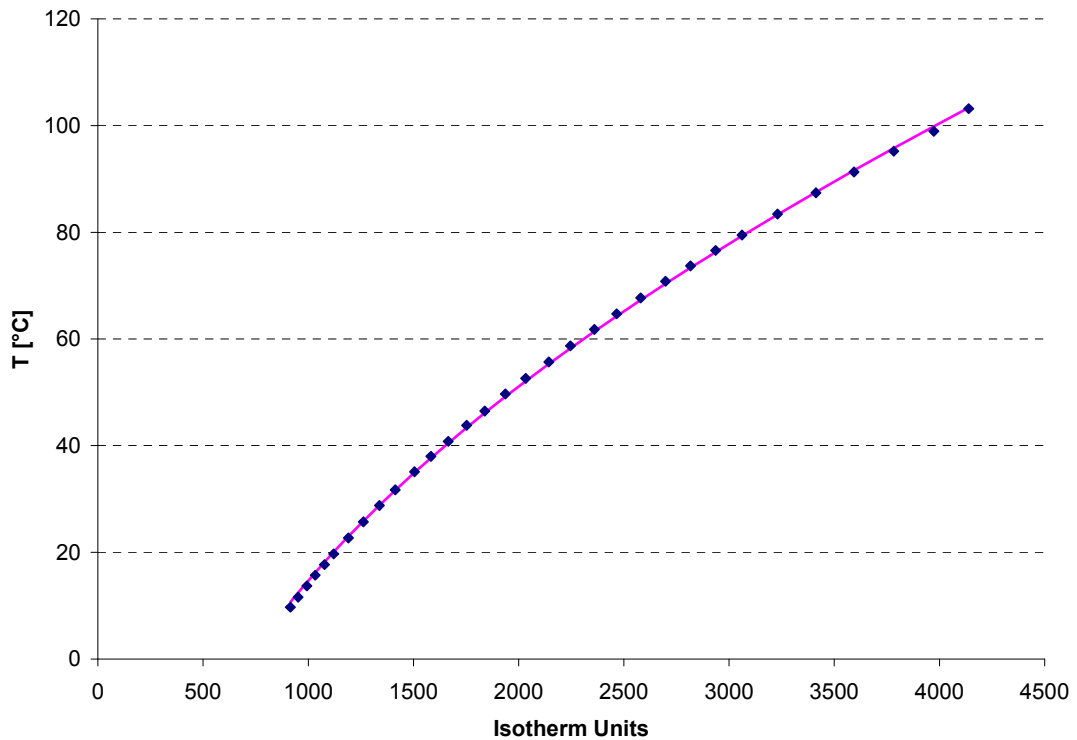


Figure 1.10: Calibration diagram for SC3000

The calibration procedure consists in:

- Having the thermograph look at the black body replicating the optical path that will be used in experiments
- Measuring simultaneously (1) the black body temperature T_{bb} with the help of a precision thermometer inserted in the thermostatic bath and (2) the Isotherm Units IU measured by the thermograph.

These measured data can be fitted by equation (1.12) through a regression process in which the constant R , B and F are calculated.

1.7 Emissivity calculation

Surface emissivity of materials depends strongly on their surface finish: a metal surface can vary within such extreme values as $\varepsilon = 0.05$ when polished to $\varepsilon = 0.95$ when oxidized. It is therefore understood that manufacturer's specification about emissivity, when given, are often just indicative and when accurate quantitative temperature measurements are needed, surface emissivity must be calculated directly on the test model.

Another reason for which emissivity calculations are needed is given by its directional nature for real bodies; as previously seen (figure 1.3), emissivity depends on the angle of view and, although it remains almost constant until the angle reaches about 50° , for greater angles of view it decreases rapidly. As a consequence, the calculation of directional emissivity is of primary importance when accurate measurements are needed on complex bodies.

The calculation of emissivity is accomplished by means of the simple calibration process explained below.

The experimental apparatus consists of a thermostatic bath, of a blackbody (as in the case of the thermograph calibration illustrated in the previous paragraph) and of a special support made of highly conductive material, like copper, whose purpose is to hold a sample of the material undergoing investigation. The support is kept at constant temperature by a copper circuit put in series with the black body and with the thermostatic bath. When the whole system is properly insulated, the black body and the metal support will be at the same temperature.

A thin sample is placed on the metal support, and is covered with insulating material to minimize emission. After a proper relaxation time, the surface of the sample will reach the same temperature as the metal support. At this point the insulation is removed from the front of the sample, and an IR image is taken of the black body and of the sample simultaneously.

The thermograph should be located close to the sample in order to minimize absorption from the interposed fluid, and the thermostatic bath should be kept at high temperature to minimize the effects of the environment.

The Infrared Units measured by the thermograph on the sample, I_s , and on the black body, I_{bb} , along with a measurement of ambient temperature, are all that is needed to calculate emissivity. Equation (1.10) can in fact be applied to both measurements, to obtain

$$\begin{cases} I' = \tau I_{bb} + (1 - \tau) I_{atm} \\ I'' = \tau \varepsilon I_s + \tau (1 - \varepsilon) I_a + (1 - \tau) I_{atm} \end{cases} \quad (1.13)$$

From the discussion above, it results that $I' = I''$, hence:

$$\varepsilon = \frac{I_{bb}}{I_s - I_a} - \frac{I_a}{I_s - I_a}. \quad (1.14)$$

The metal support can be rotated on its axis, and the process described above can be repeated several times to calculate emissivity at different angles of view. In case dependence of emissivity on temperature is suspected, the whole process should be repeated at different temperatures.

It is found that directional emissivity is well fitted by the following:

$$\varepsilon = \varepsilon_0 \cos(\theta)^{\frac{a}{\cos(\theta)^b}} \quad (1.15)$$

Where the coefficient ε_0 , a and b are found through a regression process.

Figure 1.11 shows the calculation of directional emissivity performed on MACOR[®] for this work.

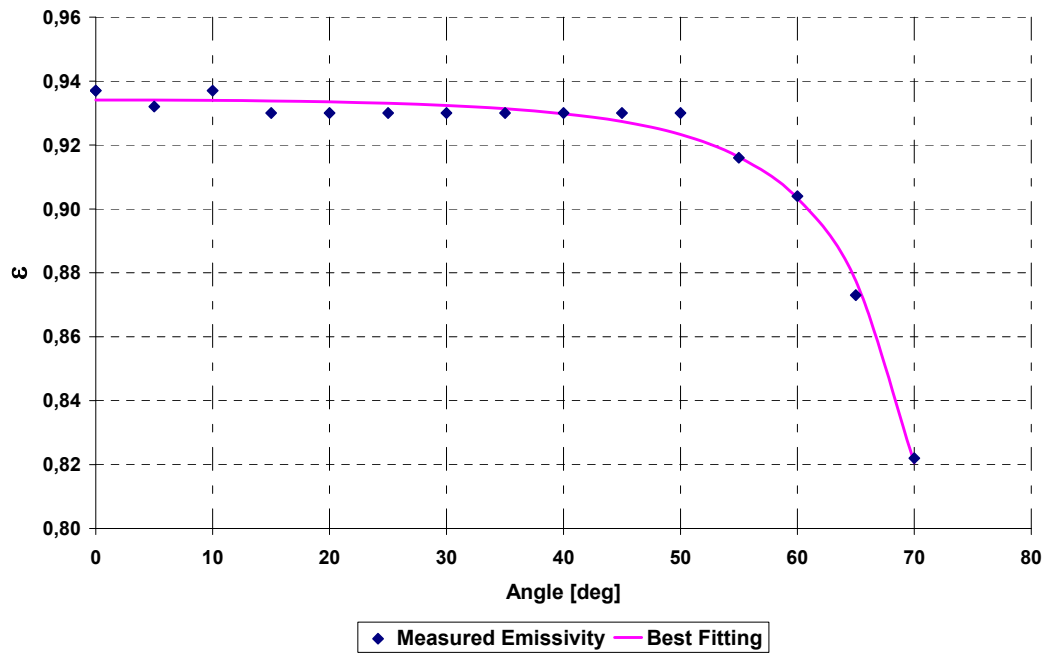


Figure 1.11: Directional emissivity of MACOR[®]

CHAPTER 2: THE PINHOLE MODEL

Flow visualization and measurement techniques requiring the use of video supports produce their outputs in the form of images. Although these images are rich in information, as in the case of the infrared thermography extensively used in this work, they are still two-dimensional representation of a three-dimensional reality. The need to gather more detailed information, as is the case of 3D flow visualisation or of measurements on models of complex shape, has led to the development of resection techniques to establish a correspondence between the plane of the image and the real world.

Although the use of these techniques is already quite common in fluid-dynamic measurements and in flow visualization (see for example Willert, 2006 and Giordano & Astarita, 2008), to the knowledge of the author geometric reconstruction has never been used for infrared thermography.

The lack of information in the correspondence between image and model is in fact particularly critical in thermographic measurements. First of all, because of the dependence of emissivity on angle of view (see figure 1.11), precise temperature measurements cannot be made without geometrical reconstruction. Secondly, the possibility to locate on the model phenomena that can be visualized by means of IR thermography (such as flow separation or reattachment, see chapter 4) can allow to make precise quantitative measurements.

One of the purposes of this work has therefore been to develop a resection method for thermographic measurements based on established resection techniques. The choice fell on the algorithm proposed by Tsai (1987), because of its accuracy. In the case of bodies with complex geometries, infact, processing the image with simple methods (as polynomial fittings) might be not sufficient or even impossible. In this case photogrammetry techniques are therefore used to establish a relationship between the coordinates in the reference system and the object in the image plane. A further advantage of the Tsai algorithm is that it directly outputs the parameters needed to locate the position of the camera with respect to the model, making the calculation of directional emissivity relatively simple.

In the present chapter the characteristic of the pinhole model will be illustrated.

2.1 The Tsai algorithm

The calibration algorithm proposed by Tsai (1987) refers to the pinhole (or perspective) model, which reduces the process of image formation to the configuration of a point through which all light rays leaving the object have to pass before reaching the camera sensor. This model can be extended, with additional parameters, to represent the distortions induced by the lens.

The Tsai algorithm involves the use of a versatile two-stage technique to calculate a series of calibration parameters depending on the position and orientation of the camera, on its focal length, on the radial distortion of the lens and on image scanning parameters (pixel distance, frequency of acquisition).

2.1.1 The pinhole model

The model used to describe the camera acquisition system uses a series of approximations. The first regards the optics, for which the model of thin lens is used. This model is characterized by the following properties (see figure 2.1):

- All the rays parallel to the optical axis when passing through the lens are refracted in such a way to pass through a point of the optical axis called focus.
- All the rays passing through the centre of the lens continue their path with no deviation.

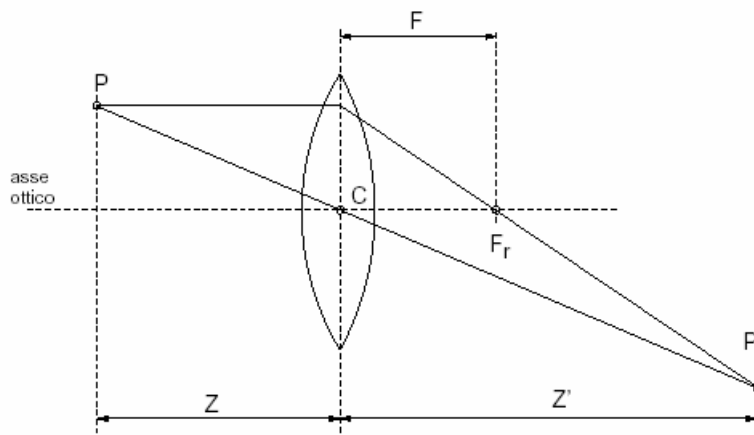


Figure 2.1: Construction of the image of a point

From the triangle similitude criteria, the Fresnel's equation gives the relationship between the distances of the object and of its image, respectively z and z' from the centre of the lens:

$$\frac{1}{z} + \frac{1}{z'} = \frac{1}{f} \quad (2.1)$$

where f is the focal length of the lens. When $|z| \gg f$, equation (2.1) becomes

$$|z'| = f \quad (2.2)$$

The pinhole model consists of an image plane \mathfrak{R} and of a point C , centre of the image, located at a distance f from \mathfrak{R} . The line passing through C and orthogonal to \mathfrak{R} is called *optical axis*; its intersection with \mathfrak{R} is called *main point*.

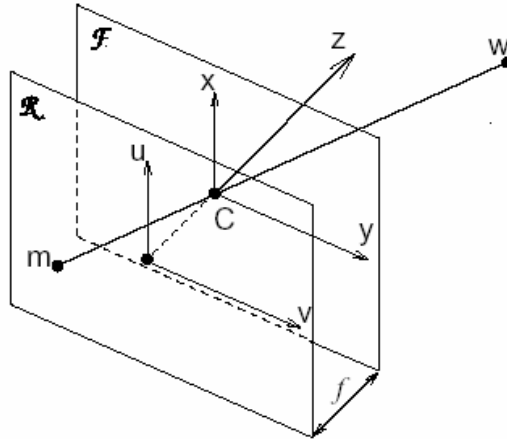


Figure 2.2: Representation of the pinhole camera model

The model used for the camera can't be limited only to the perspective projection of the real life scene on the image plane, but it must take into account also two other processes, fundamental in the formation of the image:

- The transformation between the space reference system and the image reference system. This is accomplished by a rigid rotation and a rigid translation.
- The process of discretization due to the CCD sensor (seen as two-dimensional pixel matrix), and its position in relation to the optical centre. This process involves some problems, like the determination of the physical centre (which might not coincide with the optical centre of the camera), and the introduction of different scale factors for the two axes (the coordinates are measured in pixel and need to be rescaled; the shape of the pixel can be not square and different scale factors must be used); finally it is necessary to take into account the fact that, owing to misalignments between different lines of the sensor, the axes of reference might not be orthogonal but inclined of an angle ϑ .

2.1.2 The advantages of a versatile calibration technique

The calibration of a camera in the context of 3D visualization consists in determining the camera internal optical and geometrical characteristics (intrinsic parameters) and its

position and orientation in a given space coordinate system (extrinsic parameters), for the following complementary purposes:

- Infer 3D information in real space starting from the coordinates in the image plane. This is the case in which the exact location of object seen on an image need to be located with precision in the real space. Applications can vary in the most diverse fields, from the measurement of the dimensions of mechanical parts to the analysis of trajectories.

This is also the case of the present work, in which the Tsai calibration is performed with the purpose to localize on the 3D surface test article the points analyzed in the 2D IR image.

- Infer information in image coordinates once the space coordinates are known. This case is primarily used to validate the one illustrated above.

Also this application is used in the present work since the orientation of the normal to the surface of the test model in the 3D space is used, along with information on camera position and orientation provided by Tsai calibration parameters, to calculate the angle of view between the camera and each point of the surface of the model, hence to know the directional emissivity and to perform accurate temperature measurements which would otherwise be impossible.

The technique proposed by Tsai is quite versatile because it can be used even with commercial cameras and lenses and does not require *ad hoc* cameras. The obvious advantage is that it can be used with a wide variety of different instrumentations, there included the thermographic cameras used in the present work. To implement such a versatile use, the model also models the distortion induced by the lens, a parameter which classical polynomial interpolations do not include, and it consequently is very accurate

2.1.3 Introduction to the calibration algorithm

The calibration of a camera, in the traditional approach, implies the estimation of a large number of parameters via non-linear fitting techniques. The simplest way to reduce the computational load of such algorithms is to use the so called Direct Linear Transformations, which solve a linear system based primarily on the correspondence between points on the image plane and points in the space; this approach therefore ignores the dependencies between different parameters and, to reach acceptable accuracy, the determination of a large number of parameters is needed, leading to overdetermined system and somewhat limiting the advantages obtained by the linearization the system; furthermore the lens distortion effects are not taken into account.

The Tsai algorithm consists in reducing the dimension of the parameter space through a *radial alignment* constraint, function only of rotation and translation between camera and calibration point. This is a non-linear equation which can anyway be efficiently solved; the other parameters are determined with projection equations. In such a way an efficient calibration technique which, starting from reasonable estimates for known parameters such as the position of the camera with respect to the calibration points, provides appropriate values for the unknown intrinsic parameters.

2.1.4 The transformation from the “object” reference system to the “image” reference system

The camera model referenced in this paragraph is shown in figure 2.1.

- (x_w, y_w, z_w) are the 3D coordinates in space.
- (x, y, z) are the reference coordinates for the camera, with origin in the optical centre O , and z axis coincident with the optical axis.
- (X, Y) is the coordinate system in the image plane, centered on the point O_i (intersection of the optical axis with the image plane), and having axes parallel to those of the camera reference system.
- f is the focal length, distance between the optical centre and its projection on the image plane.
- (X_u, Y_u) are the coordinates of the point (x, y, z) in the case of ideal pinhole model.
- (X_d, Y_d) are the real coordinates on the image plane, and differ from (X_u, Y_u) in that they take into account the distortion of the lens.

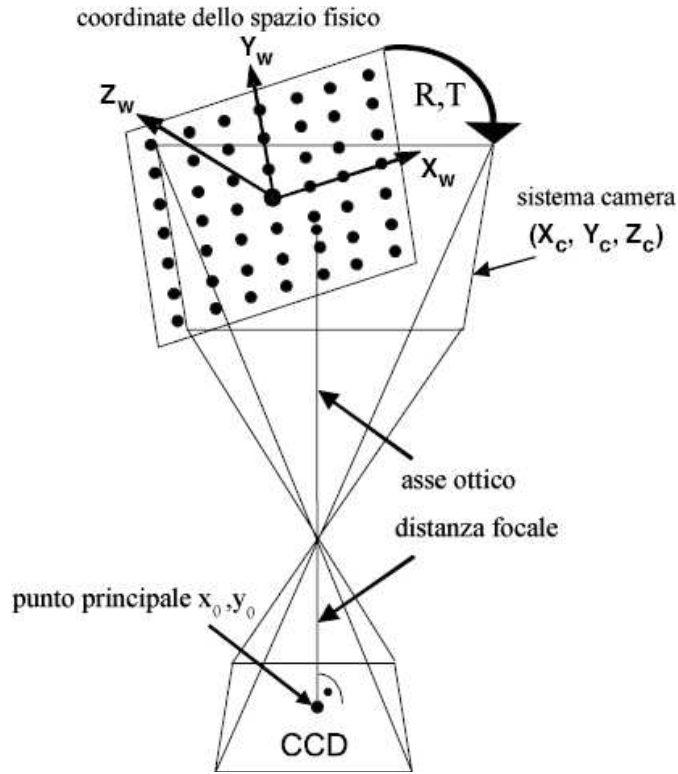


Figure 2.3: Schematic of the pinhole model

It is finally needed to take into account that the coordinates in the image plane are integer number, being expressed in pixel, and it is therefore necessary to introduce additional parameters linking the coordinates in the image plane to those in the discrete image plane. The four steps needed to go from the (x_w, y_w, z_w) space coordinates to the (X_f, Y_f) digital image coordinates are illustrated in detail below:

Step 1: Transformation from the “object” reference system to the camera reference system.

This is a simple rigid body transformation, and it is obtained through rotation of the reference system and translation of its origin.

$$\begin{bmatrix} x \\ y \\ z \end{bmatrix} = \underline{\underline{R}} \cdot \begin{bmatrix} x_w \\ y_w \\ z_w \end{bmatrix} + \underline{T} \quad (2.1)$$

$\underline{\underline{R}}$ is the rotation matrix, which is an orthogonal 3×3 square matrix; \underline{T} is the translation vector, made of three component. It is known that the 9 terms of the rotation matrix can be expressed in terms of three independent rotations (Euler angles), to univocally determine the transformation between the two reference systems. Given that

$$\underline{T} = \begin{bmatrix} T_x \\ T_y \\ T_z \end{bmatrix} \quad (2.2)$$

In this step the parameters to calibrate are **6** (extrinsic parameters): the 3 independent rotation characterizing the matrix \underline{R} and three translations T_i .

Step 2: Transformation between the camera reference system into ideal image reference system (it is reminded that the ideal system is the one described by the pinhole model only). From geometrical considerations it is obtained:

$$\begin{bmatrix} X_u \\ Y_u \end{bmatrix} = \frac{f}{z} \cdot \begin{bmatrix} x \\ y \end{bmatrix} \quad (2.3)$$

In this step the parameter to calibrate is f .

Step 3: To perform the transformation from ideal image coordinates into real image coordinates a mathematical model is needed for radial distortion. To this purpose, the radial distortion parameters D_x and D_y are introduced:

$$X_d + D_x = X_u \quad (2.4)$$

$$Y_d + D_y = Y_u \quad (2.5)$$

D_x and D_y are not constant but depend on the coordinates (X_d, Y_d) ; their functional form is unknown and they are therefore expressed in terms of a power series:

$$D_x = X_d(k_1 r^2 + k_2 r^4 + \dots) \quad (2.6)$$

$$D_y = Y_d(k_1 r^2 + k_2 r^4 + \dots) \quad (2.7)$$

$$r = \sqrt{X_d^2 + Y_d^2} \quad (2.8)$$

The parameters to calibrate in this step are the distortion coefficients k_i . It's been verified that limiting the calculation to the first two terms k_1 and k_2 permits to reach sufficient accuracy without imposing the heavier computational load needed to estimate further terms of the power series. Tangential distortion is also present, but it is negligible when compared to radial distortion.

Step 4: It is finally needed to transform the coordinate in the image plane to coordinates in pixel of the digital image on the CCD:

$$X_f = s_x d_x'^{-1} X_d + C_x \quad (2.9)$$

$$Y_f = d_y^{-1} Y_d + C_y \quad (2.10)$$

(X_f, Y_f) are the line and column number of the generic pixel on the digitized image, and (C_x, C_y) are the column number and line number of the central point of the digitized image. Furthermore:

$$d'_x = d_x \frac{N_{cx}}{N_{fx}} \quad (2.11)$$

d_x and d_y are the distances between adjacent sensors in the image plane along, respectively, the directions x and y . N_{cx} is the number of sensors in the x direction and N_{fx} is the number of pixel in a line in the sampling of an image.

In order to perform the coordinate transformation from the image plane into the discrete image plane information about the distances between adjacent pixels is needed. When these information are not known a calibration on more planes is needed. In any case, the scale factor in y is implicitly known from the focal length f , since it scales the image in the same way along x and along y . It is therefore possible to set $d_y = 1$, while the focal length will be the product between the real focal length and the scale factor along y .

The four steps just described are schematically represented in figure 2.4.

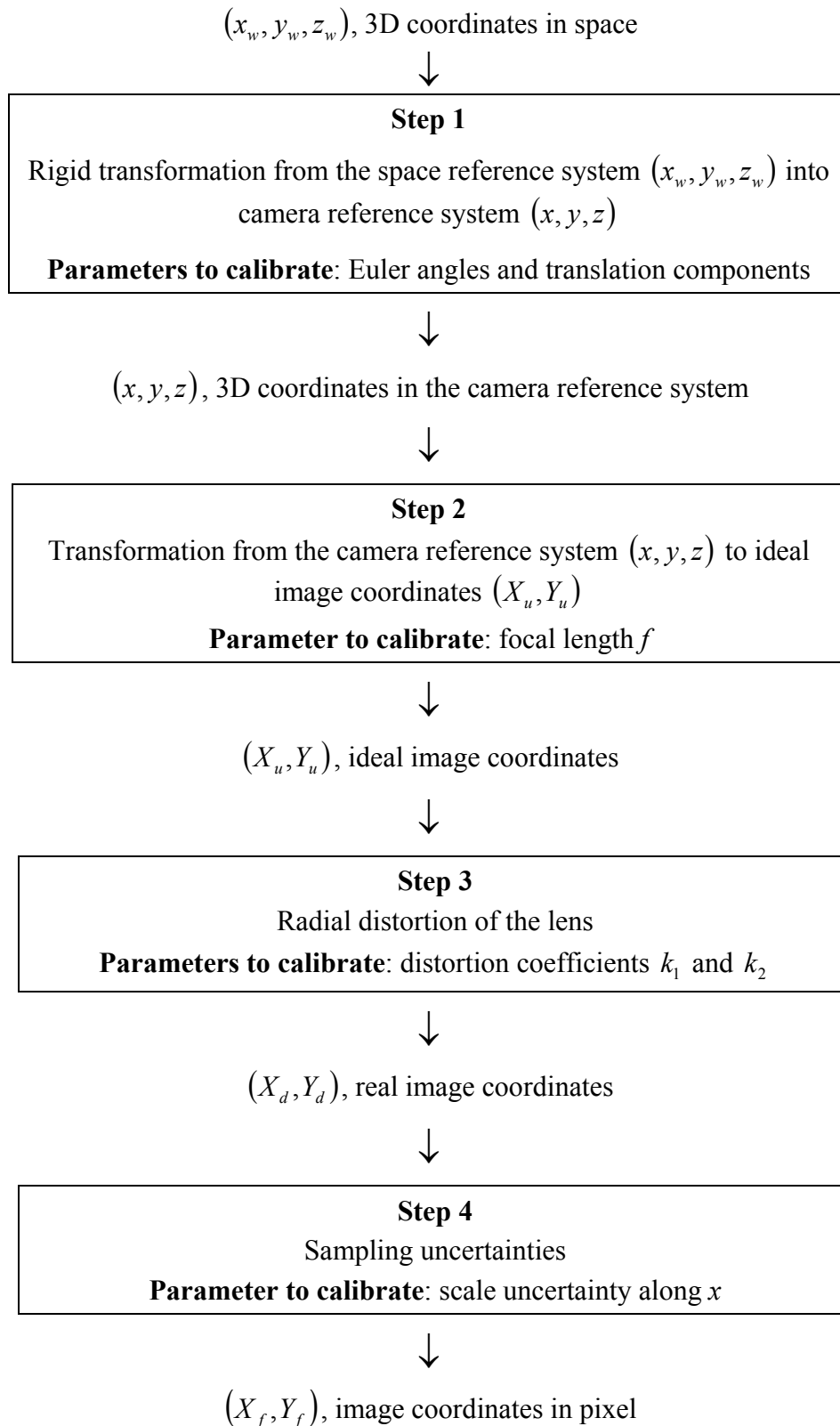


Figure 2.4: Calibration algorithm

2.1.5 The set of calibration constants

Combining the steps 2, 3 and 4 in §2.2.4 it is possible to obtain the relationships linking the coordinates in pixel on the CCD to the coordinates in the camera reference system.

Substituting (2.3) and (2.4) in (2.9), and (2.3) and (2.5) in (2.10) it follows:

$$s_x^{-1}d'_x X + s_x^{-1}d'_x X k_1 r^2 = f \frac{x}{z} \quad (2.12)$$

$$d'_y Y + d_y Y k_1 r^2 = f \frac{y}{z} \quad (2.13)$$

where

$$r = \sqrt{(s_x^{-1}d'_x X)^2 + (d_y Y)^2} \quad (2.14)$$

Substituting (2.1) in (2.12) and (2.13) it is finally possible to get the relationship which links the coordinates in pixel on the CCD with the coordinates in the 3D space:

$$s_x^{-1}d'_x X + s_x^{-1}d'_x X k_1 r^2 = f \frac{r_1 x_w + r_2 y_w + r_3 z_w + T_x}{r_7 x_w + r_8 y_w + r_9 z_w + T_z} \quad (2.15)$$

$$d'_y Y + d_y Y k_1 r^2 = f \frac{r_4 x_w + r_5 y_w + r_6 z_w + T_y}{r_7 x_w + r_8 y_w + r_9 z_w + T_z} \quad (2.16)$$

where r_i are the components of the \underline{R} matrix.

In these expression there are in total **12** optimizable parameters, which can be divided into two categories:

- **extrinsic parameters**, which are linked to the relative position of the camera and of the object and of the relative orientation of the respective reference systems. These are the 3 rotations and the 3 translations illustrated in §2.2.4
- **intrinsic parameters**, which allow the transformation between the 3D camera reference system into the 2D discrete image system. This category includes:

f	focal length
k_1, k_2	distortion coefficients
s_x	scale uncertainty along x
(C_x, C_y)	line and column number of the central pixel of the image on the CCD

2.2 The calibration process

The use of the Tsai algorithm to establish a correspondence between space coordinates and (x_w, y_w, z_w) discrete image coordinates (X_f, Y_f) implies the need of a calibration process to estimate the 12 parameters needed perform this transformation. This purpose is generally accomplished with the help of a calibration *target*. This is a plane surface on which an array of equidistant points in two orthogonal directions is placed; once an origin has been set on this surface and the distance between the points is known, the physical coordinates of each point of the array is known; once an image has been recorded by the camera undergoing calibration, the coordinates of the points will be known also in the image reference system. Starting from these known coordinates, the 12 parameters of Tsai are found from equations (2.15) and (2.16) through a process of best fitting.

The calibration points in reality are in fact not points but circular markers. The symmetry implied by this choice of the marker shape is needed in order to avoid the mathematical complication which other shapes would cause.

The Tsai model includes several kinds of calibration, but the only viable one when s_x is not known (see equation 2.12) is the multi-plane calibration, which consists on taking several images of the same target, provided that a translation along the z axis is performed each time; it is therefore to needed to take a set of images not all coplanar.

The target used for the calibration of the ALTA TC-1a experiments (chapter 4) is shown in figure 2.5

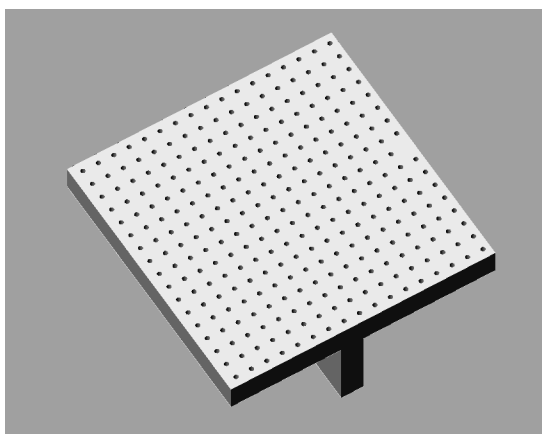


Figure 2.5: a typical calibration target

It must be noticed that the practical design of a target, both in terms of dimensions and in terms of the characteristics of the markers and of the construction materials depends first of

all on the particular application (optical cameras will need different targets than fluid-dynamic cameras), and secondly on the particular experiment.

For the applications in thermography described in this work, the contrast between the markers and the plane on which they are placed can be reached either using materials of different emissivity or devising some method to keep the markers at a different temperature from the plane.

Given the dependence of the target design on the particular experiment, detailed descriptions of the design procedures is postponed to chapters 4 and 5.

CHAPTER 3: HEAT FLUX SENSOR

The measurement of surface heating is one of the critical goals of hypersonic wind tunnel testing. It also is usually more complex than other fluid dynamic measurement because it is not performed directly but extracted indirectly from temperature measurements. A heat flux sensor is therefore composed by a temperature sensor coupled with a physical and mathematical model of the heat transfer mechanism on which the heat flux sensor is based.

In this chapter a brief description of the problems connected with heat flux measurements will be done, followed by a description of the thin film sensor, which is the most widely used heat flux identification technique in wind tunnel measurements, and of its shortcomings. The second part of the chapter will deal with the description of a new heat flux sensor, which allows to improve the results attainable by the thin film sensor, and with its numerical validation.

3.1 Heat flux measurements

Heat flux measurements are typical inverse problems: given the effects (the time evolution of surface temperatures) it is needed to find the causes (the heat fluxes who generated the temperature rise). Inverse problems are typically ill-posed problems in the sense that they are sensible to measurement errors and can become unstable (Beck, 1985); heat flux sensors must therefore be able to deal with this sort of problems. In the past a further complication and source of instability was due to the fact that temperature sensors were located inside the model and not on its surface. The use of thin film surface resistance thermometers first and of infrared thermography have later permitted to overcome this problem.

This work deals only with IR thermography and the heat flux sensor proposed herein is supposed to be used with IR measurements (although other surface temperature sensors are not ruled out). The heat flux sensor almost universally used in high enthalpy wind tunnels implementing IR measurements is the thin film sensor, and for this reason it will be described in the next paragraph

3.2 Thin film sensor

With the thin film sensor, surface temperature measurements are performed either by means of IR thermography, or with the help of a very thin resistance thermometer (the "film") which measures the surface temperature of the thermally thicker slab to which it is bonded. Heat flux is inferred from the theory of heat conduction in a semi-infinite wall which assumes that the medium into which heat is conducted has infinite thickness. Data reduction is based on the general differential equation for heat conduction in an isotropic solid which, assuming constant thermal characteristics, is given by

$$K(\nabla^2 T) = \rho c_p \frac{\partial T}{\partial t} \quad (3.1)$$

which for one dimensional heat flux becomes

$$K \frac{\partial^2 T}{\partial x^2} = \rho c_p \frac{\partial T}{\partial t} \quad (3.2)$$

In the case of semi-infinite wall the initial and boundary conditions for equation (3.2) are

$$\begin{cases} T(x,0) = T_{wi} \\ K \left. \frac{\partial T(x,t)}{\partial x} \right|_{x=0} = q_w(t) \\ T(\infty,t) = T_{wi} \end{cases} \quad (3.3)$$

where the heat flux $q_w(t)$ is unknown.

To simulate an infinite wall in real tests, it is necessary carefully evaluate the test conditions and choose test times t_p and materials in such a way that temperature perturbations do not reach the far wall of the slab for the whole duration of the test. This happens when $Fo < 1/2$, where $Fo = \alpha_p / L^2$ is the Fourier number, α the thermal diffusivity $K/(\rho c_p)$ and L the thickness of the slab.

Equation (3.2)-(3.3) can be solved analytically taking Laplace transforms (Carslaw & Jaeger, 1959), to give $T(0,t)$ in function of the boundary condition $q_w(t)$ or, alternatively

$$q_w(t) = \sqrt{\frac{\rho c_p K}{\pi}} \cdot \frac{1}{2} \left[\frac{T_w(t)}{\sqrt{t}} + \frac{1}{2} \int_0^t \frac{T_w(t) - T_w(\tau)}{(t-\tau)^{3/2}} d\tau \right] \quad (3.4)$$

It can be noted that in equation (3.4) it is the combination of thermal properties of the heat conducting medium which is important, and this is known as thermal inertia²

$$I = \sqrt{\rho c_p K} . \quad (3.5)$$

This dependence is valid also in the general case and it will be recalled later; in table 3.1 values of I for some materials are shown.

The solution of equation (3.4) involves the numerical integration of the second term in square brackets; following the approach of Cook & Felderman (1966), whose algorithm is generally accepted for aerospace applications, the numerical evaluation of (3.4) is expressed by:

$$q_w(t_j) = \sqrt{\frac{\rho c_p K}{\pi}} \sum_{i=1}^j \frac{T_w(t_i) - T_w(t_{i-1})}{\sqrt{t_j - t_i} + \sqrt{t_j - t_{i-1}}} \quad (3.6)$$

where the subscripts refer to the time steps in which the temperature has been measured.

The use of (3.6) presents the problem of noise amplifications due to the fact that the model relies on the differentiation of noisy temperature measurements on the surface of the body (see equation (3.3)), which in turn leads to the need of using smoothing techniques of the surface temperature signal. An attempt to counter this problem is given by Hedlund et al. (1980), who proposed a method in which the equation (3.2)-(3.3) is solved for the cumulative heat input into the model surface $Q(t)$:

$$Q(t) = \sqrt{\frac{\rho c_p K}{\pi}} \int_0^t \frac{T_w(\tau)}{\sqrt{t - \tau}} d\tau ; \quad (3.7)$$

equation (3.6) can be numerically integrated as follows:

$$Q(t_j) = \sqrt{\frac{\rho c_p K}{\pi}} \sum_{i=1}^j \frac{T_w(t_{i-1}) + T_w(t_i)}{\sqrt{t_j - t_{i-1}} + \sqrt{t_j - t_i}} \Delta t . \quad (3.8)$$

Surface heat flux can finally be calculated by differencing $Q(t)$:

$$q(t_j) = \frac{Q(t_j) - Q(t_{j-1})}{t_j - t_{j-1}} . \quad (3.9)$$

Although this method is somewhat superior to the other as far as noise amplification is concerned, the use of techniques for noise reduction is still needed.

² I is sometimes referred to as “thermal product”.

Material	$I \left[kJm^{-2}K^{-1}s^{-1/2} \right]$
Quartz (SiO ₂)	1.53
Pirex	1.53
Macor (theoretical)	1.76
Chromel	8.51
Constantan	9.06
17-4PH stainless steel	8.35
plexiglas	0.58

Table 3.1: Typical values for I (from Simeonides, 1992)

3.2.1 Numerical solution

The analytical solution (3.4) of equation (3.3) relies on several limiting assumptions. In particular, the body must be semi-infinite and the thermal properties of the material must not vary with temperature. To overcome these problems, alternative approaches implying a numerical solution of equation (3.2) have been proposed by various authors (Consigny & Le Sant 1990, Boyd 1994, Hollis 1995); all these models imply a basic numerical solution of equation (3.2). The most sophisticated of this methods (Consigny & Le Sant, 1990) uses the following initial and boundary conditions:

$$\begin{cases} T(x,0) = T_{wi} \\ q_w(t) = K \frac{\partial T(x,t)}{\partial x} \Big|_{x=0} \\ T(L,t) = T_L(t) \text{ or } q(L,t) = q_L(t) \end{cases} \quad (3.10)$$

where L is the thickness of the slab, $T_L(t)$ and $q_L(t)$ are, respectively, known temperature and known heat flux on the far wall of the model. Thermal properties are considered to be known and to be either constant or varying linearly with temperature. The system (3.2)-(3.10) is solved with a finite volume technique implementing a Crank-Nicholson time discretization.

The method of Consigny & Le Sant is the heat flux reduction technique currently used at ONERA.

3.3 Limits of the thin film sensor

The thin film sensor described in the previous paragraph presents two main problems: it is highly sensitive to noise in temperature measurements and it presents problems in those time steps in which temperature measurements are not available, typically at the beginning of the test.

The problem of noise amplification is critical both in the analytical and in the numerical implementations of the thin film sensors, because they are based on the same mathematical model. Smoothing techniques include global curve fitting of the entire temperature trace with a simple analytical function (Miller, 1981) and local linear least squares spline fitting. Furthermore, filtering can be applied both on the temperature signal and on the calculated heat flux, but this can cause distortion in the measured data. In all cases, heat flux identification by means of the thin film is characterized by a significant uncertainty of the results, as it will be seen in the results of CAST TC-1a test campaign (see §4.12, where the results obtained by the sensor proposed in this work will be compared with those from obtained by means of the analytical thin film).

The second main problem connected with the thin film sensor regards the impossibility to reconstruct the temperature rise when temperature measurements are not available; this circumstance can happen for different reasons in different wind tunnels:

- In some facilities, the model is inserted in the test chamber after the wind tunnel has started, and for this reason temperature measurements are not available until the model reaches its final test position, given that the thermograph is fixed and doesn't follow the movements of the model; the temperature distribution $T_w(x, t_{imm})$ at the instant t_{imm} in which the model reaches the test position is unknown. A further problem is given by the circumstance that during insertion the model passes through the boundary layer of the tunnel and is therefore exposed to a flow whose conditions are different from those characterizing the test.
- In other facilities, notably short duration wind tunnels, the model is already in test position when the tunnel is started. In such cases the model can be exposed to a flow which is not completely developed during the first instants of the test; furthermore, filtering techniques used to calculate flow conditions in the wind tunnel, make flow parameters unavailable at the beginning of the test.

A proper reconstruction of the temperature rise is impossible because the mathematical model at the basis of the thin film deals only with the temperature variation

inside the model and on its surface, and doesn't attempt any physical modelling of the flux applied to the surface of the test article.

3.4 New heat flux sensor

The heat flux sensor proposed in this work tries to overcome the limits of the thin film sensor described in §3.3. This sensor relies on the solution of the one dimensional heat conduction equation (3.2) in which the unknown surface heat flux $q_w(t)$ is measured through a whole domain parameter estimation technique. The use of such a technique implies that the unknown heat flux is considered to be dependent on parameters which need to be estimated through an iterative optimization process in which the whole measured temperature transient is considered at each iteration (conversely, with the thin film sensor the calculation of the heat flux at instant t is based on temperature information for times $\tau < t$).

The parameters on which $q_w(t)$ depend are based on the physical characteristics of the flow. The unknown surface heat flux is in fact considered to be the sum of two contributions: the radiative heat flux, depending on the fourth power of the surface temperature T_w , and a term which depends linearly on T_w and includes both chemical and convective contributions, according to the equation

$$q_w(t) = h(T_w(t) - T_{aw}) + \sigma \varepsilon (T_w(t)^4 - T_r^4). \quad (3.11)$$

The use of equation (3.11) allows meaningful reconstruction of the temperature rise when measurements are not available (typically, as explained in the previous paragraph, at the beginning of the test); the whole domain estimation, although involving heavier computational load, allows low sensitivity to measurements errors, as the rest of the paragraph will show.

The mathematical model at the basis of the sensor will first be described, a description of the iterative optimization method will come next, and the numerical validation of the code will finally be illustrated.

3.4.1 Mathematical Model

The equation to be solved inside the body is described by the equation (3.2) which is shown here again

$$K \frac{\partial^2 T}{\partial x^2} = \rho c_p \frac{\partial T}{\partial t}, \quad (3.12)$$

with boundary conditions

$$\left\{ \begin{array}{l} T(x,0) = T_{wi} \\ K \frac{\partial T(x,t)}{\partial x} \Big|_{x=0} = q_w(t) = h(T_w - T_{aw}) + \sigma \varepsilon (T_w^4 - T_r^4) \\ K \frac{\partial T(x,t)}{\partial x} \Big|_{x=L} = q_L(t) \text{ or } T(L,t) = T_L(t) \end{array} \right. \quad (3.13)$$

The initial temperature distribution $T_{wi}(x)$ is known; in particular, since temperature measurements inside the body are usually not available, T_{wi} is considered to be constant unless the starting point for heat flux estimation is the result of numerical calculations due to known heat flux previously applied.

For the boundary condition at the far wall, any known temperature $T_L(t)$ or flux $q_L(t)$ can be used; unfortunately, temperature evolutions are usually not known, or measured, on the far wall. In this case, two different approaches can be used:

- 1) The body can be made semi-infinite, so that $T(L,t) = T_{wi}$;
- 2) In a more realistic approach, the far wall can be considered adiabatic. This is true in most high enthalpy wind tunnels, in which the test chamber pressure is very low (of the order of the millibar), there is no flow on the far wall and the far wall itself is at significantly lower temperature than the surface exposed to the flux; in this situation, both convective and radiative heat fluxes are negligible and the far wall effectively behaves as an adiabatic wall.

The unknown heat flux $q_w(t)$ depends on several parameters:

- 1) The heat flux coefficient h is unknown and needs to be estimated.
- 2) The wall temperature T_w is known from the numerical solution of the equation (3.12)-(3.13).
- 3) The adiabatic wall temperature T_{aw} is not known and can either be estimated or set to a known value³.
- 4) ε is the surface emissivity of the model, and is known either from literature or from experimental calibration (see §1.1 and §1.7).
- 5) T_r is a reference temperature towards which the model radiates. It could be subject of optimization but in this work it has been considered to be the same as the ambient temperature.

³ As an example, it is reminded that for laminar hypersonic flows over a flat plate $r \cong T_{aw}/T_0 = \sqrt{Pr}$.

It is important to highlight that this model evaluates explicitly the radiative heat flux whose contribution can be important in tests in high enthalpy wind tunnels, where the surface temperatures can reach high values,

The optimization process consists in varying the optimizable parameters on which $q_w(t)$ depends, to minimize the functional of the sum of the squared differences between the measured temperatures, $T_{wTH}(t)$, and the temperatures $T_{wNUM}(t)$ generated numerically by the solution of (3.12)-(3.13):

$$\int_0^{t_p} (T_{wTH}(t) - T_{wNUM}(t))^2 dt \quad (3.14)$$

From the description above it is clear that estimation of the heat flux q_w relies on estimation of one or two parameters, h or (h, T_{aw}) respectively; as it will be shown later, the choice is imposed by test conditions. As it will be seen in the next paragraph the use of a further, non physical, optimizable parameter (*delay*) is also needed for the technique to work properly; the two cases described above will be in any case referred to as one-parameter and two-parameter optimization. In the rest of the chapter all discussions will be made with explicit reference to the two-parameter optimization but they are equally valid for one-parameter optimization when the obvious modification that T_{aw} is not optimizable is taken into account.

3.4.2 Iterative Method

The evolution of surface temperature on the tested body is measured with the help of IR thermography and of the resection technique described in chapters 1 and 2; for each point of the surface the experimental temperature rise $T_{wTH}(t_i)$ is therefore known. $T_{wTH}(t_i)$ is made up of a number N of temperature measurements which depends on the frequency of acquisition of the thermograph, f_s , and on the duration of test t_p . To estimate the surface heat flux the following steps are followed:

- 1) Set T_r and T_{wi} to known values;
- 2) Input $T_{wTH}(t_i)$ to the optimization program;
- 3) Set trial values to the unknown undergoing optimization $(h, T_{aw}, delay)^4$;

⁴ The meaning of the *delay* parameter will be explained shortly.

- 4) Solve the heat conduction problem (3.12)-(3.13) inside the body to generate the temperature rise $T_{w_{NUM}}(t)$. A finite volume method has been implemented for the numerical solution of (3.12)-(3.13), see appendix 1 for details on the implementation;
- 5) Modify h , T_{aw} and $delay$ in the attempt to minimize the error functional (3.14) which in its discrete form becomes

$$\sum_{j=nSkip}^N [T_{w_{TH}}(t_j) - T_{w_{NUM}}(t_j + delay)]^2 \quad (3.15)$$

in which $T_{w_{TH}}(t_0) = T_{w_{NUM}}(t_0) = T_{wi}$;

- 6) Go back to point (4) and iterate to convergence.

Equation (3.15) introduces two parameters, $nSkip$ and $delay$, which deserve explanation:

- $nSkip$ is used to account for the insertion time of the model in the wind tunnel. When, for one or more of the reasons outlined in §3.3, temperature measurements for the first time steps are not available, these points are not considered for the optimization; in other words, for $t < t_{nSkip}$ $T_{w_{TH}}$ is not known. The numerical temperature rise generated in these first time steps is still meaningful because its generation is based on a mathematical model which takes into account the physical reality of the flow. The time t_{nSkip} , known from the experimental conditions, is called the “insertion time” t_{imm} :

$$t_{imm} = t_{j=nSkip} \quad (3.15bis)$$

- The $delay$ parameter introduces an “unphysical” translation of the numerical temperature curve. It has been used to take into account two important facts: (1) the initial instant in which the model is exposed to flux is not known with precision and (2) the mathematical model does not completely replicate reality because, as described in §3.3, the model could be inserted in the test chamber after the wind tunnel has been started and the flow might not be in test conditions during the start of the wind tunnel.

The use of $delay$ allows to consider the flow around a body located in the test chamber starting from an unphysical instant (to be estimated) and exposed only to the flux considered by the mathematical model.

3.4.3 Optimization Methods

Classically, the method used to solve non-linear optimization problems is the *Levenberg-Marquardt* method (Levenberg, 1944, Marquardt, 1963), which is highly stable

and reliable. Unfortunately, to use this method the so called “sensitivity coefficients” need to be known; this coefficient are derivatives of the numerical solution relative to the unknowns $\partial(T_{w_{NUM}})^n / \partial P_j$, with $n = [nSkip, nSkip + 1, \dots, N]$ and $P_j = [h, T_{aw}, delay]$. The optimization described in this work it relies on the iterative solution of a nonlinear differential equation; the *Levenberg-Marquardt* method would require the inefficient calculation of the sensitivity coefficient at each time step and at each iteration and is therefore better avoided.

It’s been preferred to use optimization methods which do not require the calculation of derivatives; in particular, the optimizations methods used in the code are those proposed by Powell (as described in Press et al., 2007) and its variation proposed by Brent (1973), whose optimization routine is called *Praxis*. This last method is characterized by the use of a random jump of preset magnitude for optimizable parameters when solution is not found through normal iterations⁵.

⁵ For a full description of the various optimization methods refer to the quoted bibliography.

3.5 Dimensional Analysis

The heat flux sensor is to be used in a wide variety of situations: models can have widely differing thermal characteristics and test durations can range from a few hundred milliseconds to several seconds. In order to assess the validity of the heat flux sensor taking into account all possible test configurations, it is worthwhile to analyze it in adimensional terms.

The dimensional analysis which follows is based on the Buckingham π -theorem, described in Appendix 2. The purpose of a dimensional analysis to express the problem under exams in terms of a limited number of adimensional groups; the number of adimensional groups is smaller than the number of dimensional parameters on which the problem depends, implying a general picture of the problem along with a better understanding of the situation.

The mathematical model on which the sensor is based is held by equations (3.12)-(3.13) which are shown again here:

$$K \frac{\partial^2 T}{\partial x^2} = \rho c_p \frac{\partial T}{\partial t}, \quad \text{BC:} \begin{cases} T(x,0) = T_{wi} \\ K \frac{\partial T(x,t)}{\partial x} \Big|_{x=0} = h(T_w - T_{aw}) + \sigma \varepsilon (T_w^4 - T_r^4) \\ K \frac{\partial T(x,t)}{\partial x} \Big|_{x=L} = 0 \end{cases} \quad (3.12),(3.13)$$

It is possible to recognize eleven parameters on which the problem depends:

$$\{t, T, x, (\rho, c_p, K), \sigma \varepsilon, (h, T_{aw}), T_{wi}, T_r\}$$

where σ is a dimensional constant.

The only temperature T of interest for the model is the surface temperature T_w ; if a study is performed only for an infinite wall (as is the case for the numerical validation illustrated in the next paragraph) the problem ceases to depend on the parameter x . Furthermore, as noted in §3.2, the influence of the material on the heat flux can be univocally characterized by the material's thermal inertia I ; keeping in mind these considerations, the total number of parameters on which the problem depends is reduced to the following eight:

$$\{t, T, I, \sigma \varepsilon, (h, T_{aw}), T_{wi}, T_r\}, \quad (3.16)$$

where the two parameters object of optimization are in parentheses.

With the help of Buckingham π -theorem, the following adimensional groups are identified:

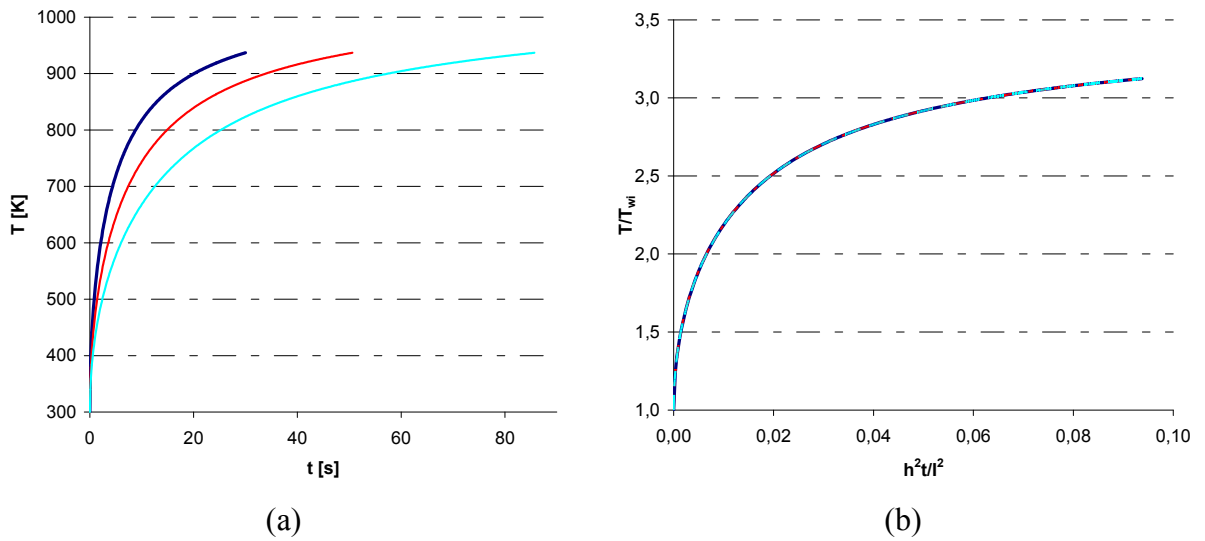
$$\pi_1 = \frac{h^2 t}{I^2}, \quad \pi_2 = \frac{T}{T_{wi}} \quad (3.17.a)$$

$$\pi_3 = \frac{T_{wi}}{T_{aw}}, \quad \pi_4 = \frac{T_r}{T_{wi}}, \quad \pi_5 = \frac{\sigma \varepsilon T_{aw}^3}{h} \quad (3.17.b)$$

The use of these adimensional groups implies that the temperature diagrams which in dimensional terms are represented on the plane (t, T) , in adimensional terms will be instead represented on the plane (t^*, T^*) , where $T^* \equiv \pi_2$ and $t^* \equiv \pi_1$.

A quick analysis of the adimensional group π_1 shows how temperature diagrams characterized by different values of I or t , although distinct on the dimensional plane, will collapse to a single diagram in the adimensional plane (see figure 3.1); the same thing will not happen when h varies unless π_5 is kept constant. Given the range in which h can change, it is noted that it is unrealistic to keep π_5 constant. Error diagrams will therefore be drawn keeping T_{aw} constant instead; results for different values of h will therefore not collapse onto a single curve on the adimensional plane, and results for different values of T_{aw} will be shown in different diagrams

Finally it must be noticed that, when adimensional parameters are used to characterize a wind tunnel test (as in the case of the numerical validation described in §3.6), the test time t_p is chosen as characteristic time to use in π_1 .



⁶ The five adimensional groups shown here are obviously not the only possible choice, but are the ones which have been most appropriate for the current analysis. In particular, π_2 , π_3 and π_4 are all temperature ratios; different ratios could be used to generate equally meaningful adimensional groups.

Figure 3.1: Temperature diagrams for $\pi_1 = 9.37 \times 10^{-2}$ and $\pi_5 = 137$. Blue line: $t_p = 30$, $I = 200$; red line: I and t_p are varied; cyan line: h , ε and t_p are varied. (a) the diagrams on the dimensional plane, (b) on the adimensional plane the three diagrams collapse onto a single one

3.5.1 Acceptable limits for adimensional parameters

In the table below the typical range of existence for the parameters shown in (3.16) and for the adimensional groups π_1 and π_5 .

	min	max
σ	5.76E-08	5.76E-08
ε	0.50	1.00
t_p [s]	1.0	60.0
ρ [kgm^{-3}]	275	2,000
c_p [$Jkg^{-1}K^{-1}$]	1,000	1,100
K [$Wm^{-1}K^{-1}$]	0.1	100
h [$Wm^{-2}K^{-1}$]	5	100
T_{aw} [K]	1,500	6,000
T_{wi} [K]	300	300
T_r [K]	300	300
I [$kg^2K^{-2}s^{-5}$]	1.66E+02	1.48E+03
h^2t_p/I^2	1×10^{-7}	2×10^1
$(\sigma\varepsilon/h) \cdot T_{aw}^3$	1×10^{-5}	2×10^3

Table 3.2: Variability for parameters of interest

It is noted that, although single parameters may happen to attain values outside the range shown it is extremely rare that they will all contribute in the same direction to the adimensional parameters; it is therefore possible to claim that in real tests values for π_1 and π_5 outside the limit shown in table 3.2 cannot be expected.

In figure 3.2 various temperature rises are shown for π_1 varying within the limits shown in table 3.2

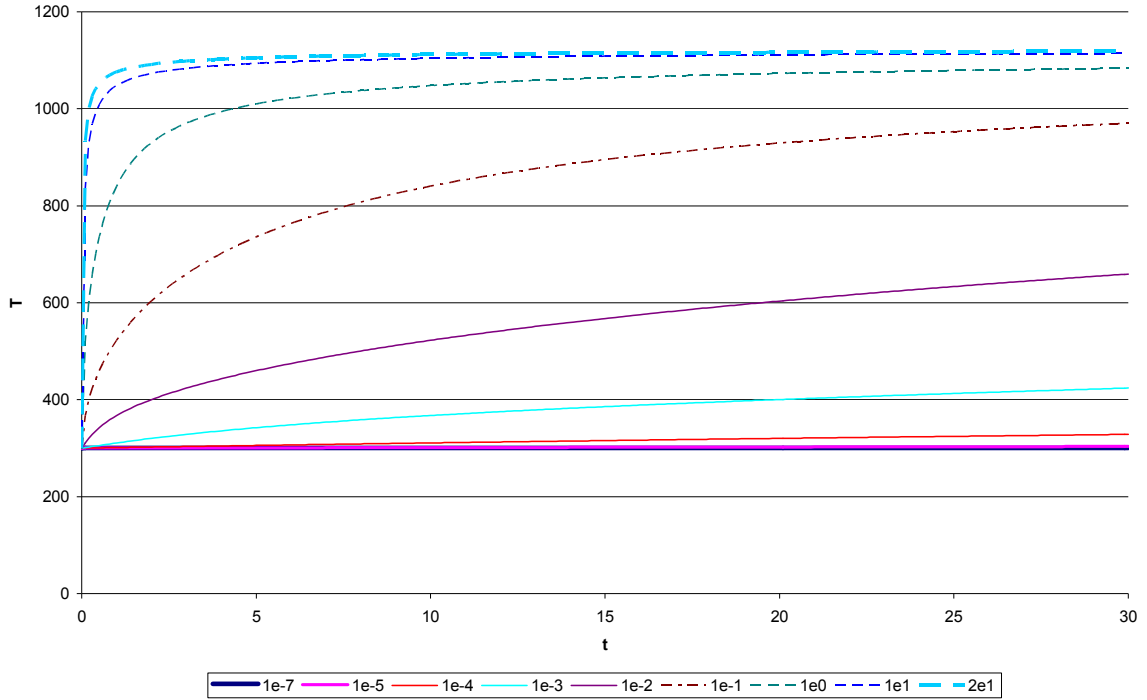


Figure 3.2: Temperature rises for $T_{aw} = 1,500$ for $h = const.$, $t_p = 30s$ and different values of π_1

It can be noticed that for high values of π_1 the temperature rises reach just a few Kelvin even for the full duration of a 30 second test; at the other extreme, there are temperature rises of several hundred degrees in the time span of a few hundred milliseconds. It is considered that such extreme cases are unrealistic. As a consequence, in the course of the numerical validation described in the next paragraph, a narrower range of variation for π_1 will be considered:

$$\pi_1 = \frac{h^2 t_p}{I^2} \in (1 \times 10^{-3}, 1 \times 10^0) \quad (3.18)$$

3.6 Numerical Validation

A full numerical validation has been carried out for the optimization problem presented in §3.4 and §3.5. The purpose of the numerical validation is to analyze the error made by the heat flux sensor in the estimation of h and T_{aw} , as meaningful parameters characterizing each temperature rise (or, equivalently, each experimental scenario) in order to characterize it and to identify its limits of applicability. The parameters to be varied are the following:

- 1) The adimensional parameters (3.17), following the criteria described later in this paragraph.
- 2) The intensity of the noise in temperature measurements (see §3.6.2).
- 3) The insertion time t_{imm} , namely the initial time lapse (if present) in which temperature measurements are not available.

As far as the adimensional parameters are concerned, the range of variation for π_1 and π_2 is derived from the analysis made in §3.5.1; for the other adimensional groups, the following considerations are applicable:

- 1) The temperatures T_{wi} and T_r are considered test parameters and not under the control of the experimenter. For the numerical optimization these temperatures will be considered to be constant and equal to the ambient temperature T_{amb} . As a consequence π_4 is constant, and the variation of π_3 are ignored.
- 2) The error diagrams will show the statistical parameters of interest on the plane (π_3, π_1) for different values of T_{aw} . As mentioned, T_{aw} varies as T_{wi} is kept constant and π_3 will vary consequently. It doesn't make sense to keep π_3 constant because the variation of T_{aw} , which in this work belongs to the interval (1,500;6,000), would imply proportional variations in T_{wi} which are absolutely not realistic. As a consequence, tests characterized by different values of T_{aw} will necessarily be shown on different diagrams.
- 3) For the sake of generality, in the course of numerical validation the body is considered to be semi-infinite (assumption which has also influenced the dimensional analysis, as pointed up in §3.5) and its thermal and radiative characteristics constant.

3.6.1 Method

The validation method can be outlined in the steps described below and with the help of figures 3.2 and 3.3, where a sample optimization is shown.

- 1) For each value of π_1 , of π_5 and of T_{aw} under exam, an “experimental” temperature rise is generated numerically solving equation (3.12)-(3.13); the subscript "th" will be used to describe this solution. The temperature rise $T_{th}(t)$ is generated with a very small time step dt_f , to make the numerical error negligible, and is subsequently sampled at a time step dt_s representative of the frequency of acquisition of the thermograph; when $t_{imm} > 0$ all the points for $t < t_{imm}$ will not be included in the optimization; in figures 3.3 and 3.4 $T_{th}(t)$ is the solid blue line and the discarded points for $t_{imm} = 5s$ are represented by the dashed blue line.
- 2) A random noise with zero mean and known standard deviation is added to the temperature rise $T_{th}(t)$ generated in step (1), to obtain the noisy temperature rise $(T_{th}(t))_D$. This is the temperature rise which is given in input to the optimization routine; $(T_{th}(t))_D$ is the pink line in figure 3.3 and 3.4.
- 3) Initial attempt values are given for h and T_{aw} , and a first attempt temperature rise is generated (red line in figure 3.3).
- 4) The heat flux is estimated. The result of the optimization is shown by the red line in figure 3.4.

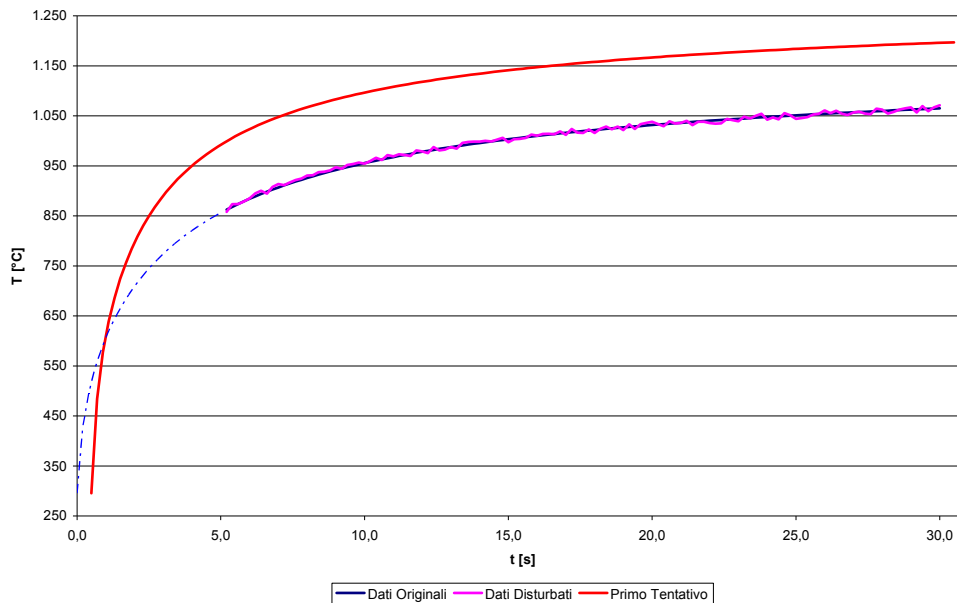


Figure 3.3: “Experimental” temperature rise, noisy temperature rise and first attempt temperature rise for $t_{imm} = 5s$

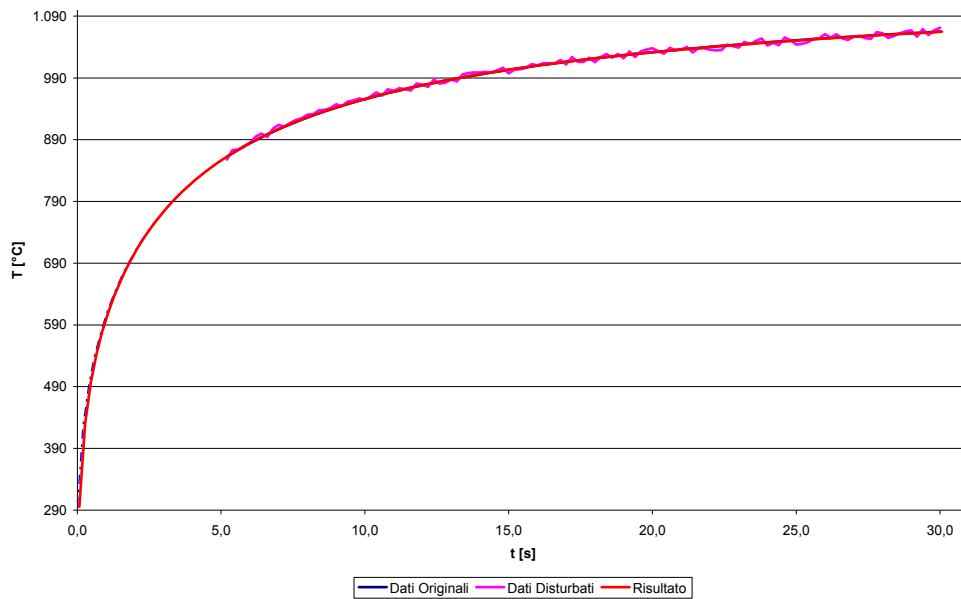


Figure 3.4: Result of the optimization.

Steps (2) to (4) described above are repeated \tilde{n} times; The selection of the number of tests is based on statistical considerations and is based on the examination of the data convergence with the number of optimizations. Figure 3.5 shows the evolution of h and of its average with the number of tests for one of the validations described in this paragraph. It is seen that the choice of $\tilde{n} = 1,000$ is sufficient to insure data convergence.

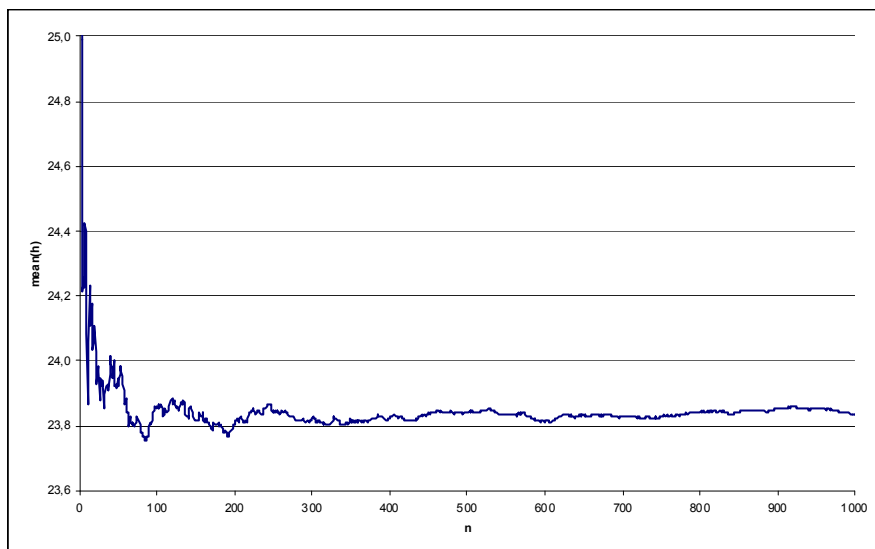


Figure 3.5: Statistical convergence of h parameter

3.6.2 Type and intensity of noise

The noise added to the numerically generated temperature diagrams must reflect the accuracy of the thermograph, both under the point of view of the intensity of the noise and under the point of view of its statistical distribution.

Intensity and pdf of the noise of the SC3000 thermograph has therefore been measured. Several images of a black slab at ambient temperature have been taken (figure 3.6). The average temperature has been calculated for each picture and subtracted pixel by pixel to obtain an image showing the zero-mean random noise of the SC3000. Figure 3.7 shows the pdf of the noise measured in such a way.

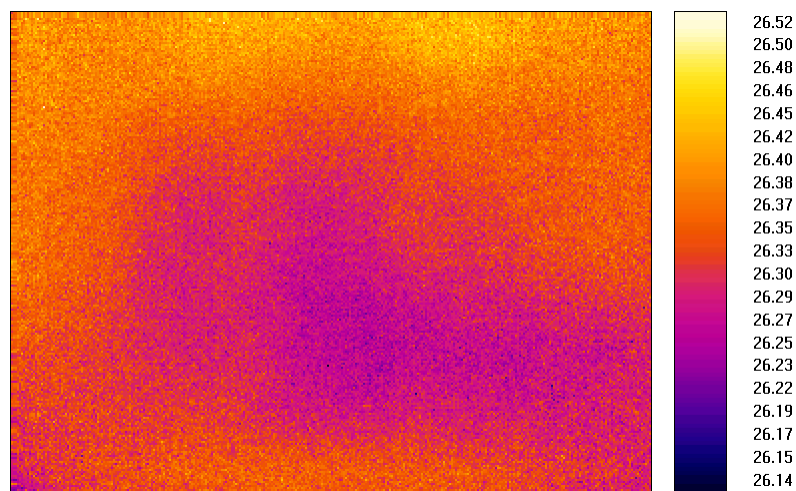


Figure 3.6: Thermogram of a black slab at constant temperature as seen by the SC3000 thermograph

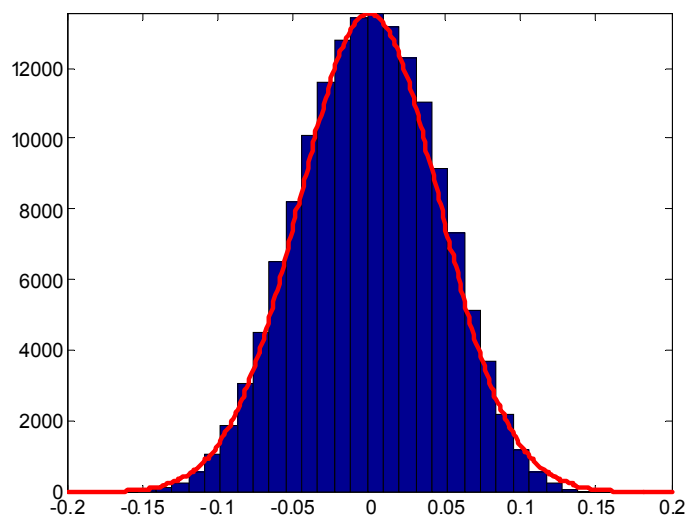


Figure 3.7: pdf of random noise for the thermograph SC3000 at ambient temperature, and comparison with a Gaussian curve with the same standard deviation. The pdf is calculated from the thermogram shown in figure 3.6

The standard deviation of the random noise has resulted in a value of $\sigma_{noise} = 0.048^{\circ}C$, and its distribution is Gaussian, as shown by the red curve in figure 3.7, which is a Gaussian with a standard deviation $\sigma_g = \sigma_{noise}$.

The present analysis leads therefore to the use of a noise with Gaussian distribution for the numerical validation of the code. As far as the intensity of the noise is concerned, it is important to point up that the random noise calculated in this paragraph represents a best case scenario for noises expected in real tests: sources of noise other than the accuracy of the thermograph are to be expected; these noises can have the most varied origins are impossible to assess not only in a general analysis like the this one, but also in presence of an accurate description of the test facility. To keep these further sources of noise into account, the numerical validation has been performed with noise intensities much higher than the one calculated here.

3.6.3 Error parameters

It is necessary to define a number of parameters capable to describe unequivocally the goodness of the optimization.

If p is the exact value of the parameter to estimate, p_i the value of that parameter as estimated in the generic optimization i and $\bar{p} = \frac{1}{\tilde{n}} \sum_{i=1}^{\tilde{n}} p_i$ the average value of the total number of estimations, we can define the following error parameters:

$$\text{Bias:} \quad \beta = \bar{p} - p \quad (3.19)$$

$$\text{Total Error:} \quad \delta = \sqrt{\frac{1}{\tilde{n}} \sum_{i=1}^{\tilde{n}} (p_i - p)^2} \quad (3.20)$$

$$\text{Standard Deviation:} \quad \sigma = \sqrt{\frac{1}{\tilde{n}} \sum_{i=1}^{\tilde{n}} (p_i - \bar{p})^2} \quad (3.21)$$

The value β shows the difference between the exact value and its ideal estimation, σ is a measure of the oscillations around the average in the estimation under investigation and δ is the average error which is done in the optimization.

When $\beta = 0$, σ will be equal to δ . In presence of bias, δ can be different from σ and the two values are not correlated.

3.6.4 Sampling rate

In point (1) at the beginning of §3.6.1 it has been mentioned that, for the purpose of numerical validation, the “experimental” temperature rise is sampled at the rate dt_s characterizing the frequency of acquisition of the thermograph f_s .

The results of the optimizations obviously depend on f_s ; strictly speaking, it must be noticed that the optimizations should be performed keeping the number of samples N_s constant:

$$N_s = \frac{t_p}{f_s} = \text{const.} \quad (3.22)$$

In the present numerical validation a high acquisition frequency has been chosen, to make validation results independent of N_s . In particular, f_s has been chosen after an analysis of its influence on the validation results and keeping in mind technological limits of current thermographs as $f_s = 1 \times 10^{-4} s$.

3.7 Results: two-parameter optimization

The numerical validation has been performed following the method described in detail in the previous paragraphs. The results shown below regard those optimizations in which the two physical parameters h and T_{aw} , and the non-physical parameter $delay$ are estimated.

In absence of noise, the optimization program is capable to estimate the parameters with no error in all the configurations taken into consideration.

As mentioned before, although modern thermographs feature very low noise levels (normal noise with standard deviation $\sigma_{noise} = 0.048K$ for the SC300 at ambient temperature, see §3.6.2), higher levels of noise are expected in wind tunnel experiments. As a consequence, the numerical validation has been performed for two levels of noise, one characterized by $\sigma_{noise} = 0.8K$ and the other by $\sigma_{noise} = 1.6K$.

It is finally noted that, among the error parameters described in §3.6.3, the total error has always resulted very similar to the absolute value of the bias. For the sake of brevity, it will therefore not be shown in the error diagrams below. Likewise, since a good result in the estimation of h implies a consequent good result in the optimization of T_{aw} , only the results regarding h will be presented.

Figures 3.8 and 3.9 show the results of the validation in terms of bias and standard deviation for $t_{imm} = 0$ and $\sigma_{noise} = 0.8K$; figures 3.10 and 3.11 show the case of $\sigma_{noise} = 1.6K$. The influence of the insertion time is shown in figure 3.12.

The error diagrams show rather clearly the features of the heat flux sensor>

- 1) The optimization works better for higher values of T_{aw} .
- 2) For a given value of T_{aw} , better optimizations are achieved when π_5 is smaller, namely when the ratio T_{aw}/h decreases.
- 3) For small values of π_1 the optimization worsens and can fail.
- 4) As π_1 is increased, the optimization improves until an optimal value of π_1 is reached; after that, if π_1 is further increased the optimization doesn't improve.
- 5) Increasing the noise has the effect to translate upwards the error diagrams. This means that, if π_1 is high enough, the optimization process works even in presence of strong noise, although its quality deteriorates. This result also implies that the optimal value for π_1 is independent of the level of noise.

Point (4) represents a significant result of the numerical validation, in that it can give useful hints in the design of an experiment. In fact, remembering that $\pi_1 = \frac{h^2 t_p}{I^2}$, it is seen that for each value of (π_1, π_5) the error diagrams suggest can suggest both an optimal test time and an appropriate choice of materials for the model.

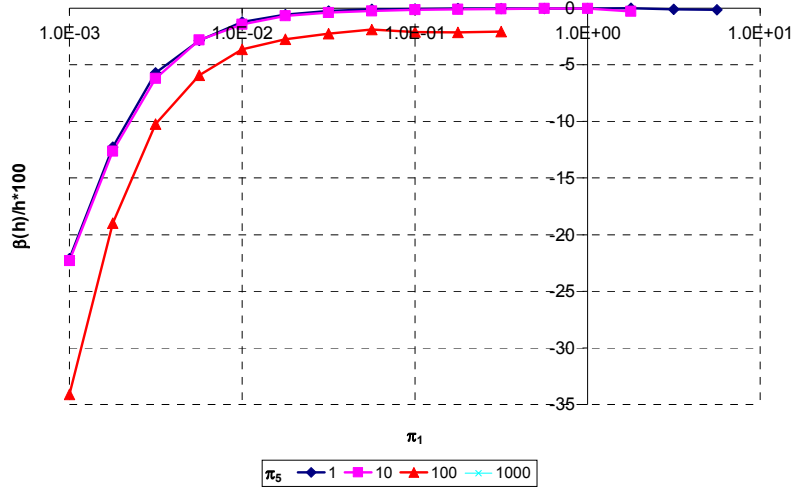
Although the numerical validation shows excellent results, with uncertainties in the estimation of h well under 0.5% when T_{av} is high, even in presence of high noise, it must be noted that the results shown in figures 3.8-3.11 are ideal upper limits. First of all it must be noticed that thermographs with extremely high frequencies of acquisition f_s are usually not available, and lower f_s will imply worse results. Secondly, as already mentioned, all the diagrams are drawn for $t_{imm} = 0$.

The influence of the insertion time is shown in figure 3.12 in terms of the ratio

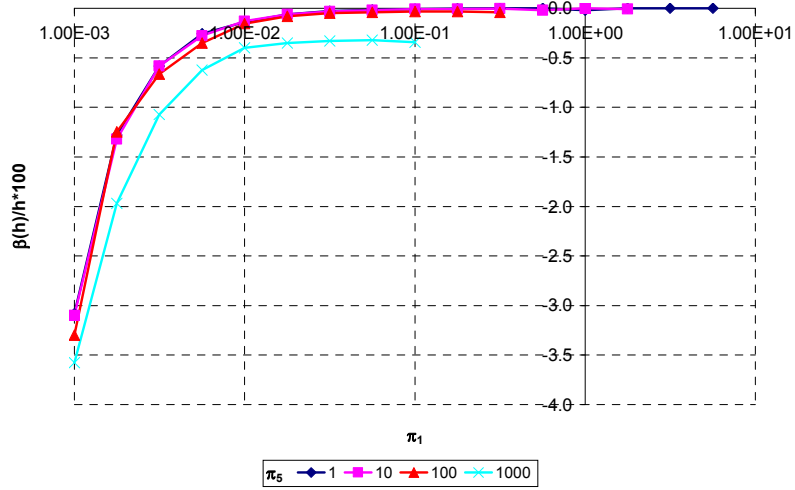
$$\frac{\sigma_h(t_{imm}/t_p)}{\sigma_h(t_{imm} = 0)} \quad (3.23)$$

where σ_h is the standard deviation of the error in the estimation of h . In practice, to know the expected error in the estimation of the heat flux in presence of a finite insertion time, the results shown in diagrams 3.8-3.11 should be multiplied by the values shown in figure 3.12 for a given t_{imm} . It is seen that normal insertion times lasting 5%-10% of the duration of the test have limited influence on the results of the optimization.

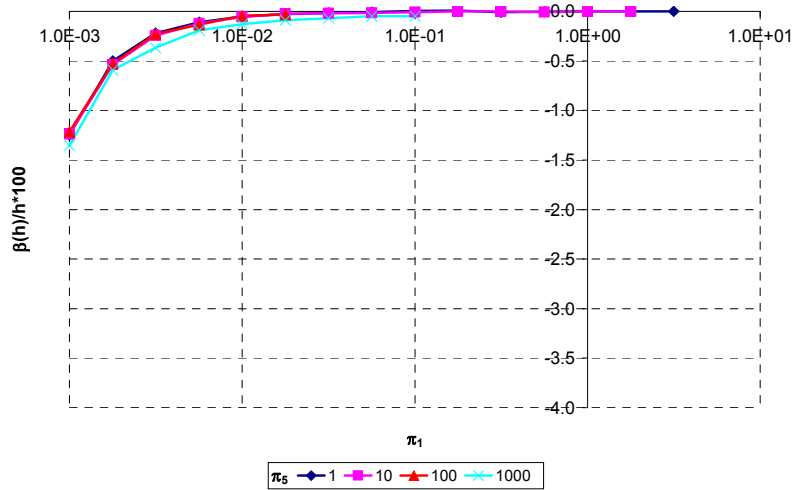
Figure 3.11 shows also the interesting result that it depends on t_{imm}/t_p rather than on the simple value of t_{imm} itself.



(a)



(b)



(c)

Figure 3.8: Percentage bias in the estimation of h for $\sigma_{noise} = 0.8K$.
 (a) $T_{aw} = 1,500K$, (b) $T_{aw} = 4,000K$, (c) $T_{aw} = 6,000K$. **NOTE:** the scale in (a) is different

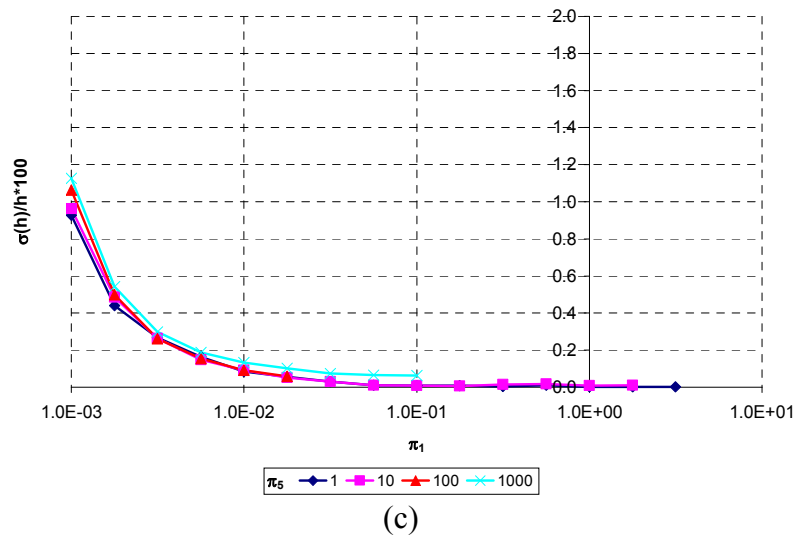
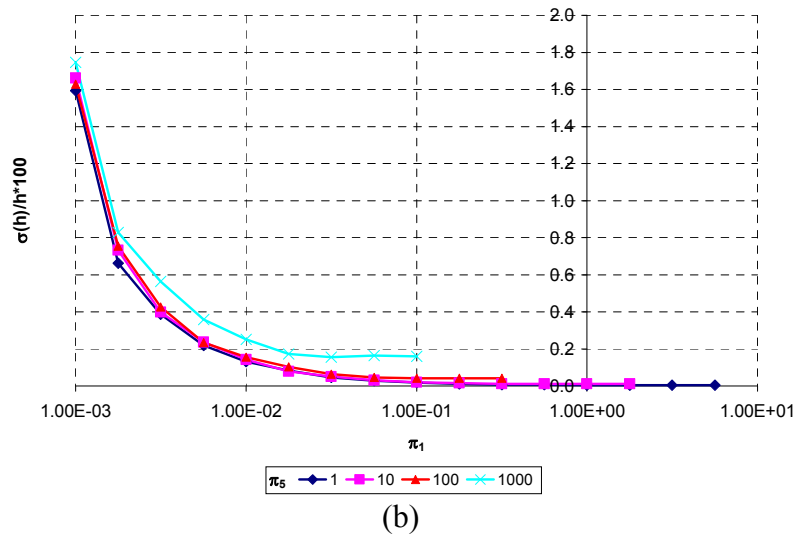
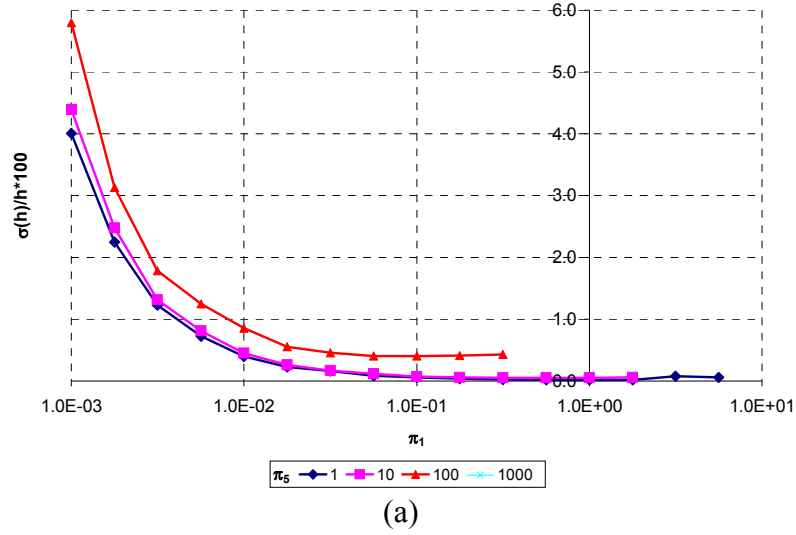


Figure 3.9: Percentage standard deviation in the estimation of h for $\sigma_{noise} = 0.8K$.
 (a) $T_{aw} = 1,500K$, (b) $T_{aw} = 4,000K$, (c) $T_{aw} = 6,000K$. **NOTE:** the scale in (a) is different

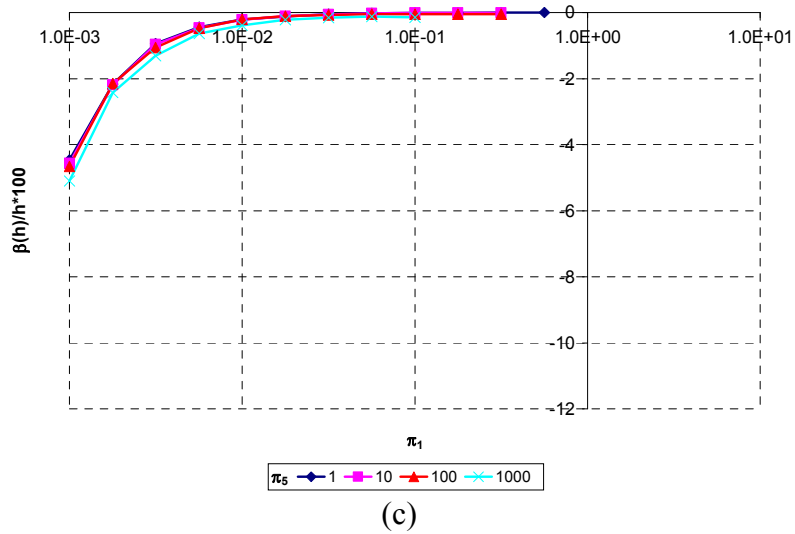
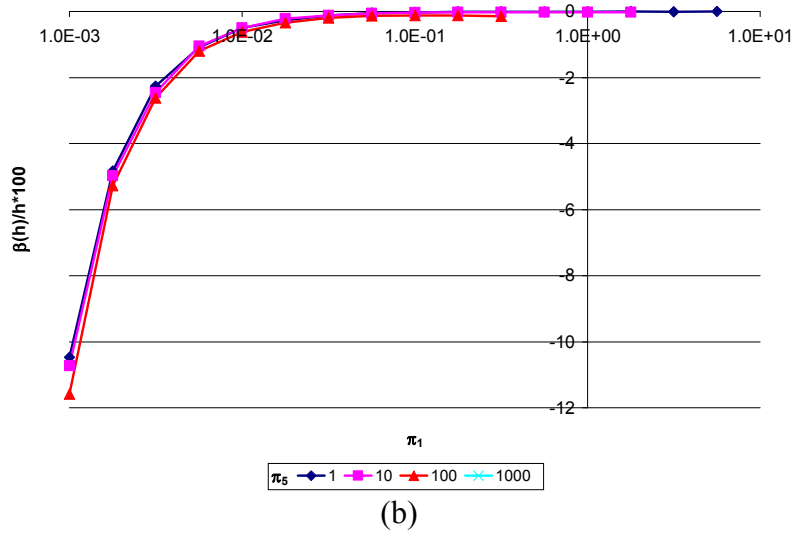
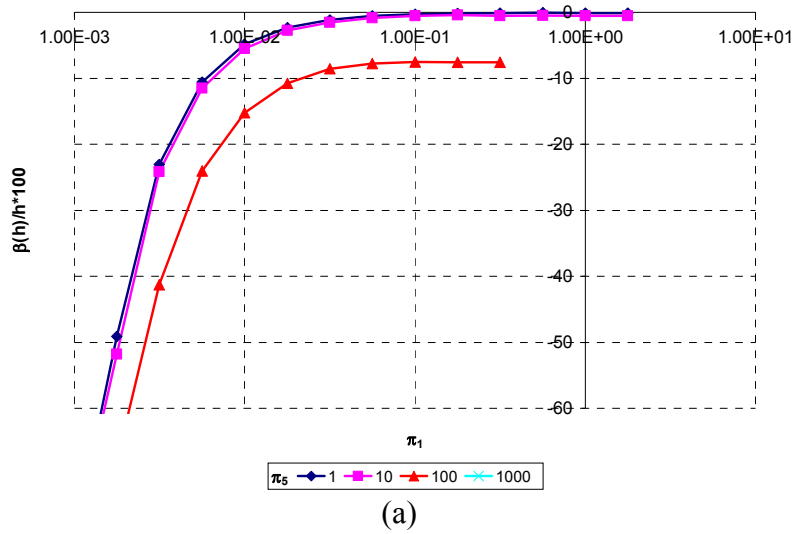
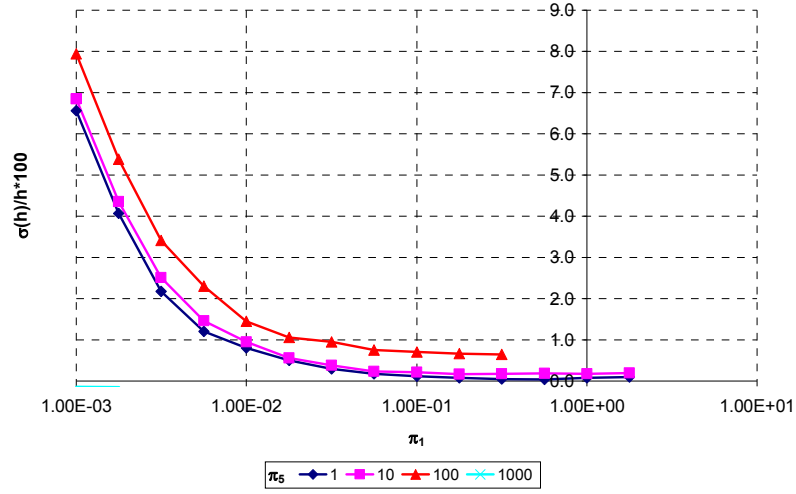
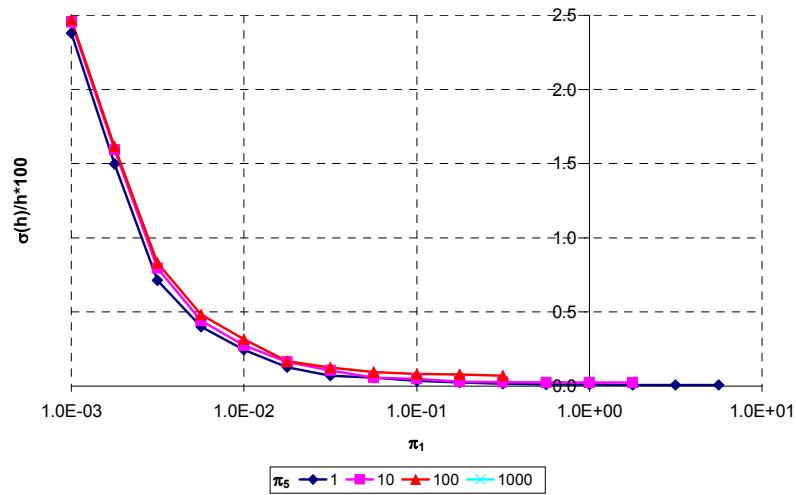


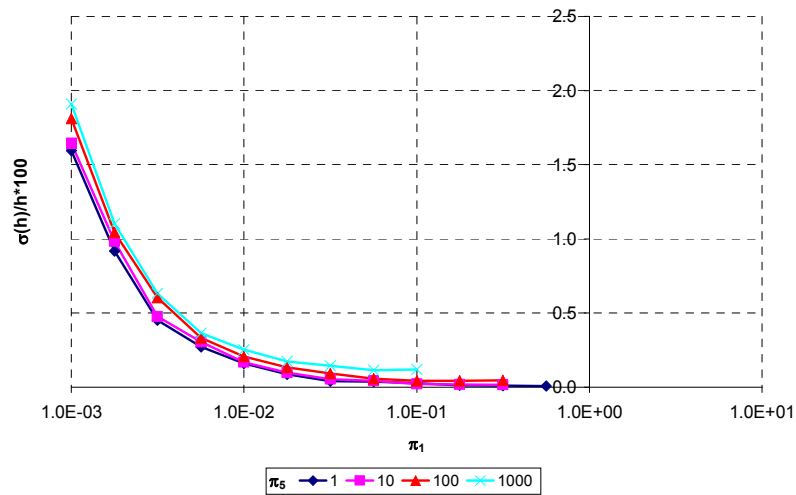
Figure 3.10: Percentage bias in the estimation of h for $\sigma_{noise} = 1.6K$.
 (a) $T_{aw} = 1,500K$, (b) $T_{aw} = 4,000K$, (c) $T_{aw} = 6,000K$. **NOTE:** the scale in (a) is different



(a)



(b)



(c)

Figure 3.11: Percentage standard deviation in the estimation of h for $\sigma_{noise} = 1.6K$. (a) $T_{aw} = 1,500K$, (b) $T_{aw} = 4,000K$, (c) $T_{aw} = 6,000K$. **NOTE:** the scale in (a) is different

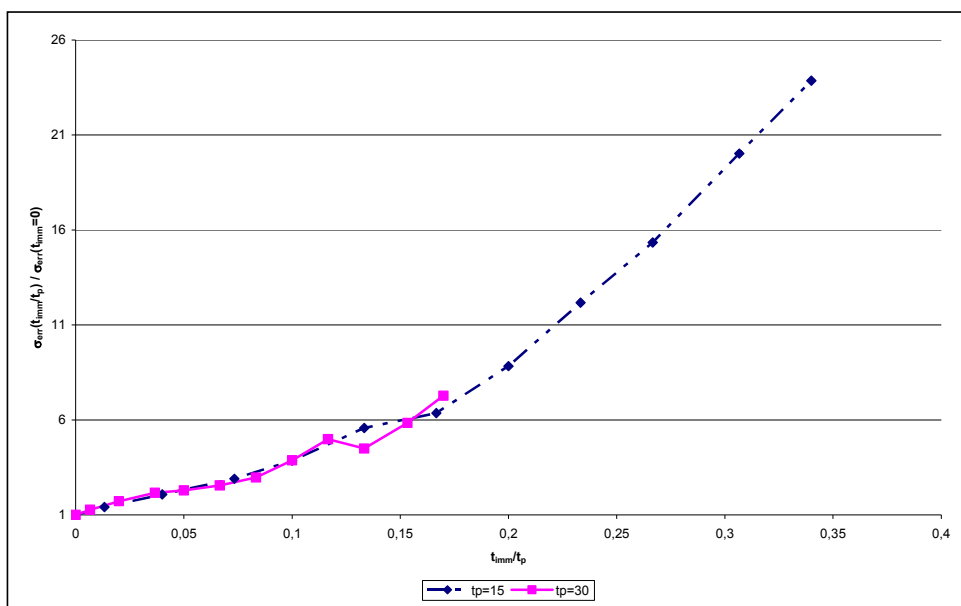


Figure 3.12: Influence of insertion time t_{imm}

3.8 Results: one-parameter optimization

The results illustrated in the previous paragraph have shown that the accuracy of the two-parameter optimization decreases as π_1 gets smaller and, even if this effect is limited when T_{aw} is high, lower adiabatic wall temperatures and high values of π_5 can influence significantly the results of the optimization, which in these conditions can easily fail. In presence of finite insertion times t_{imm} and of higher levels of noise the situation worsens.

The failure of the two-parameter optimization in such cases is due to the fact that, although in absence of noise the problem is still univocally determined and the optimization process is still able to estimate h and T_{aw} with no error, in presence of noise, even minimal, an infinite number of couples (h, T_{aw}) allows to generate numerical temperature rises which fit the experimental one equally well.

In this cases, separate estimation of the convection coefficient and of the adiabatic wall temperature is not possible, but it is still possible to reconstruct the temperature rise fixing T_{aw} to a reasonable value and estimating only h , as anticipated in §3.4.1. In this situation the optimization, when succeeding, will be able to estimate the correct surface heat flux $q_w(t)$ and the correct radiative contribution. The physical meaningfulness of the parameter h , on the contrary, will depend on how close the chosen value of T_{aw} is to the real one. From the discussion in §3.5 it can be recalled that low values of π_1 are characteristic of the tests with the smallest temperature rises per unity of time; these are tests with low total enthalpy H_0 , and it is therefore expected that T_{aw} will be close to T_0 .

The heat flux identification in such cases has been described as one-parameter optimization.

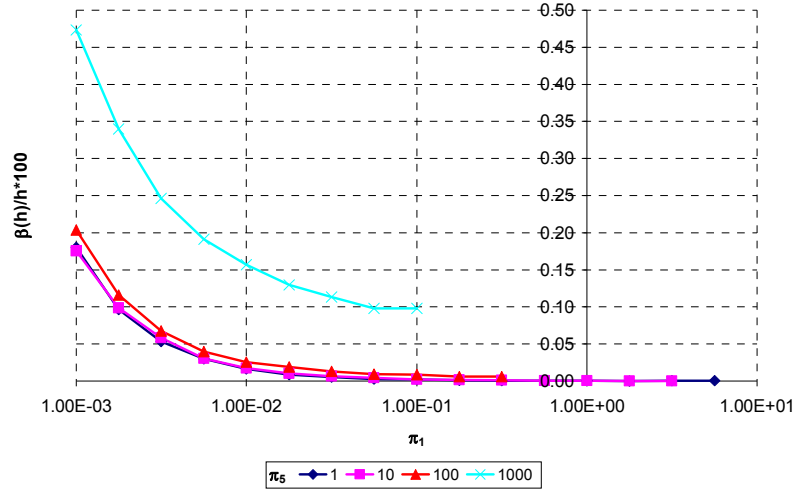
In this paragraph, as in the previous, the results are shown in terms of the parameter h . In this case, given that the surface heat flux $q_w(t)$ depends only on that parameter, the accuracy in the estimation of h is equivalent to the accuracy in the estimation of q_w .

Given that in one-parameter optimization T_{aw} is considered to be known and it must given in input to the program, for the diagrams shown in this paragraph the exact value of T_{aw} used in the generation of the “experimental” temperature rise has been chosen. This choice does not invalidate the generality of the results and it allows to express the results in terms of h .

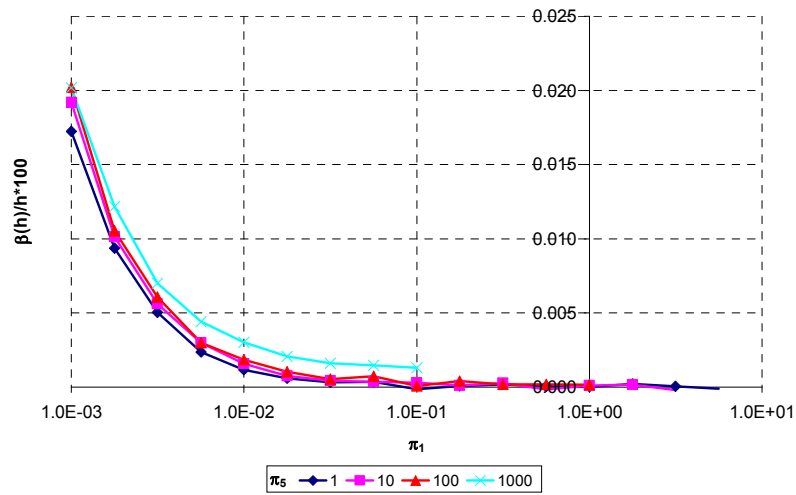
Figures 3.13 and 3.14 show the results of the validation when the noise added to the experimental temperature rise is $\sigma_{noise} = 0.8K$; figures 3.15 and 3.16 show the results for $\sigma_{noise} = 1.6K$.

The same results of the two-parameter validation can be noticed: optimal results are attained for higher T_{aw} and lower π_3 , and the optimization improves when π_1 is increased, although once an optimal value is reached further increases cause only negligible improvements in the optimization.

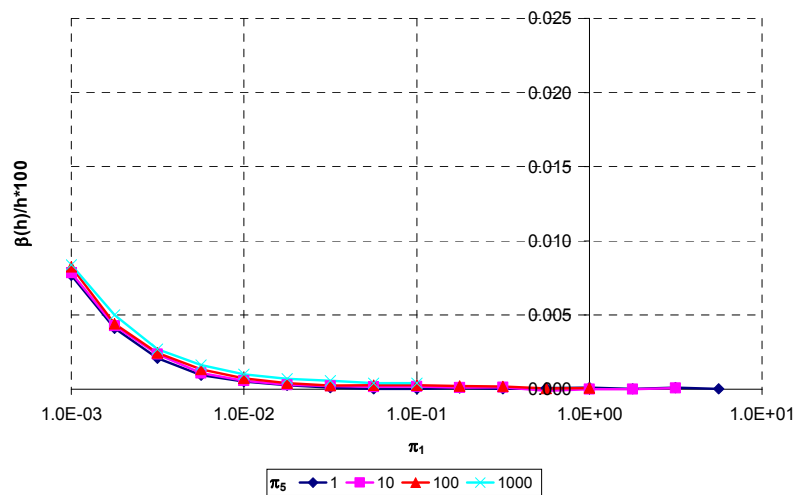
The main difference with the two-parameter optimization lies in the fact that the results are in this case significantly improved, and consequently imply the possibility to use the heat flux sensor for a larger range of variability both for π_1 and for π_2 , in particular for $\pi_1 < 1 \times 10^{-3}$. As expected, the one-parameter optimization can successfully be used in many of those cases in which the two-parameter optimization fails.



(a)

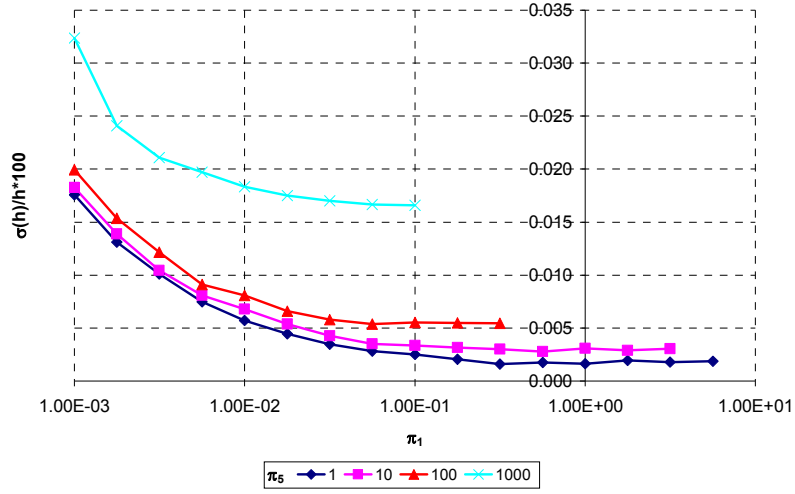


(b)

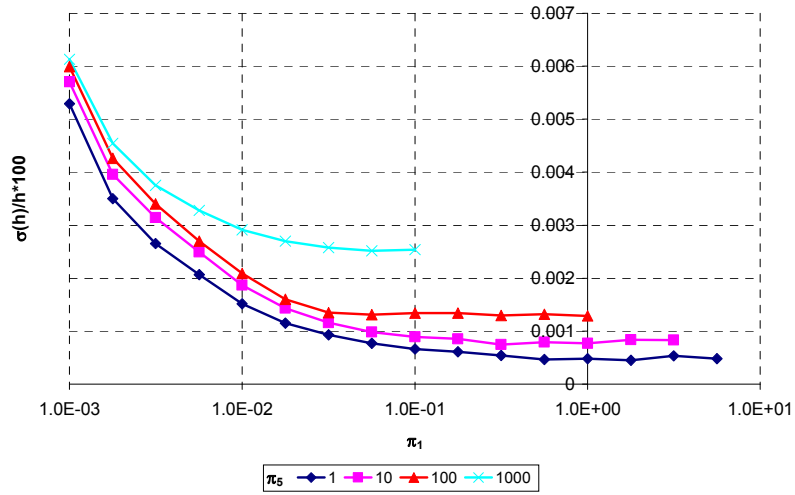


(c)

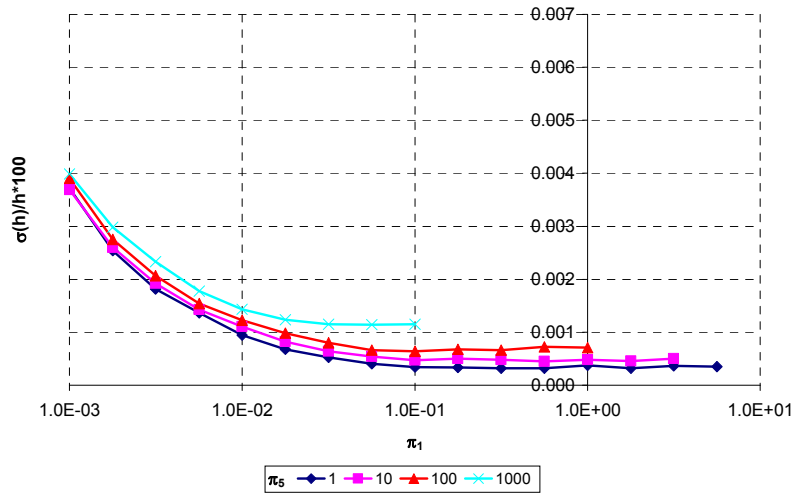
Figure 3.13: Percentage bias in the estimation of h for $\sigma_{noise} = 0.8K$.
 (a) $T_{aw} = 1,500K$, (b) $T_{aw} = 4,000K$, (c) $T_{aw} = 6,000K$. **NOTE:** the scale in (a) is different



(a)

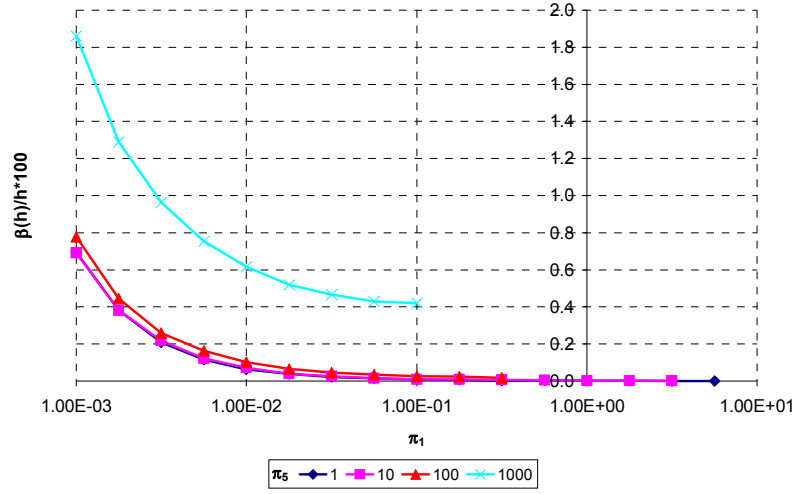


(b)

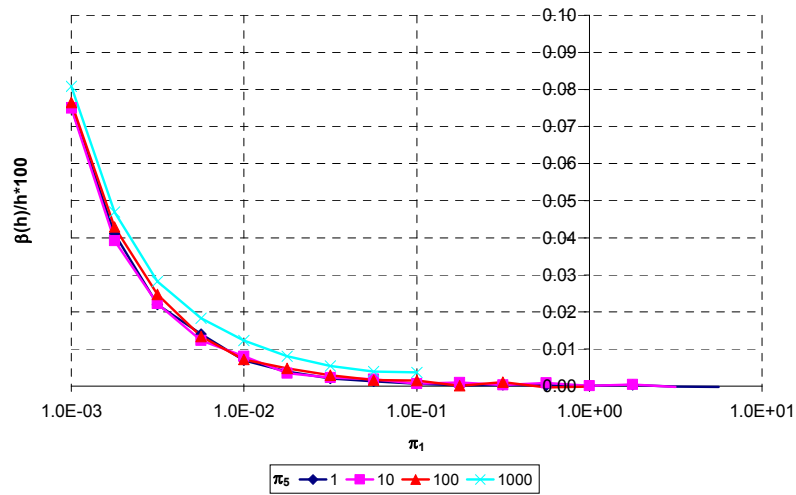


(c)

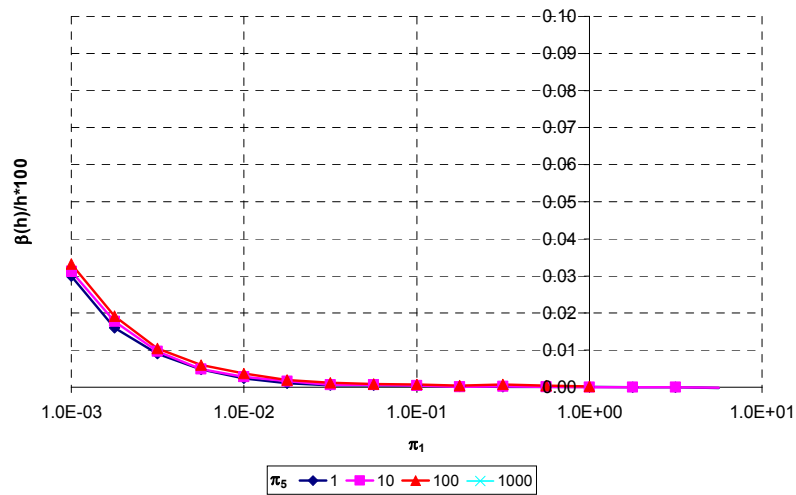
Figure 3.14: Percentage standard deviation in the estimation of h for $\sigma_{noise} = 0.8K$. (a) $T_{aw} = 1,500K$, (b) $T_{aw} = 4,000K$, (c) $T_{aw} = 6,000K$. **NOTE:** the scale in (a) is different



(a)

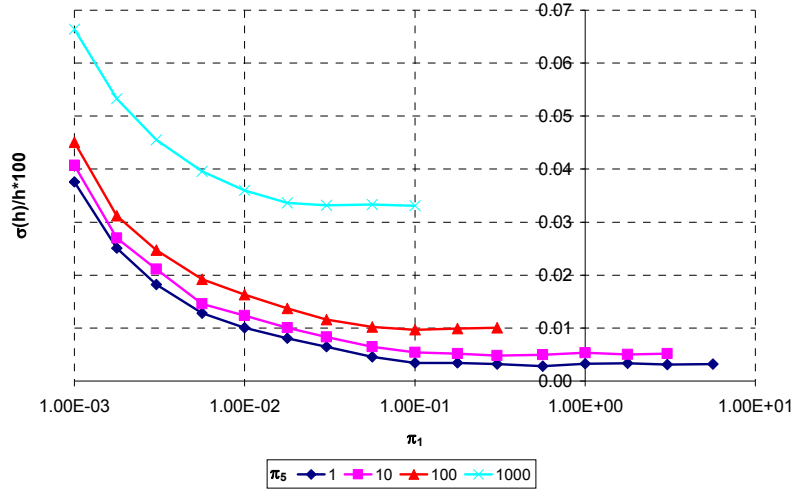


(b)

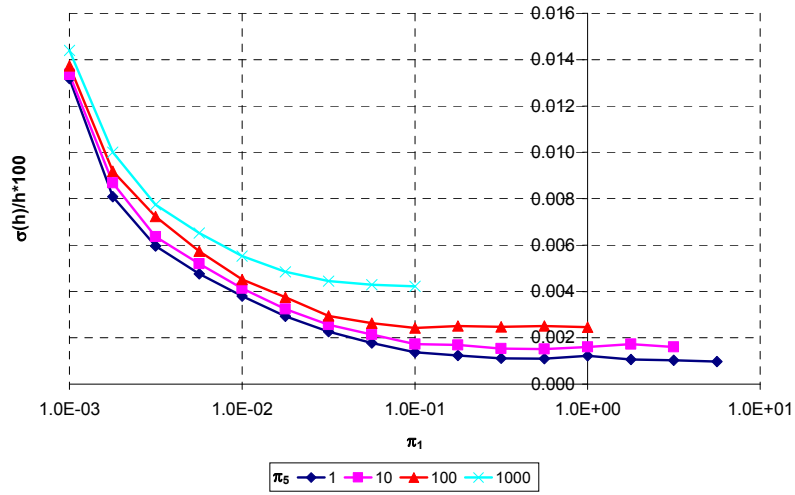


(c)

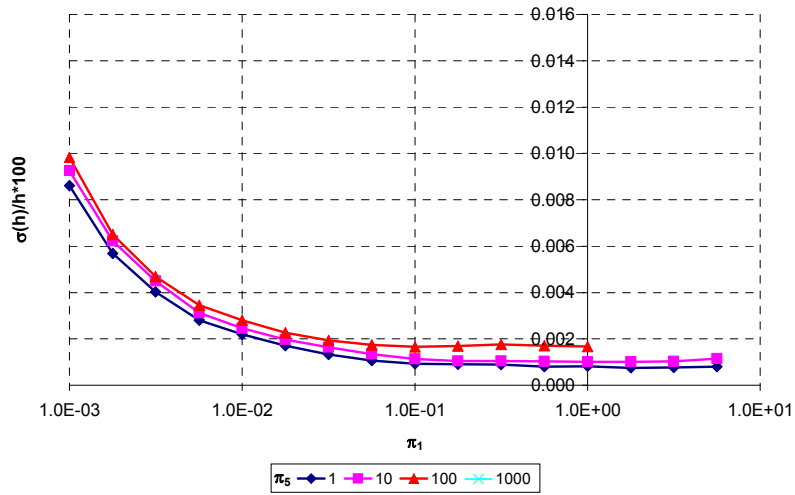
Figure 3.15: Percentage bias in the estimation of h for $\sigma_{noise} = 1.6K$.
 (a) $T_{aw} = 1,500K$, (b) $T_{aw} = 4,000K$, (c) $T_{aw} = 6,000K$. **NOTE:** the scale in (a) is different



(a)



(b)



(c)

Figure 3.16: Percentage standard deviation in the estimation of h for $\sigma_{noise} = 1.6K$. (a) $T_{aw} = 1,500K$, (b) $T_{aw} = 4,000K$, (c) $T_{aw} = 6,000K$. **NOTE:** the scale in (a) is different

3.9 Conclusions

In this chapter, the new heat flux sensor has been presented and validated numerically. The results of the validation have shown how the sensor can successfully be used in a wide variety of test configurations, either in its two-parameter or in its one-parameter optimization form. It has also been seen that its stated goals to allow accurate measurements in presence of finite insertion times and to improve its performance in terms of sensitivity to temperature measurements errors have been met.

In conclusion, it is worthwhile to report the list of criteria proposed by Beck (1985) to evaluate an inverse heat conduction procedure.

1. The predicted temperatures and heat fluxes should be accurate if the measured data are of high accuracy.
2. The method should be insensitive to measurement errors.
3. The method should be stable for small time steps or intervals.
4. Temperature measurements from one or more sensors should be permitted
5. The method should not require continuous first-time derivatives of the surface heat flux. Furthermore, step changes or even more abrupt changes in the surface heat fluxes should be permitted.
6. Knowledge of the precise starting time of the application of the surface heat flux should not be required.
7. The method should not be restricted to any fixed number of observations.
8. Composite materials should be permitted.
9. Temperature-variable properties should be permitted.
10. Contact conductances should not be excluded.
11. The method should be easy to program.
12. The computer cost should be moderate.
13. The user should not have to be highly skilled in mathematics in order to use the method or to adapt it to other geometries.
14. The method should be capable of treating various one-dimensional coordinate systems.
15. The method should permit extension to more than one heating surface.
16. The method should have a statistical basis and permit various statistical assumptions for the measurement errors.

An analysis of the discussion and results presented in this chapter shows how the new heat flux sensor meets all the relevant criteria.

In particular:

- a) The numerical validation has shown that the optimization results improve when the noise decreases, and in absence of noise the optimization program is capable to estimate the exact heat flux, with no error (points (1) and (2)).
- b) Points (8), (9), (14) and (15) are met because the problem is solved numerically, and the variability of material properties and the presence of composite materials has been implemented.
- c) Points (3) and (7) are met in that the use of thermographs with any frequency of acquisition f_s is allowed. The only limitation is that when the f_s is too small in relation to the test duration and too few samples are available, the optimization doesn't work. Furthermore, the use of a whole domain optimization technique made the method stable also for small time steps.
- d) Points (5) and (16) are met because of the very mathematical model and methodology on which the sensor is based and because of the appropriate choice of optimization routines.
- e) The use of the parameter *delay* has made it possible to use the sensor without knowing the exact moment in which the model starts to be exposed to the flux (point (6)).
- f) Contact conductances have not been considered, but can be easily implemented (point (10)).
- g) The method is very elaborated and it has therefore not been easy to program (point (11)), although future modifications can be implemented with a certain ease (as it will be seen in chapters 4 and 5, where slight modifications of the program were required to adapt it to the particular test configurations); furthermore, thanks to the configuration files used by the code program (see appendix 3), the program can be used in "blind mode", provided the phenomenology involved is understood (point (13)).
- h) The sensor requires the iterative solution of a non-linear differential equation. The computational cost involved in this is countered by the high accuracy and stability characteristic of whole domain estimation techniques (point (12)).
- i) Finally, the use of infrared thermography makes point (4) not relevant in this work.

CHAPTER 4: EXPERIMENTAL ANALYSIS – CAST TC-1A

4.1 Introduction: The CAST Project and the Test Case TC-1a

This experimental campaign was performed within the CAST (Configurazioni Aerotermodinamiche innovative per Sistemi di Trasporto spaziale – Advanced Aerothermodynamic Configurations for Space Transport) project funded by ASI, the Italian Space Agency. The purpose of this 4-year programme is the development of an advanced multidisciplinary simulation tool for aerodynamic, aerothermodynamic and aeroacoustic phenomena on space vehicles during ascent and re-entry phases. Several Italian research centres and university departments are involved in the project and, in fact, one of its goals is to realize a strong synergy among all the Italian experts in this field, creating a national consortium devoted to the study of aerothermodynamics.

One of the goals of CAST is also to create a dedicated experimental database in order to validate the numerical code with experimental data from several simple and complex Test Cases (TCs).

The Test Case object of this chapter falls within this framework and, in particular, is aimed at an analysis of the shock wave boundary layer interaction; this is a key phenomenon to be studied in the design of hypersonic vehicles both because of the high loads on the interested surfaces, and because it typically occurs over the control surfaces of hypersonic vehicles, where flow separation and recirculation can have significant effects on their efficiency; to emphasize these phenomena, a series of tests in the CAST project as an important part for the validation of the numerical code. A sharp double cone geometry has been selected for the early CAST test cases because this geometry has already been tested and the availability of previously obtained data allowed to design the experiment with a well established experience for both numerical computations and experimental techniques.

The CAST's Test Case on a sharp double cone within Alta's HEAT hypersonic tunnel (Test Case TC-1a) included surface temperature measurements both by means of IR thermography and with sensors on the double cone surface, allowing comparison between intrusive and non-intrusive temperature sensors. The gathered database is used for the numerical reconstruction of the experiment, that is carried out by CIRA and the DIASP department of Politecnico di Torino (PoliTO).

4.2 Hypersonic double cone flow

The hypersonic flow over a double-cone geometry is an interesting computational fluid dynamics (CFD) case because it produces many of the complex phenomena, such as shock interactions, triple points, and recirculation zones, that take place in flows past hypersonic vehicles. Double cone geometries have therefore been subject of extensive studies both experimental, in Calspan facilities (Holden, 2000, Holden & Wadhams, 2001) and in Princeton University facility (Wright et al., 2000), and numerical (Druguet et al., 2005, Nompelis et al., 2003, Wright et al. 2000).

A schematic description of the hypersonic flow past a double, following Druguet (2005), is given below.

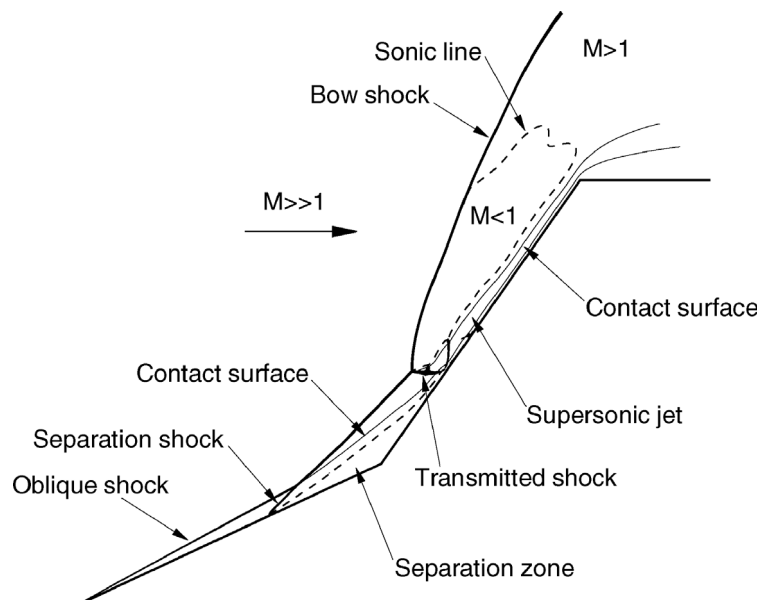


Figure 4.1: Schematic of the hypersonic flow past a double cone geometry (from Druguet, 2005)

The attached leading-edge shock wave interacts with a detached bow shock wave formed from the second cone, and this interaction produces a transmitted shock wave that impinges on the second cone surface, where very high surface pressures and heat transfer rates are consequently generated. Because of the high pressures at the impingement location, the flow separates near the cone–cone juncture and a recirculation zone develops, which in turn alters the shock interaction. The size of the separation zone is very sensitive to the shock angles and to the strength of the shock interaction. Downstream of the shock impingement location, a supersonic jet develops near the second cone surface.

Under a thermodynamic point of view, the points of greatest interest are the separation zone around the two cones and the reattachment on the second zone; these should be clearly

visible both on thermal and in heat flux maps, because the recirculation involves reduced heat transfer, and consequent reduced surface heating), while a peak in heating is obviously expect at the reattachment point.

4.3 Experimental apparatus

4.3.1 The HEAT facility

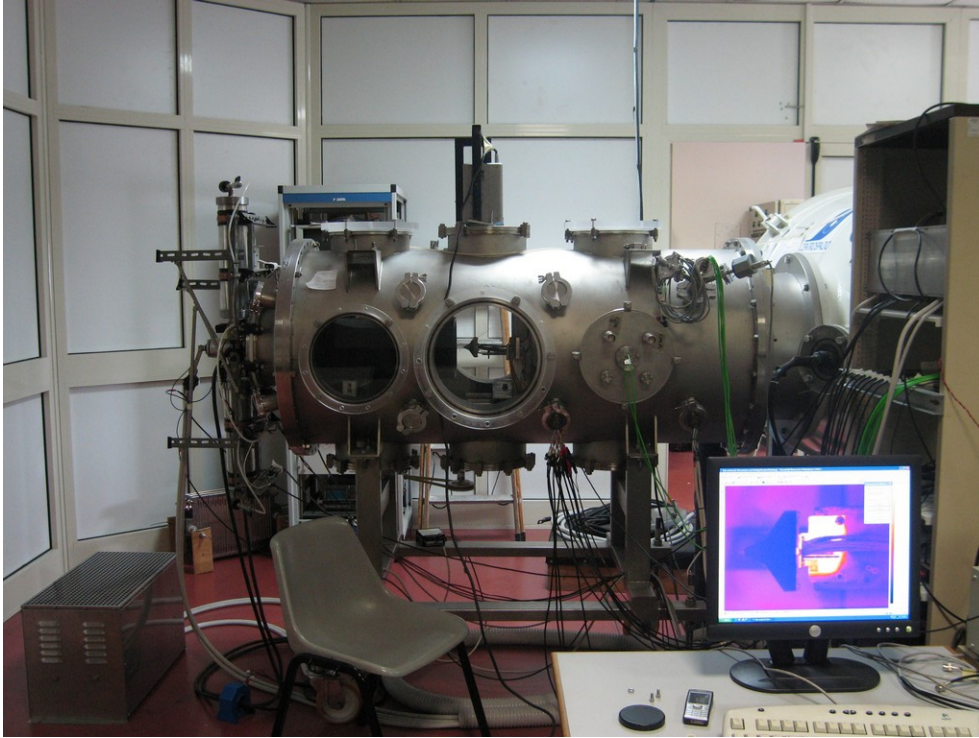


Figure 4.2: The HEAT facility in ALTA (Pisa). It is possible to see the thermograph mounted on the top of the wind tunnel, the model inside the test chamber and a thermographic image of the model

The TC-1a has been performed in the High Enthalpy Arc-heated Tunnel (HEAT), Alta's small hypersonic wind tunnel (figure 4.2), operative since 1996 in the medium-low Reynolds number range. The flow total pressure in air can vary typically between 1 and 9 bar, with total enthalpy up to 6 MJ/kg . Two contoured nozzles can be used in air to produce Mach 6 and Mach 9 flows, and the Mach 9 nozzle includes a series sensors on its lateral walls to allow pressure and temperature measurements during the gas expansion.

The total vacuum volume is of about 4.5 m^3 and the test section is accessible from several windows allowing the visual and instrumental monitoring of the experiment from eight different directions. The arc discharge is powered by a 260 kW DC power supply with peak values of voltage and current of 650 V and 630 A . Two tanks inject the gas in the plenum chamber through fast solenoid valves. Sensors are installed in order to monitor in real time the pressure both in the plenum and in the test chamber as well as the arc parameters. The

performances of the facility allow a typical test time of 50-300 ms , limited only by the vacuum chamber back pressure.



Figure 4.3: The instrumented Mach 9 nozzle

Finally, a dedicated flange with a Germanium window is installed above the model for use with IR thermography. The window, inclined with respect to the axis of observation to avoid any reflection on the camera, is coated for the long wave range (8-14 μm) with minimum absorption in the temperature range of 296-1000 K in which the double cone emits.

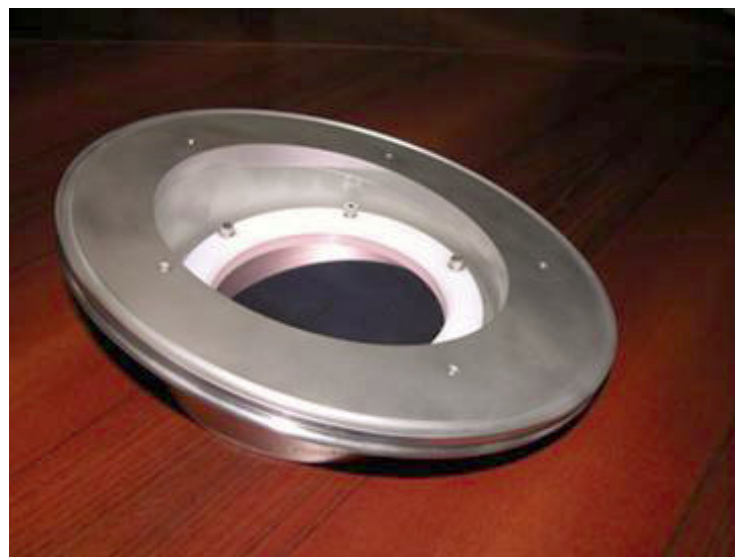


Figure 4.4: The inclined flange with the Germanium window

4.3.2 The thermograph

A FLIR SC3000 thermograph has been used for temperature measurements. A list of the main characteristics of the SC3000 can be found in §1.5. It is here remarked that the

frequency of acquisition f_s is 60 *Hz* when full 320×240 frames are recorded, but it can rise up to 300 *Hz* if the dimension of the frame is reduced to 320×48.

The typical test duration t_p for TC-1a are about 150 *ms*. If a full frame had to be recorded, the recorded temperature rise would be made of up to 9 experimental points. This number is far too small for heat flux identification, and therefore the highest frequency of acquisition has been chosen, to obtain temperature transients made of up to 45 points, which proved to be enough for proper functioning of the heat flux sensor.

The reduced frame size imposed by the high frequency of acquisition, although resulting in IR images not covering the entire width of the cone (see figure 4.12 later in this chapter), didn't hamper the possibility to see its whole axial length. It is also noticed that measurements from the edges of the cone need in any case to be discarded because of the high angle of view between the thermograph and the surface of the cone (cf. §4.4.2 and §4.8). The smaller frame has therefore proved to be optimal for thermographic measurements and heat flux identification in this experimental campaign.

4.4 Test article design

4.4.1 Geometry

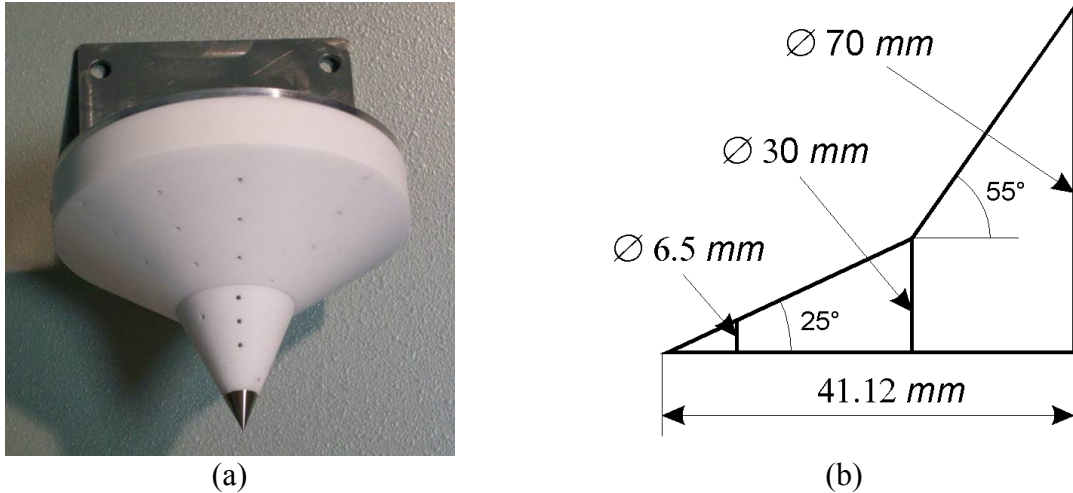


Figure 4.5: The TC-1a double cone model; (a) Picture; temperature and pressure sensors are clearly visible. (b) Sketch with dimensions

The model expressly designed for the TC-1a has an internal aluminium structure covered by a MACOR[®] shell of 1.5 mm of thickness. The sharp leading edge was made of stainless steel in order to avoid erosion during the experiments and to keep the conic shock wave attached.

The same test case described in Druguet (2005) has been chosen to permit the comparison with existing data for both experimental tests and numerical simulations. The geometry, shown in figure 4.5, is therefore characterized by semi-aperture angles of the cone of 25 and 55 degrees. The linear dimensions have instead been scaled in order to place the whole model within the core flow with uniform Mach number of the Mach 9 nozzle. The base diameter of the first cone and of the second cone have been set, respectively, to 23 mm and 70 mm, whereas the same measurements for the cone described by Druguet were 84.5 mm and 257.8 mm with a total length of the cone of 151.3 mm.

The base diameter of the stainless steel tip, on which thermographic measurements are not possible, has been set to 6.5 mm

Pressure sensors and thermocouples, whose positions are clearly visible in Fig. 1, have been placed on four different radial sections, in order to allow the axial symmetry verification. The axial position were chosen in order to maximise the chance of correct identification of the shock-shock interaction on the double cone as expected from the design simulations.

4.4.2 Material

The implementation the new heat flux sensor requires a full characterization of the material constituting the model, both under a thermal and a radiative point of view.

As mentioned in the previous paragraph, the test model is made of MACOR[®], which is a machinable glass ceramic manufactured by Cornig Inc. MACOR[®] is a thermal insulator with high emissivity, and is therefore ideal for use both with IR thermography and as a substrate for thin film gages.

Although widely used in aerospace applications, the thermal characteristic of MACOR[®] and their variation with temperature is not well documented, and the sources available in literature are not in good agreement between them. Hollis (1995) has reviewed existing literature and has calculated curve fits for most recent available data. These curve fits are shown below

$$\begin{cases} \rho = 2543.84 - 8.0 \times 10^{-12} \cdot T \quad [kgm^{-3}] \\ c_p = 114.04 + 2.5196 \cdot T - 1.5136 \times 10^{-3} \cdot T^2 \quad [Jkg^{-1}K^{-1}] \\ K = 0.3389 + 7.4682 \times 10^{-3} \cdot T - 1.6118 \times 10^{-5} \cdot T^2 + 1.2376 \times 10^{-8} \cdot T^3 \quad [Wm^{-1}K^{-1}] \end{cases} \quad (4.1)$$

Given the uncertainty in available data, and given the limited temperature span involved in TC-1a (with peaks of about 150 °C on the surface of the model at reattachment, and much lower anywhere else) it has been preferred to consider the variations of thermal characteristic with time negligible. This choice will also allow a better comparison with data reduction with the classic thin film sensor, which doesn't take material variations with temperature into account.

The thermal properties of MACOR[®] at ambient temperature are available from Cornig⁷ and are:

$$\begin{cases} \rho = 2,520 \quad [gm^{-2}] \\ c_p = 790 \quad [Jkg^{-1}K^{-1}] \\ K = 1.46 \quad [Wm^{-1}K^{-1}] \end{cases} \quad (4.2)$$

As regarding the surface emissivity ε of MACOR[®], it strongly depends on surface finishing, and can therefore strongly vary from one lot to another; data available in literature are therefore not reliable, and calibration of emissivity is needed; the calibration is also needed to calculate directional emissivity, which is not available in literature but can play a

⁷ MACOR[®] brochure, www.cornig.com

crucial role in the present case because of the high angles of view involved, especially with regards to the 55° cone.

A full calibration of directional emissivity has been performed at the DIAS laboratory, following the procedure explained in §1.7, and the results are shown in figure 4.6.

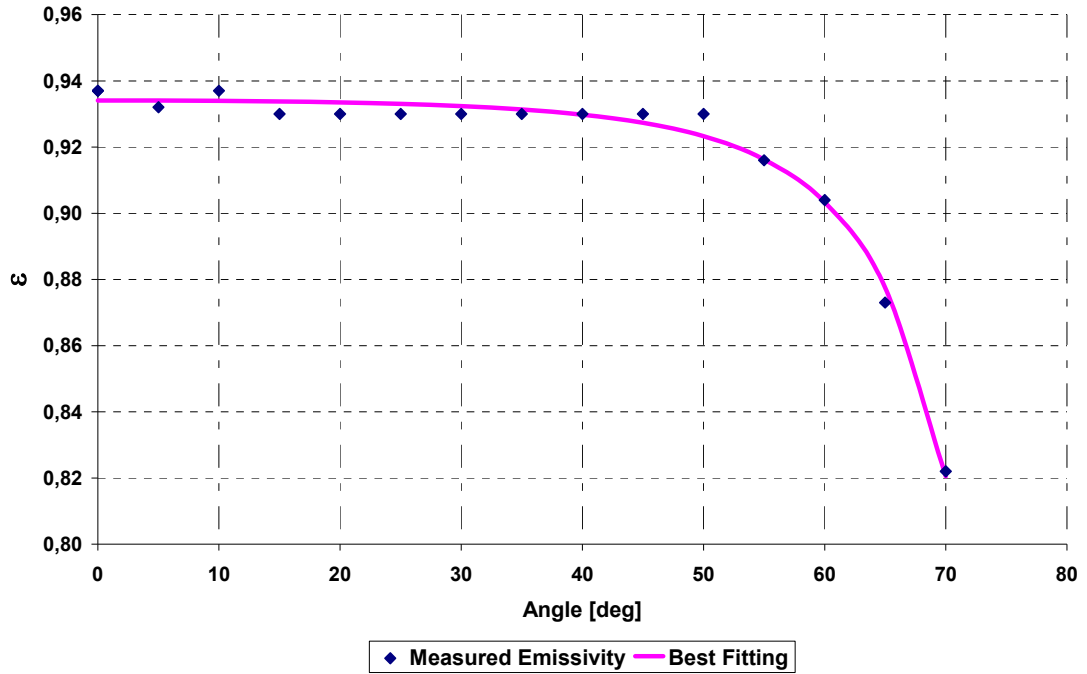


Figure 4.6: Directional Emissivity of MACOR®.

The equation describing the emissivity as a function of the angle of view is given by (1.15), shown again below

$$\varepsilon = \varepsilon_0 \cos(\theta)_{\cos(\theta)^b}^a \quad (4.3.a)$$

The parameters ε_0 , a and b are found via best fitting:

$$\begin{cases} \varepsilon_0 = 0.934 \\ a = 9.8 \times 10^{-3} \\ b = 2.4 \end{cases} \quad (4.3.b)$$

4.5 Design of the target

The design of the target needed for the geometrical reconstruction described in chapter 2 is strictly linked with the test in which it has to be used. In particular, it must take into account the dimensions of the model, the resolution of the thermograph and the distance of the camera from the model. Finally, the markers must be clearly visible by the thermograph.

Experience has shown that, for the Tsai calibration program to work properly, the markers need to include at least four pixels on the IR image. Starting from this project constraint, and from the design parameters and constraints mentioned above. The parameters of interest are:

- Maximum dimension of the IR image: 320×240 pixel,
- Aperture of the lens on the SC3000: $25^\circ \times 20^\circ$
- Distance of the SC3000 from the model: ~ 500 mm

These data allow to calculate the spatial resolution on the surface of the model, which is about 0.5 mm and that a maximum total area of 16×12 cm will be seen, although only a part of this image will be actually occupied by the model (see figure 4.12). Starting from these measurements and considerations, the dimensions of the target can be set. A 12×12 cm flat slab with thermal markers of 2.2 mm diameter has been chosen.

Once the measurements have been defined, the materials for the slab and for the markers must be chosen. To be visible, thermal markers need to have as large a different emissivity as possible from that of the slab. The choice to have high emissivity markers on a low emissivity slab is made, on the basis of considerations on the ease of manufacturing.

A surface of polished aluminium has been chosen as background, and the markers have been realized by drilling holes of 10 mm of depth in it. Holes whose depth is more than 4 times the diameter behave as black bodies because, thanks to the fact that multiple reflections inside the hole let emerge from it only a tiny part of the incident radiation.

The target can be heated quickly and very easily, thanks to its small dimensions and to the high conductivity of the aluminium. When the target is heated, the thermal markers will be clearly seen as hot spots on a cold surface. A picture of the target is shown in figure 4.7, and its thermal map in figure 4.8.

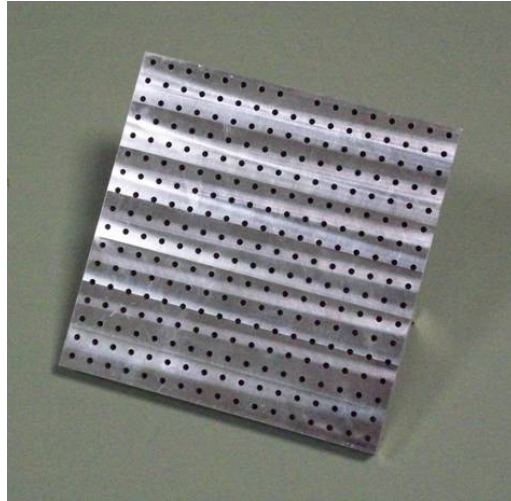


Figure 4.7: Picture of the target. The missing marker at the top of the picture is used to locate the array of markers on the IR image.

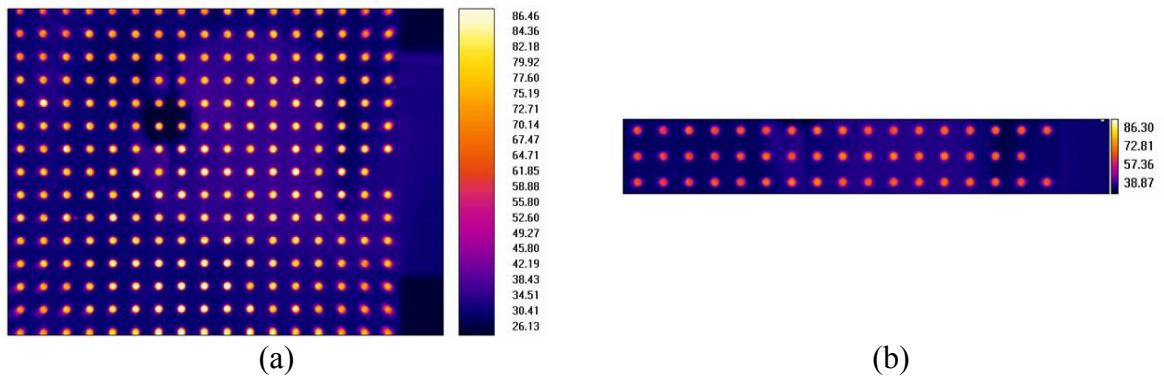


Figure 4.8: IR image of the target. (a) full resolution (320×240 pixel); (b) 320×48 pixel, which is the resolution actually used during the experiments.

The target is also used to set a reference frame for space coordinates, because each point in this reference frame can be identified on the IR image. For this to happen, the test model needs to be referenced in the system generated by the target, and the position on the target of at least one point of the cone must be known. With this goal in mind, the target has been designed in such a way that the vertex of the cone coincides with the centre of one of the thermal markers when the target lies on one of its calibration planes.

It is noted that the resection process has a sub-pixel precision, and it is impossible to locate points of the cone on the IR image by visual inspection.

4.6 The test campaign

The experiments were carried out with synthetic air flow (80% N₂, 20% O₂) with nominal conditions for total pressure ($p_0 = 3 \text{ bar}$) and total enthalpy ($h_0 = 4.5 \text{ MJkg}^{-1}$).

About 30 runs were performed during test campaign; hereinafter TC-1a runs will be named according to test day and run number, as in 13-3_#3.

In table 4.1 the test conditions for two runs are shown, along with conditions for the test case reported in Druguet (2005) (Calspan), which is here reported because it will be used for comparisons later in this chapter.

Test	Mach	h_0 [MJkg^{-1}]	T_0 [K]	ρ_∞ [kgm^{-3}]	u_∞ [ms^{-2}]	Re_∞
Calspan	11.3	3.8	2,711	5.5×10^{-4}	2,713	1.33×10^5
TC-1a nominal	9.00	4.5				
12-3_#8	9.17	4.5	2,781	2.0×10^{-4}	2,472	4.15×10^4
13-3_#3	9.35	4.6	3,210	2.2×10^{-4}	2,679	4.57×10^4

Table 4.1: Sample test conditions

4.7 Experimental Problems

Two kinds of experimental problems have been experienced;

- 1) All the runs were characterized by a high level of noise. As figure 4.9 shows, this noise was mainly due to an elevated number of sparkles, possibly originated by the cathode. This has been cause of extremely noisy temperature measurements, whose filtering is somewhat difficult, owing to the limited number of measurements forming a temperature rise (typically, about 50); also space averaging of the measured temperature was of little use in those cases in which a sparkle hit the surface, because in this case the zone interested by the perturbation was very large. No filtering technique has therefore been implemented, and the presence of noisy data proved to be a good test ground for the new heat flux sensor.



Figure 4.9: Photograph of the model during a run. Sparkles released by the cathode can be seen

- 2) The other significant problem encountered during the tests regarded the stagnation temperature, which has rarely been constant during the tests. Figure 4.10 shows a particularly critical test, during which the arc ignited twice. This problem has proved to be particularly critical because the experimental temperature rise is completely different from the theoretical temperature rise predicted by the mathematical model (3.12)-(3.13) and this makes the curve fitting to all extents impossible; as an example see figure 4.11 where two temperature rises generated using the experimental and averaged stagnation temperatures shown in figure 4.10 are drawn.

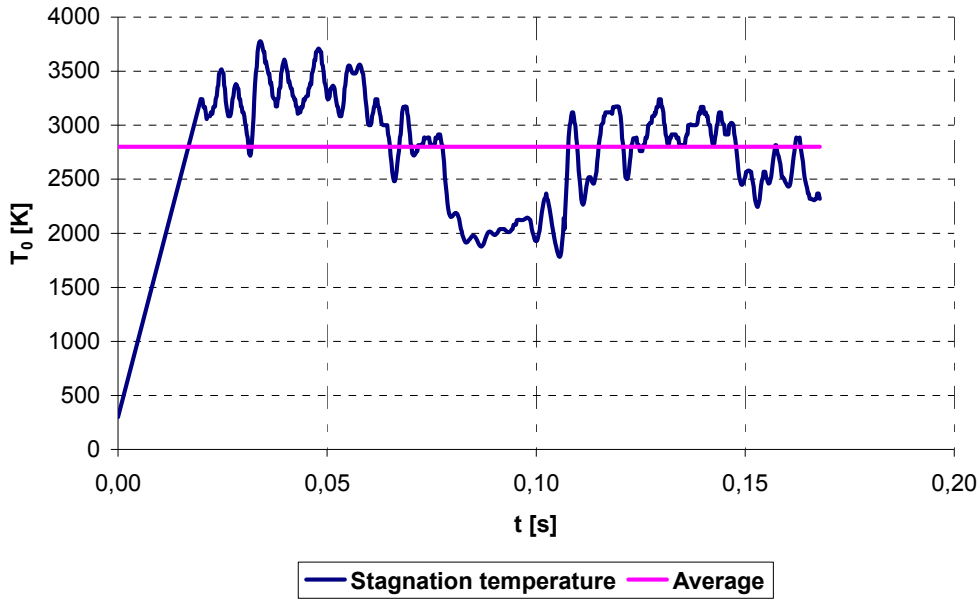


Figure 4.10: Stagnation temperature for run #13-3_12. In this particular case a double ignition of the arc can be noticed.

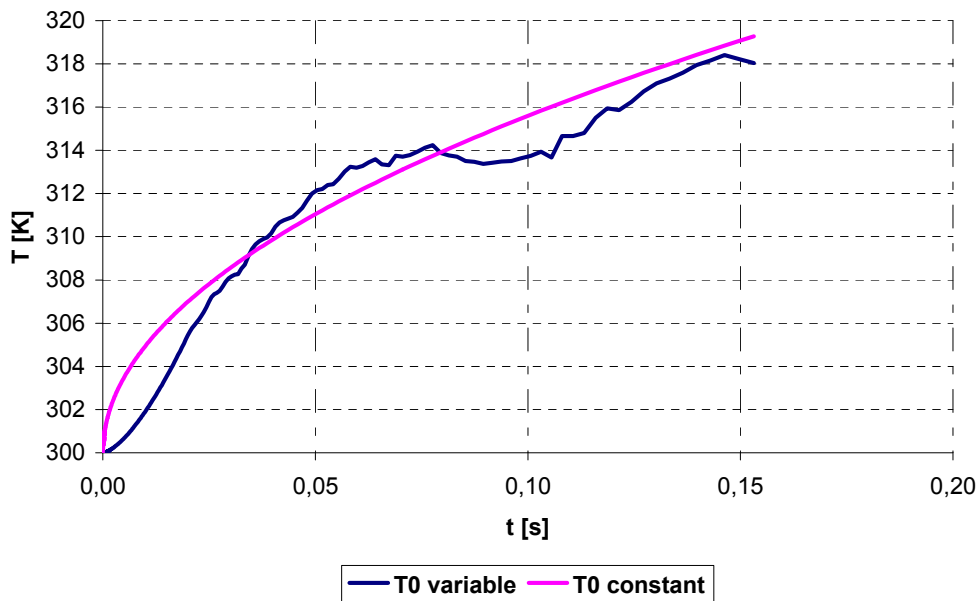


Figure 4.11: Temperature rises generated with the stagnation temperature shown in figure 4.10

The non-constancy of the stagnation temperature has led to the need to implement a modified version of the heat flux sensor, as it will be seen in §4.8.

4.8 Transient temperature measurement

The technique used in this work to measure temperature transients on the surface of a body by means of IR thermography has been described in general terms in chapters 1 and 2. The practical implementations of this technique requires several steps which are described in detail below.

- 1) *Acquisition of a time sequence of IR images.* These images are recorded by the SC3000 thermograph at a frequency of 300 Hz; the thermograms in this case are 320×48 pixel, and each pixel contains information about the intensity of radiation I_U related to that pixel; this information needs to be further elaborated to calculate the temperature. In figure 4.12 an IR image of the model is shown.
- 2) *Thermograph calibration.* The thermograph has been calibrated following the process described in §1.6; the calibration in this case is needed to take into account the absorption of radiation in the optical path between the thermograph and the model. In this case, the germanium window shown in figure 4.4 is present and, although the germanium is almost transparent to the radiations in the operative wavelength range of the SC3000, a calibration is advised. The calibration has been performed in the DIAS laboratory.
- 3) *Generation of a mesh on the surface of the cone.* The double cone geometry is quite simple to discretize, and a mesh of square elements has been generated. The mesh spacing has been chosen to be just slightly higher than the spatial resolution of the thermograph, in such a way to avoid both loss of information and useless extra points adding no further information but causing heavier computational load. As shown in figure 4.6, the emissivity of MACOR[®] decreases dramatically for angles of view θ higher than 60°; as a consequence, the mesh has been generated only on limited sector of the double cone, $-15^\circ < \theta < 15^\circ$ where θ is the angle from the vertical, and the other points of the surface cone seen by the thermograph have not been used for temperature measurements. Figure 4.13 shows the mesh built on the cone.
- 4) *Tsai calibration.* To estimate the 12 constants needed for geometrical reconstruction, several images of the target from planes at different distances from the thermograph are needed. The target has been mounted on the same support used to hold the model, and images from 13 different planes have been taken, for a total of 663 points (markers) of known spatial position recorded and given in input to the Tsai calibration program to get the constants in output.

- 5) *Geometrical resection*. the Tsai constants are used to establish a correspondence between the points of the mesh and points of each of the IR images of the sequence. Figure 4.14 shows a thermographic image of the model with the projection of the points of the mesh (figure 4.13) superimposed.
- 6) *Emissivity mapping*: the Tsai constants give also the relative position of camera and model, and they are used to calculate the angle of view between the camera and the surface on each point of the mesh. Once the viewing angles are known, the emissivity of the model on each point of the mesh is calculated with equation (4.3). A map of emissivity is shown in figure 4.15.
- 7) *Temperature calculation*: Finally, information gathered in steps (2)-(6) are used to calculate temperatures on each point of the mesh for each time step starting from the IR images recorded in step (1) and using equation (1.10) with $\tau = 1$.

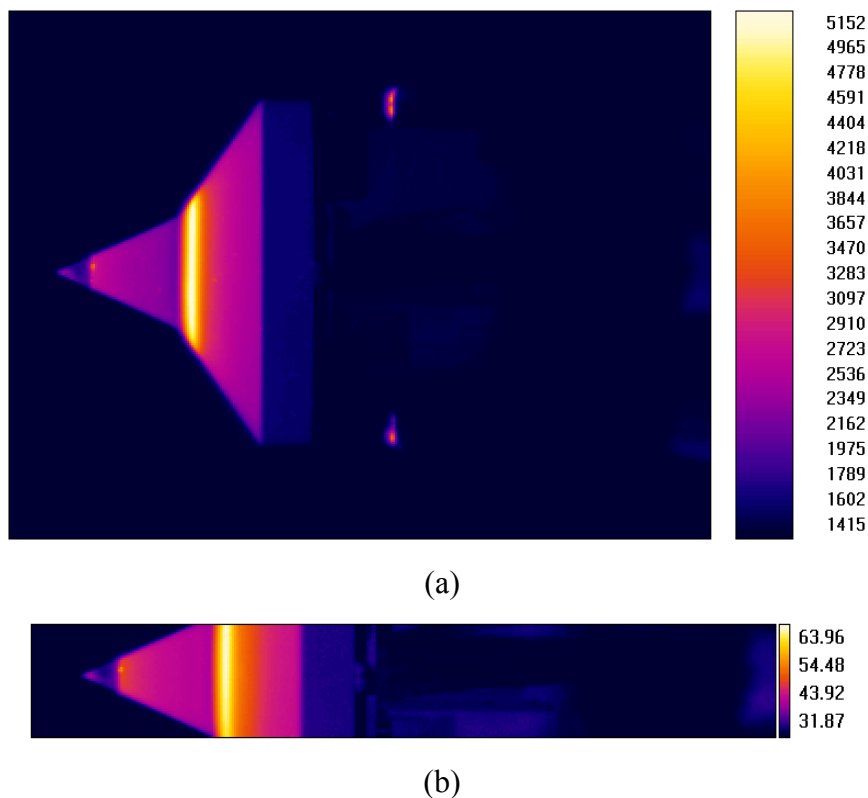


Figure 4.12: Thermograms. (a) Full frame 320×240; (b) 320×48. The images used for heat flux reduction have all been 320×48 because the low frequency of acquisition required for full frame (60 Hz) implies a number of samples of the temperature rise (about 6) which is too small for use by the optimization program

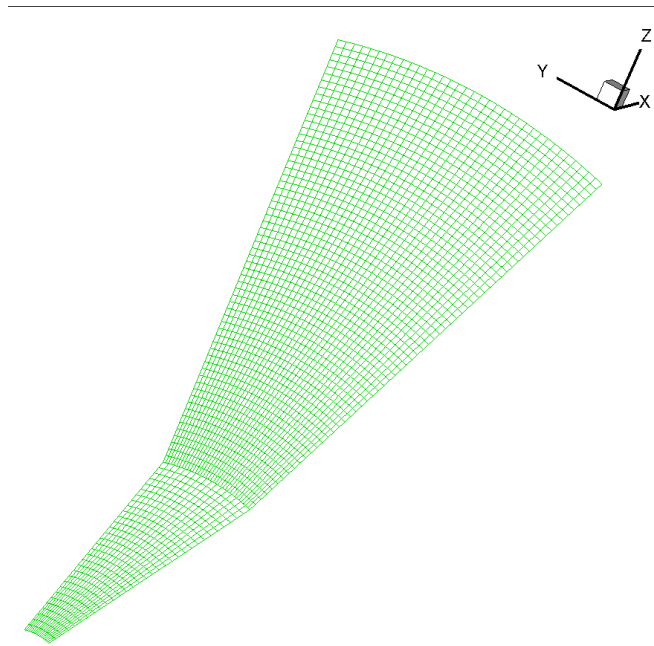


Figure 4.13: Square mesh on the double cone. Only a sector of 30° around the z axis is considered and, of course, the stainless steel tip is not meshed

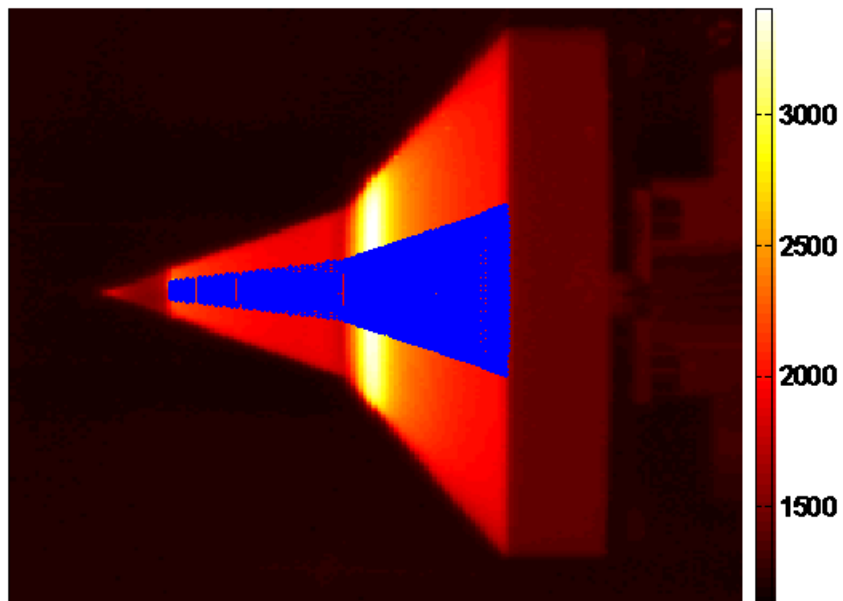


Figure 4.14: The mesh of figure 4.13 projected on the plane of the IR image 4.12a

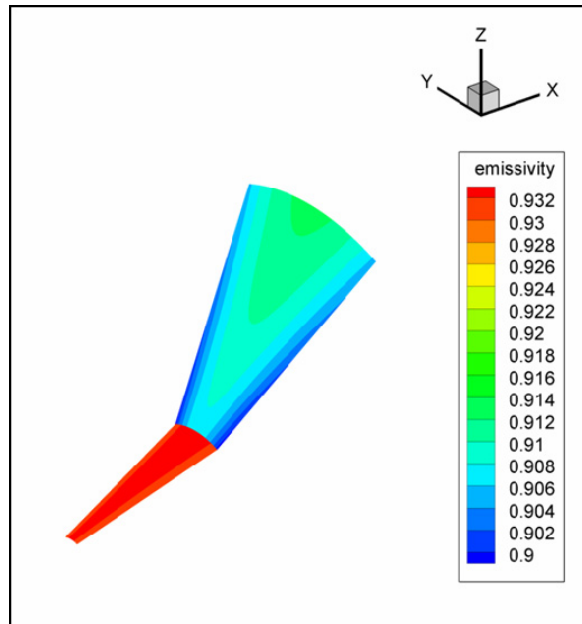


Figure 4.15: Emissivity map

The temperature measurements performed with the method described in this paragraph will be illustrated in detail in §4.10.

4.9 Heat Flux measurement

Heat flux measurement are performed by the new heat flux sensor starting from the temperature measurements illustrated in §4.8.

A preliminary check is needed to verify if the sensor is usable for this particular test case and, should that be the case, whether two-parameter estimation (cf. §3.4.1) can be used. For this purpose it is necessary to estimate the values that the adimensional parameters (3.17) can attain in this test campaign; these values are calculated from approximated known or expected values for model properties and test conditions. In particular, from the nominal test conditions (see §4.6), it is possible to infer the expected values for T_0 and h ($T_0 \cong 3,000\text{ K}$, $h \in (20,150)$ on different points of the model); the thermal properties of the material are taken from (4.2) and for the emissivity the approximate value $\varepsilon = 0.93$ is chosen (cf. equation (4.3)). Finally the test time is $t_p \cong 150\text{ ms}$. Starting from all these assumptions and measurements, the expected values for π_1 and π_2 are calculated:

$$\begin{cases} 2 \times 10^{-5} < \pi_1 < 1 \times 10^{-3} \\ 10 < \pi_2 < 70 \end{cases} \quad (4.4)$$

where the higher values for π_1 are reached only at the reattachment point.

From the results of §3.7 it is seen that the values attained by π_1 are very low; if the further problem of the extremely noisy temperature measurements is considered (see §4.7), it is evident that conditions for 2-parameter optimization are nowhere met, so 1-parameter optimization will be used.

The thermal properties (4.2), along with the thickness of the model ($L = 1.5\text{ mm}$, see §4.4.1) are useful to calculate the Fourier number:

$$Fo = 4.9 \times 10^{-2}. \quad (4.5)$$

This value is low enough to make the assumption of infinite wall valid (cf. §3.2). This condition, coupled with the hypothesis of constant thermal properties (§4.4.2) makes it possible to use the classical thin film sensor. The thin film sensor has therefore been used by ALTA to calculate the surface heat flux starting from thermocouple measurements. These results will be compared with those from the new heat flux sensor in §4.11.

Apart from noisy temperature measurements, the other experimental problem pointed up in §4.7 is related with the not constancy of the stagnation temperature T_0 . For the reasons described in §4.7 this problem could make the new heat flux sensor not usable. This has been

solved implementing the variability of T_0 in the heat flux sensor, so that the known curve $T_0(t)$ is used in the boundary conditions (3.13) as a known input parameter.

With reference to the equation (3.12)-(3.13) and to the parameters (3.16) on which it depends, the data reduction program will need the following data in input:

- T_r is the ambient temperature, which is known both from temperature measurements at the test facility and from thermographic measurements on the surface of the model before the beginning of the first test of the day.
- T_{wi} is the temperature at the beginning of the test, which is supposed to be constant through the thickness of the model. Since each day of testing has been composed by several runs, and since the quasi-void conditions inside the wind tunnel imply negligible radiative heat flux, the temperature T_{wi} changes at the beginning of each test, and it has been calculated by averaging several thermographic measurements on the surface of the model before the beginning of each run. These assumptions for T_{wi} are perfectly valid as long as the proper relaxation time is waited between one test and another.
- T_0 , rather than T_{aw} as mentioned above, is given in input as a discrete function of time. Data filtering techniques used at ALTA cause T_0 to be not known at the beginning of the test, typically for about 20 *ms*, although the exact value changes from test to test. The insertion time t_{imm} (3.15bis) has been set accordingly and for $0 < t < t_{imm}$ T_0 has been considered to vary linearly from T_{amb} to the known value for $t = t_{imm}$.

Finally, the thickness L of the model has been set to the model actual thickness of 1.5 *mm*, although this parameter is not important given the semi-infinite wall behaviour of the model.

With such setup the temperature rises calculated in the previous paragraph are given in input point by point to the optimization program core of the heat flux sensor and surface heat fluxes are calculated and given in output on each point of the mesh.

4.10 Results

The results for temperature and heat flux measurements are shown in this paragraph while a confrontation with the thin film sensor and with the data from the Calspan case will be done in the following paragraphs.

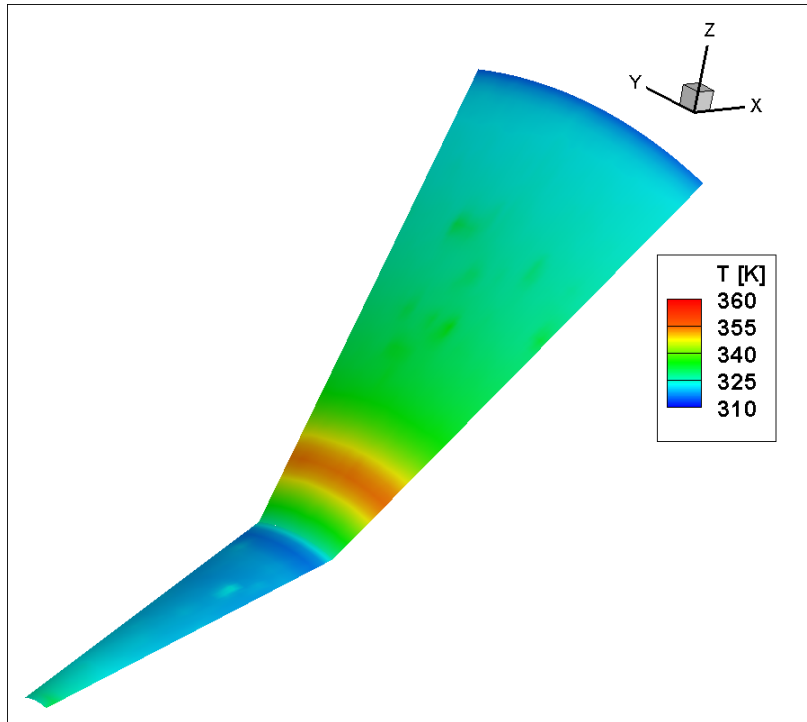
4.10.1 Temperature maps

The maps shown in this paragraph will illustrate the temperature distribution calculated with the method described in §4.8. All the figures show only the results from run 13-3_#3, but they are qualitatively representative of the whole test campaign.

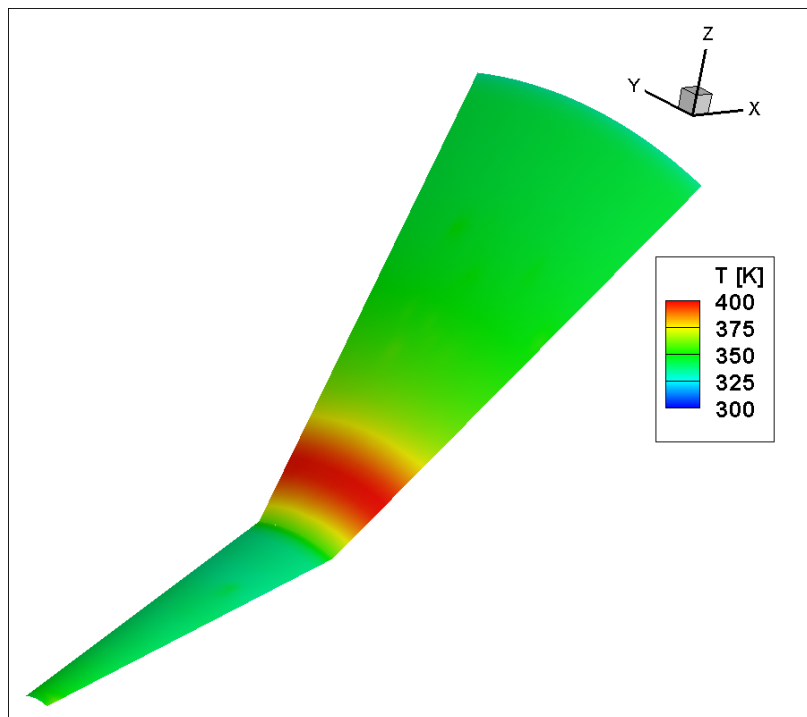
Figure 4.16 shows the 3D surface temperature map at two different instants: at the beginning of the test and in the end of the blowdown shot, when maximum heating is reached. The separation zone at the end of the first cone is visible, being colder, and the reattachment zone is visible too, being of significantly higher temperature.

Since the flow is axial-symmetric, a spanwise average of the measured temperatures can be performed to get a 1-dimensional view of temperature variations along the axis. This view, which can give a better understanding of the phenomena involved is shown in figure 4.17. Separation and reattachment can still be seen well, although not at all instants probably due to noise. At the end of the test the recirculation might not clearly visible also for tangential heat conduction effects.

Finally figure 4.18 shows a frame in which a sparkle hits the model. It can be seen how the temperature measurement error involves a quite wide area of the model, making space filtering extremely difficult

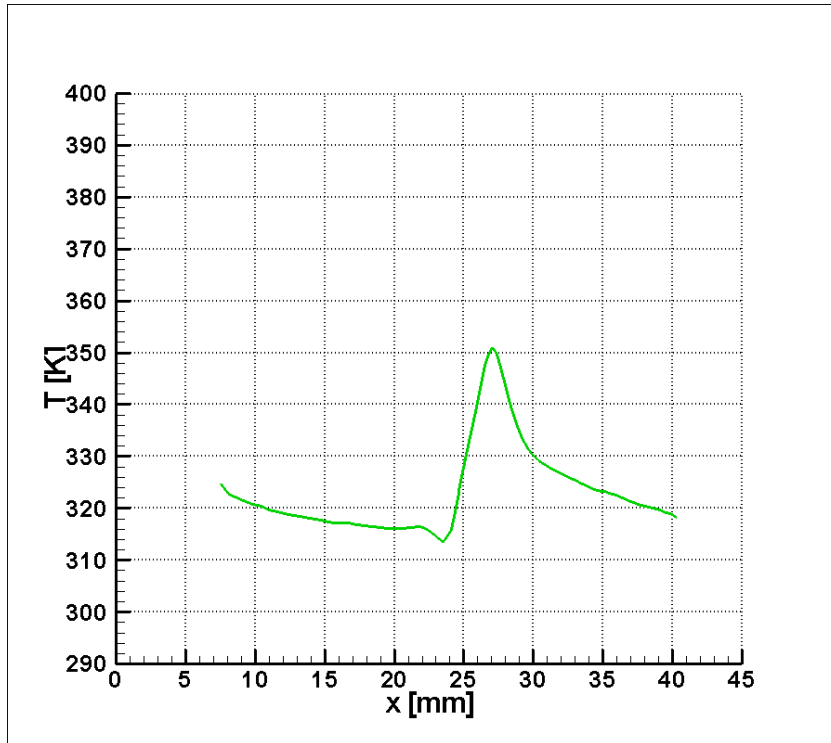


(a)

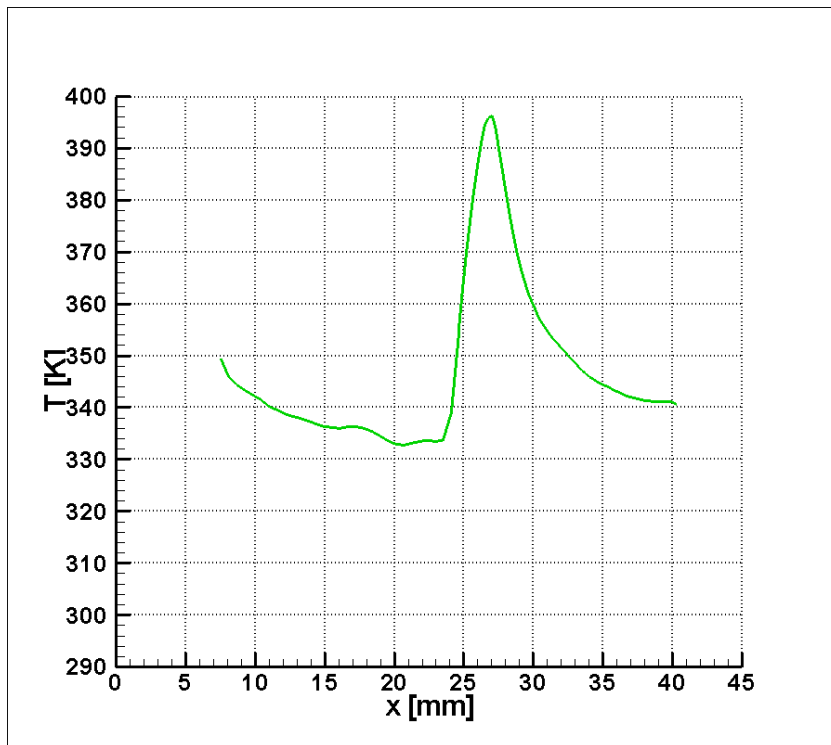


(b)

Figure 4.16: Run 13-3_#3, 3D surface temperature maps. (a) $t = 0.013$ s, (b) $t = 0.166$ s. Reattachment can be clearly seen in both figures, recirculation is slightly visible in (a). *NOTE*: the temperature scales are different in the two figures, to view the temperature distribution better



(a)



(b)

Figure 4.17: Run 13-3_#3, 1D temperature diagrams. (a) $t = 0.013$ s, (b) $t = 0.166$ s; these are the same instants of figure (4.16). Reattachment is evident, recirculation can only be viewed in (a).

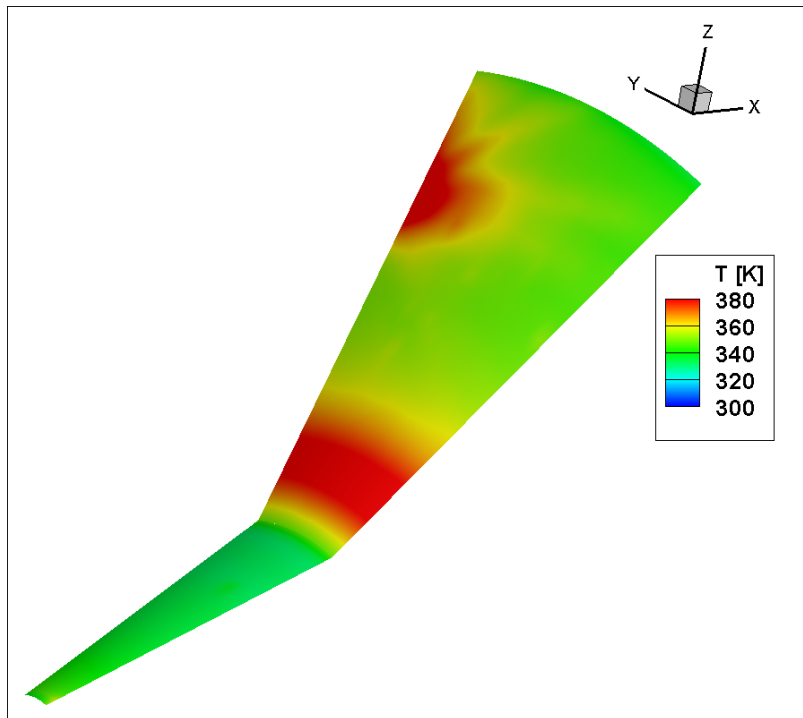


Figure 4.18: Temperature map in presence of a sparkle

4.10.2 Heat flux maps

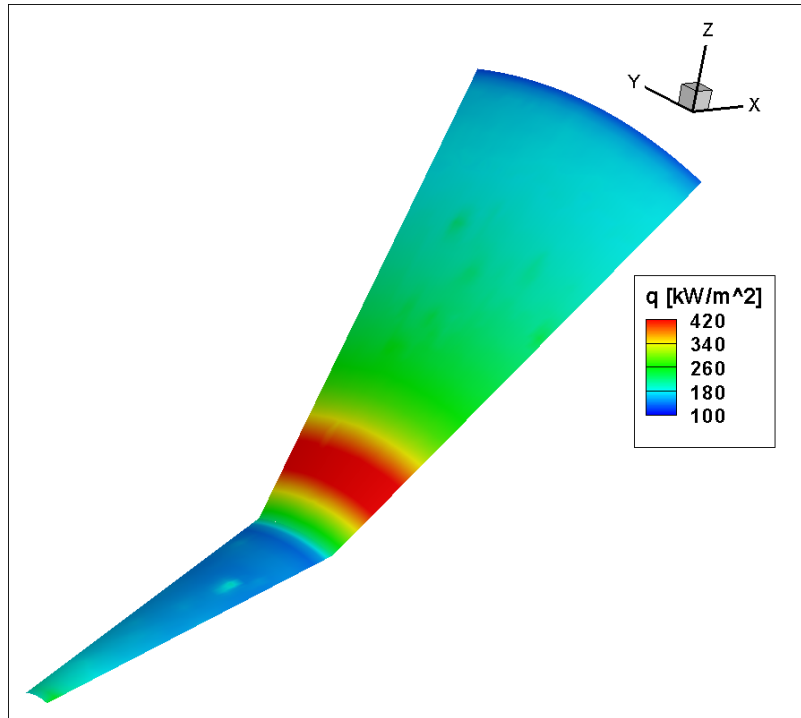
In this paragraph the estimated heat fluxes are shown, for the same run illustrated in §4.10.1 (run 13-3_#3).

Figure 4.19 shows the 3D surface heat flux map at the beginning and at the end of the test, in the same instant where temperature maps of figures 4.16 and 4.17 were shown. It can be seen that the total heat flux stays basically unchanged for the whole duration of the test. As in the case of temperature measurements, the peak of heat flux at reattachment can be clearly seen, but the recirculation zone is not very evident. This problem is verified for some runs only, as it will be seen in §4.11.

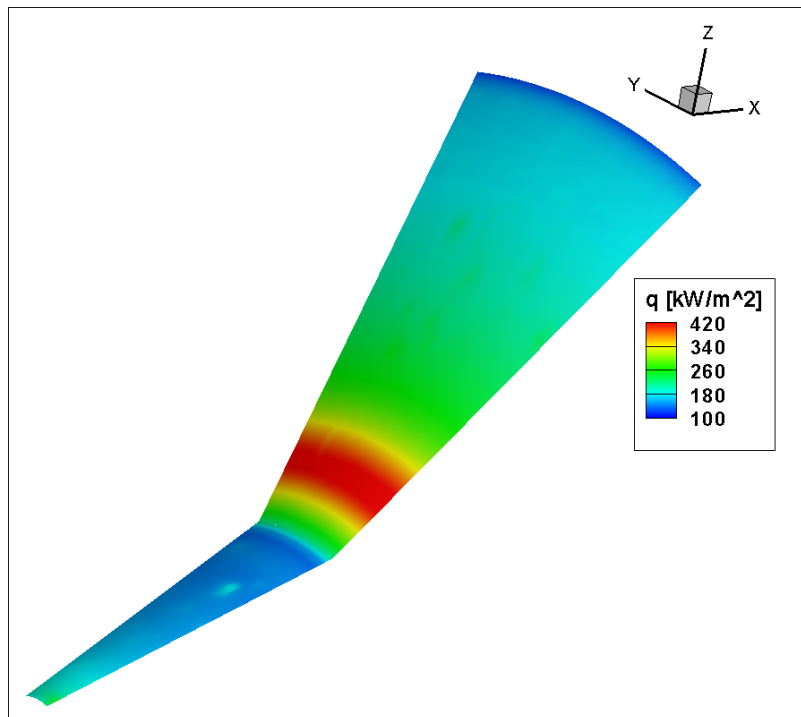
Figure 4.20 shows the radiative heat flux at the end of the test, when it reaches its maximum. It can be seen that it is always negligible.

Figure 4.21, finally shows the map of the correlation factor between experimental and numerically generated temperatures. It can be seen that in the correlation is good everywhere but in the recirculation.

One-dimensional heat flux diagrams will be shown in §4.12 and in §4.11 in adimensional form, where they will be analyzed in detail.



(a)



(b)

Figure 4.19: Run 13-3_#3: heat flux maps. (a) $t = 0.013$ s, (b) $t = 0.166$ s; these are the same instants as figure 4.16. It can be seen that the flux stay almost unchanged for the whole duration of the test

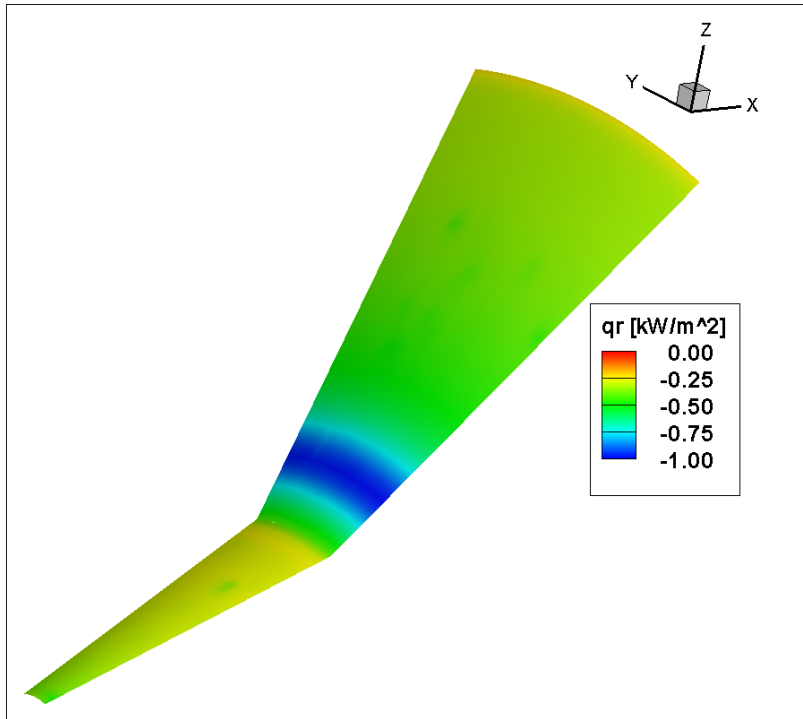


Figure 4.20: Run 13-3_#3: maximum radiative part of the heat flux. A comparison with figure 4.19 shows that it is always negligible

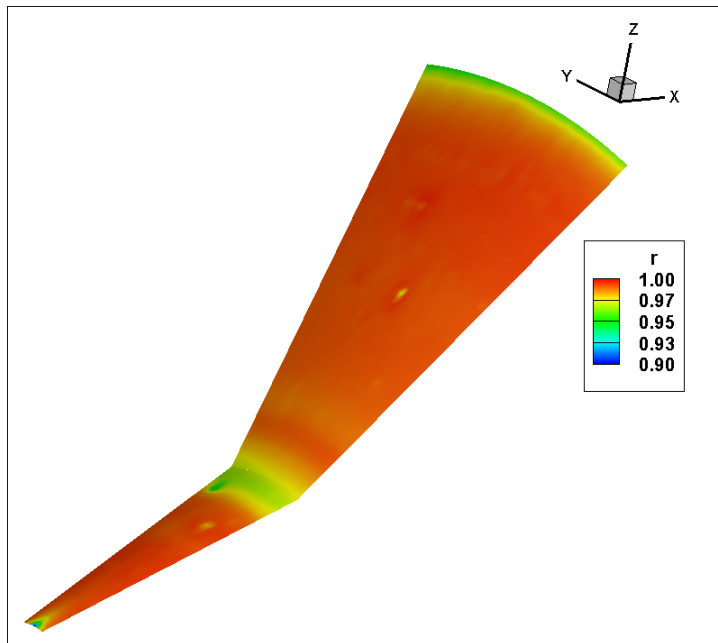


Figure 4.21: Correlation. It is good everywhere except in the recirculation, where heat flux is minimum

4.10.3 Time history temperature diagrams

In this paragraph a confrontation is shown between calculated and estimated temperature for 1D calculations in four runs. The figures in the next pages show 1D temperature rises are in the points shown in figure 4.22: **A** is close to the tip, **B** in the middle of the recirculation zone, **C** at reattachment and **D** further downstream. Along with the temperature rises, in each figure the evolution of stagnation pressure is shown; this is an important piece of information because, as explained, the stagnation pressure determines the shape of the temperature rise.

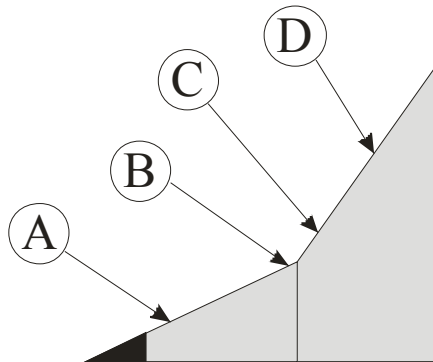
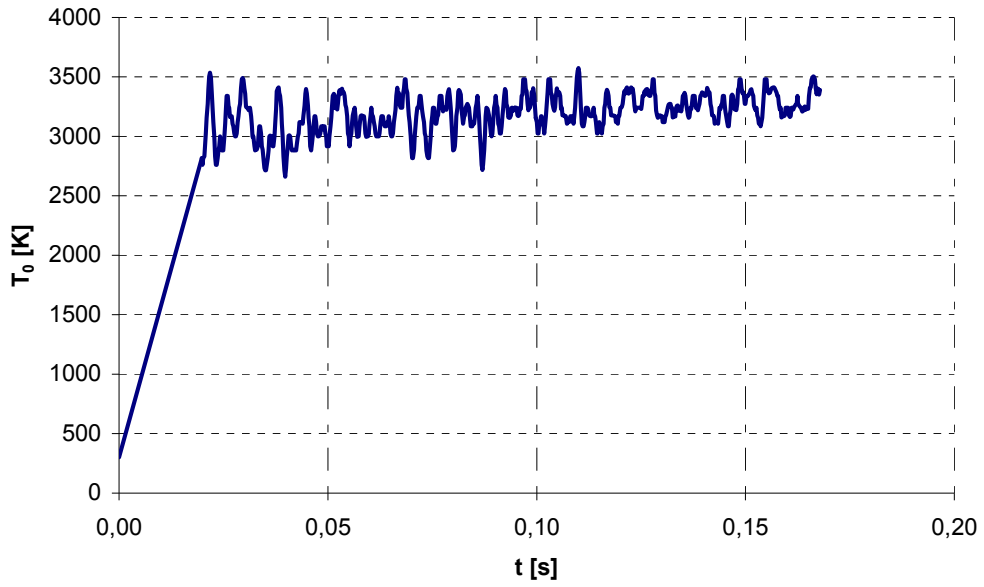


Figure 4.22: Points in which the temperature transients shown in figures 4.25-4.28 are calculated. Point **B** is in the recirculation zone, point **C** at reattachment

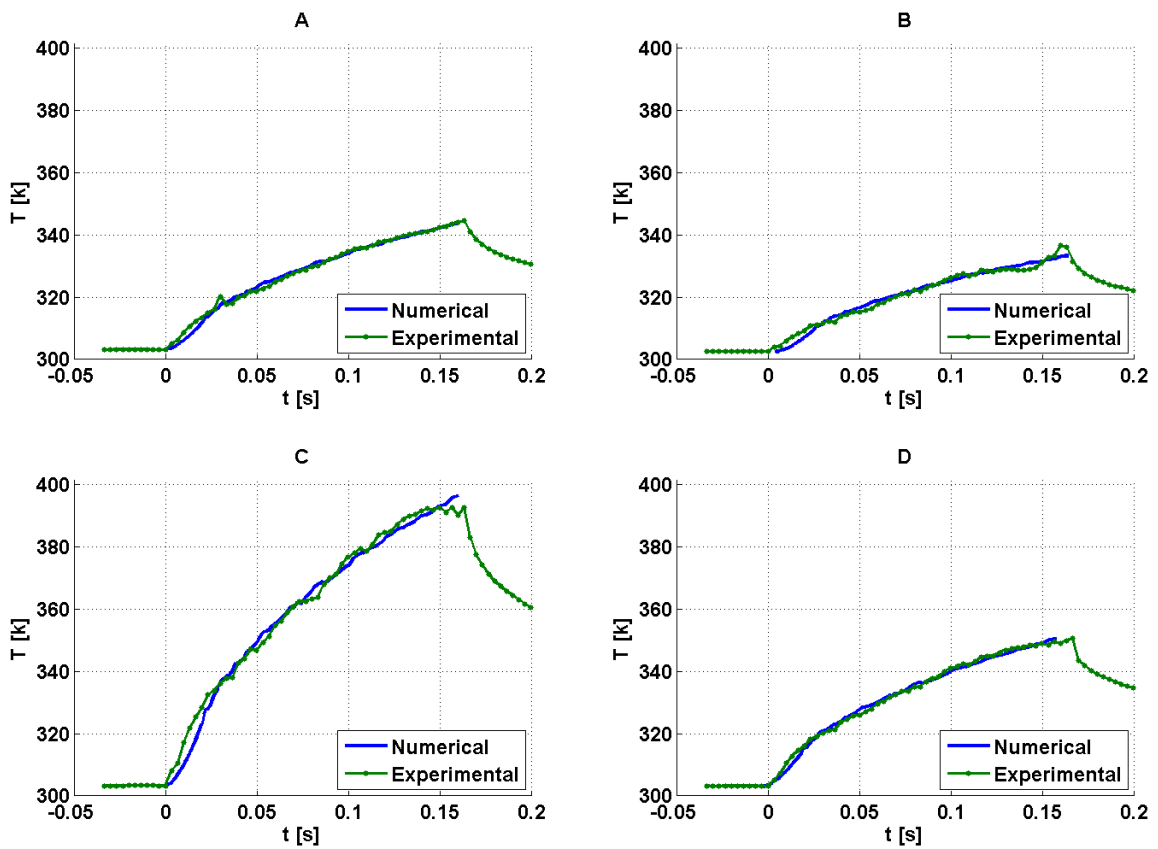
The four runs have been chosen as characteristic of the whole test campaign. In particular:

- Figure 4.23 shows a typically good run, with almost constant stagnation pressure and proper temperature reconstruction, despite the presence of sparkle which can be noticed, for example, in figure 4.24(b)-A.
- Figure 4.24 shows a run with double arc ignition. Despite this problem, the numerical reconstruction has still been good, with a larger error only at reattachment point.
- Figure 4.25 shows another good optimization. In this case, the arc didn't ignite properly during the first 40 *ms* of the run. This test shows the full benefits of the parameter *delay* (cf. §3.4.2). The insertion time t_{imm} in this run has been set to a value higher than usual (about 42 *ms*) and the optimizable *delay* parameter has translated the numerical temperature rise to get proper fitting for $t > t_{imm}$.
- Finally, figure 4.26 shows a failed optimization. The heat flux estimation hasn't worked for a number tests characterized by extremely high levels of noise and of particularly noisy and/or extremely irregular stagnation temperature evolution. In this particular case, a very bad time evolution of T_0 can be noticed.

In all cases, when not differently noted, t_{imm} has been set to 20 *ms* and the unknown time evolution of the stagnation temperature has been considered linear starting from ambient temperature. This choice causes the non-fitted and anomalous evolution of the temperature rises during the first 20 *ms*.

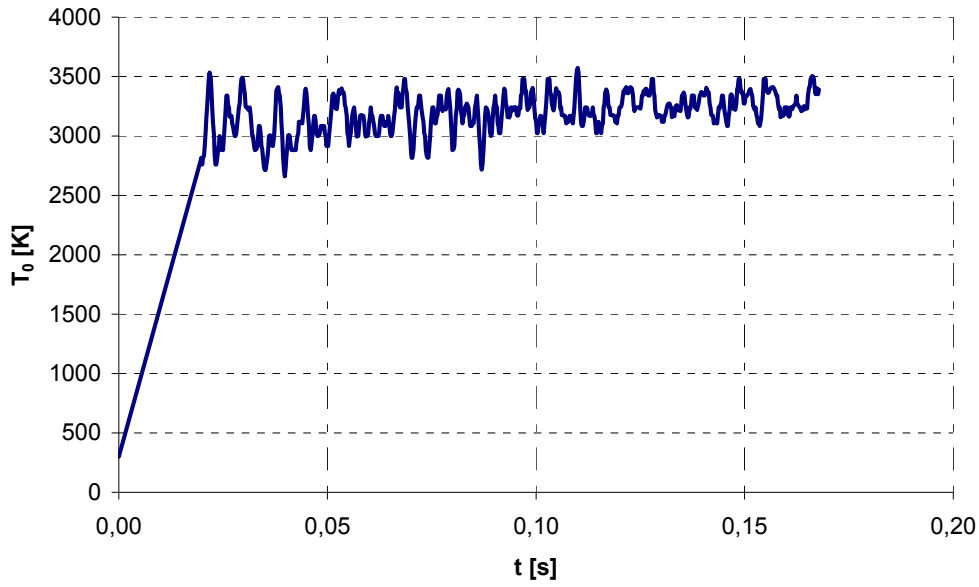


(a)

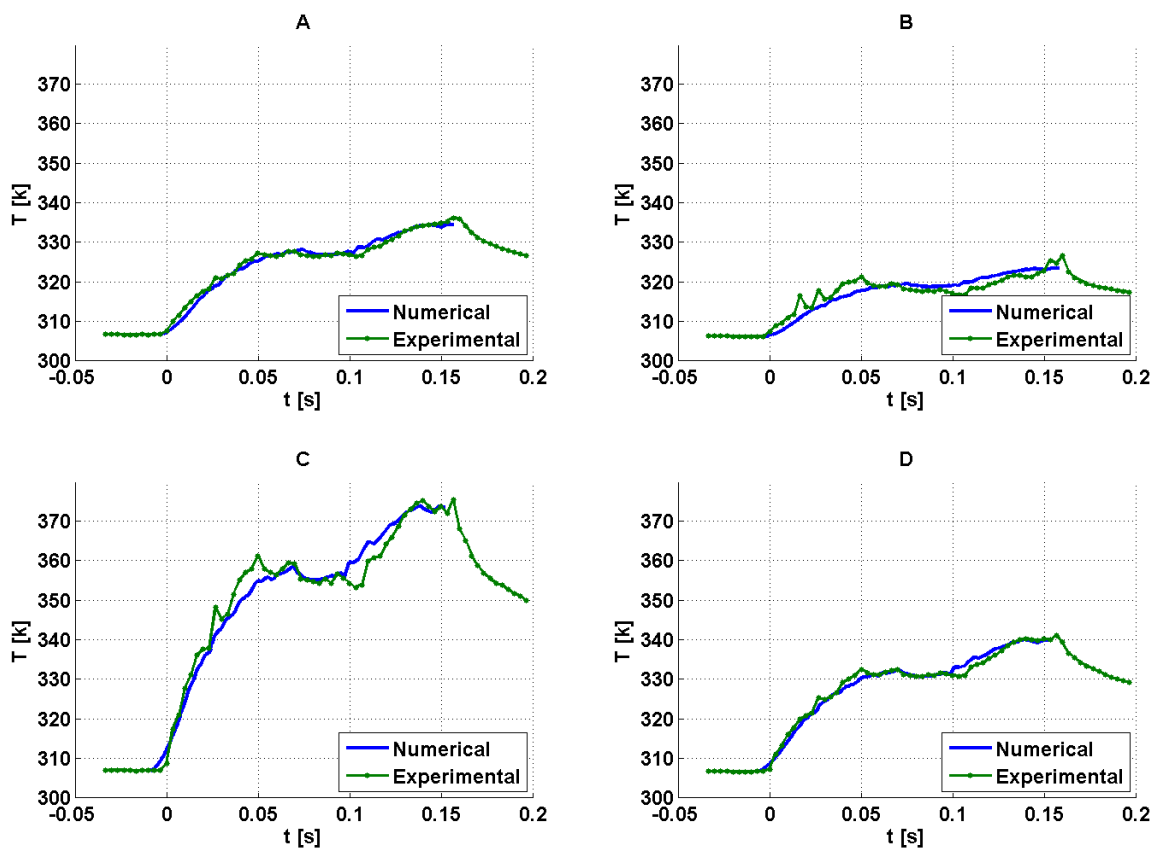


(b)

Figure 4.23: run 13-3_#3. (a) $T_0(t)$; (b) $T(t)$. This is an ideal optimization, with almost constant $T_0(t)$. Notice the presence of sparkles in diagrams A and B

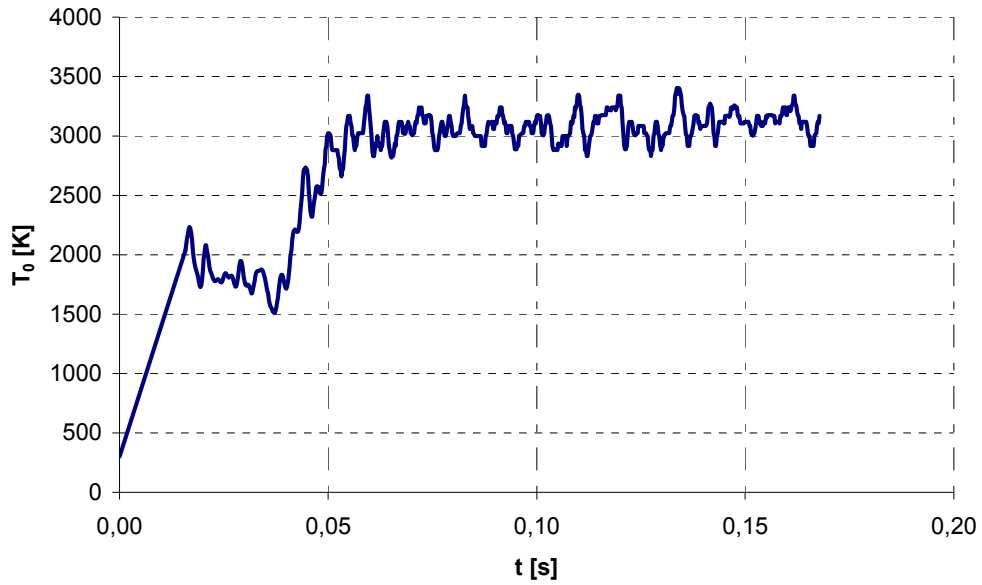


(a)

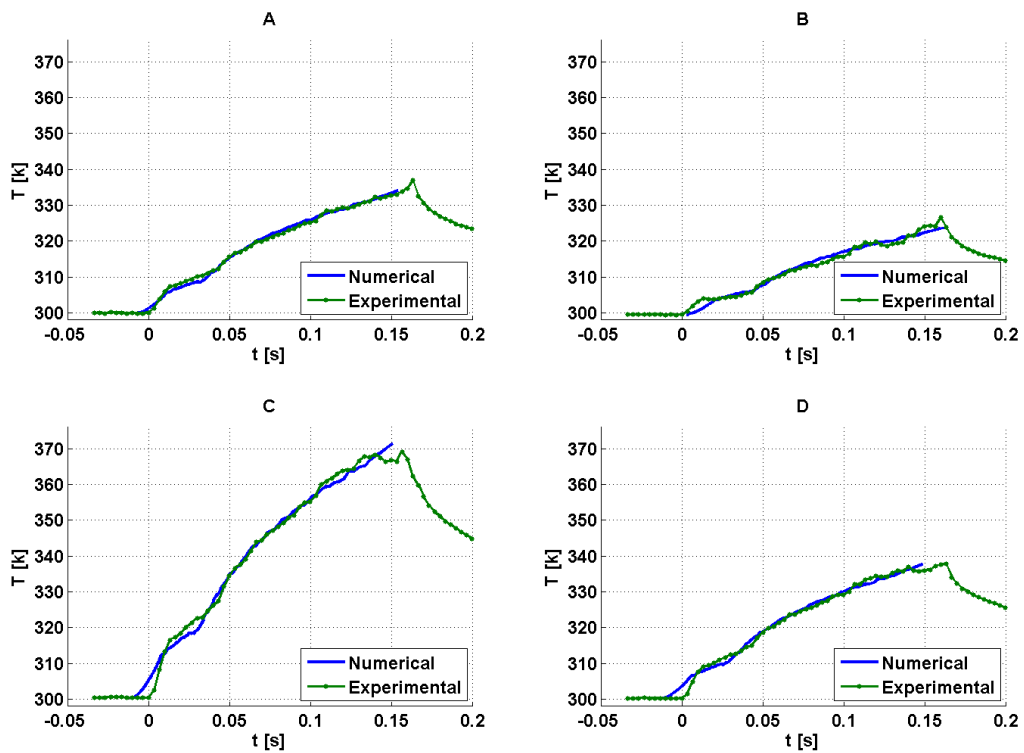


(b)

Figure 4.24: run 13-3_#12. (a) $T_0(t)$; (b) $T(t)$. Run with double ignition of the arc and with good temperature reconstruction

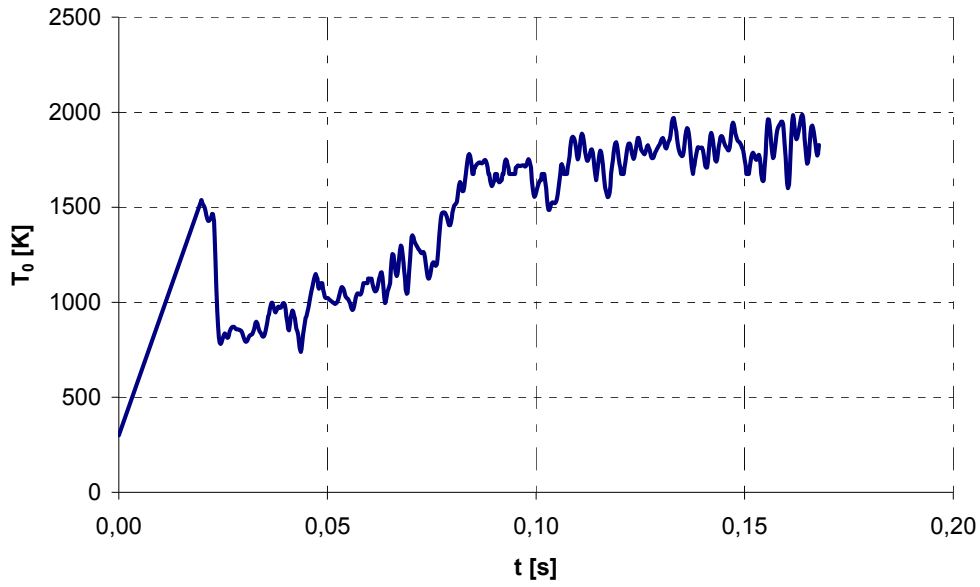


(a)



(b)

Figure 4.25: run 12-3_#1. (a) $T_0(t)$; (b) $T(t)$. In this run the transient of $T_0(t)$ was not acceptable during the first 40 ms. Notice how the *delay* parameter has allowed proper fitting anyhow



(a)

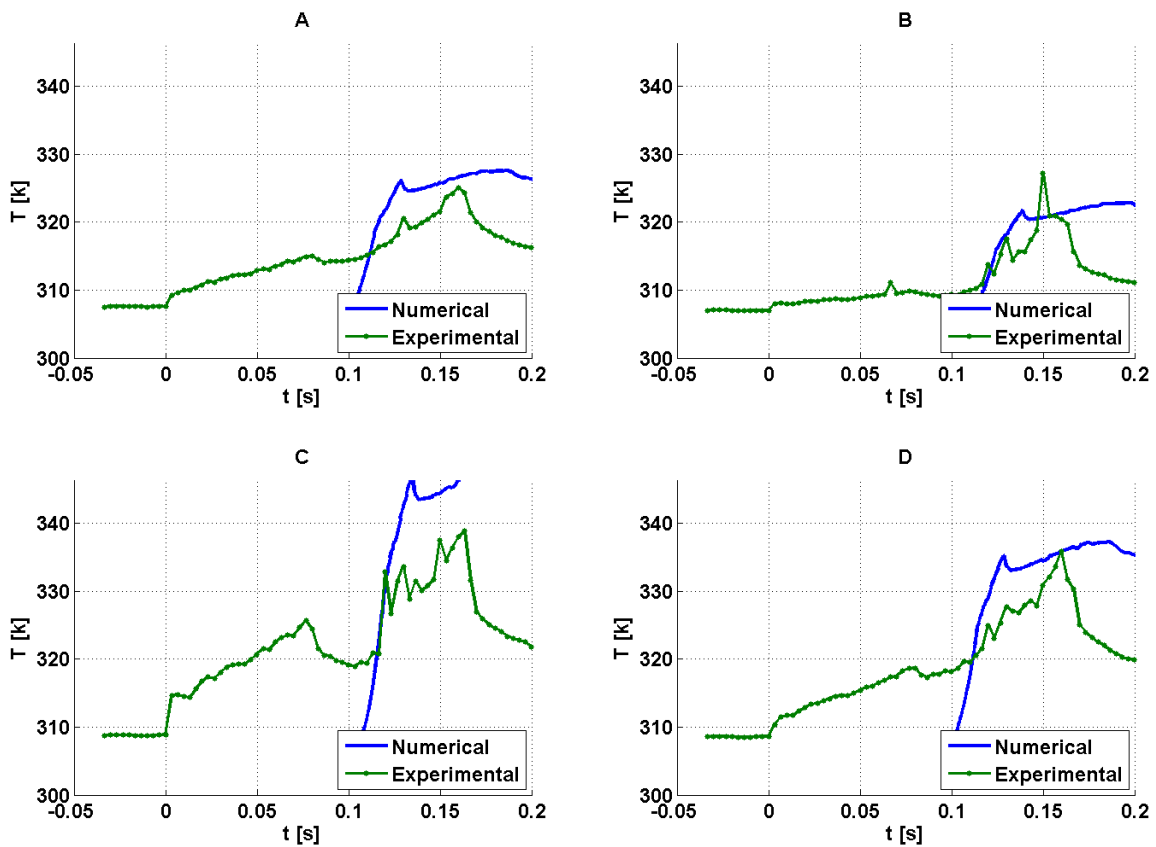


Figure 4.26: run 11-3_#12. (a) $T_0(t)$; (b) $T(t)$. Failed reconstruction due to bad arc ignition

4.11 Comparison with literature

The results obtained in this work will be compared with those of Holden & Wadhams (2001), which will be referred to as Calspan results in this paragraph. In order to do this comparison, in this paragraph the surface heat flux q_w will be presented in terms of the modified Stanton number c_H (cf. Druguet et al., 2005):

$$c_H = \frac{q_w}{\rho_\infty u_\infty^3} \quad (4.6)$$

The tests of the TC-1a have been performed at Reynolds number different from the Calspan ones, and variations in Reynolds number are present even within different runs of TC-1a. In order to compare tests performed at different Reynolds, the values of c_H have been scaled according to the following relation, valid for laminar flows (Di Cristina, 1970; De Luca et al., 1995):

$$c_H = c_{H_p} \frac{\sqrt{Re_p}}{\sqrt{Re^*}} \quad (4.7)$$

where c_{H_p} and Re_p are the values of Stanton and Reynolds in the single runs, and Re^* is a reference Reynolds number; the Reynolds number of run 13-3_#3 has been chosen:

$$Re^* = 4.6 \times 10^4 \quad (4.8)$$

The Reynolds numbers used in (4.7)-(4.8) are referred to unity length: $Re_p = \frac{\rho_p u_p}{\mu_p}$.

It must finally be remembered that the linear dimensions of the TC-1a cone are smaller than those of the Calspan cone, so to compare the two cases the axial coordinate has been normalized to the total length of the TC-1a cone. The comparison is presented in figures 4.27 and 4.28. It should be noted that the much higher Reynolds number in the Calspan case implies a larger recirculation zone. For this reasons, values of c_H can be compared only in the region of the cone before separation.

It is seen that the results can be subdivided in two families: family 1, where estimated heat flux is in very good accordance with Calspan data, and family 2 be where they are lower. Trying to explain the reasons for this behaviour is outside the scope of this work, but it is noted that these results are in accordance with the heat flux calculation performed by Alta; it is supposed that the different results are characterized by two different and unpredictable behaviours of the arc (Caredda et al., 2008).

It can be also seen from figure 4.27 that for the runs belonging to family 1 the recirculation zone is not visible in the estimated heat flux. Several reasons may be responsible for this:

- It can be a direct consequence of the anomalous behaviour of the arc causing noisier data, which have already been noticed in temperature measurements (see §4.10.1 and figure 4.17).
- In the runs belonging to this family, a smaller recirculation zone might be generated; this smaller is at the boundaries of the special resolution of the thermograph whose measurements might therefore be interpolated with measurements from nearby points, outside the recirculation zone, hence making it not visible.
- The recirculation zone is the one with the lowest heat flux where, has extensively seen in chapter 3 and highlighted in figure 4.21, the accuracy of the heat flux sensor is lower.

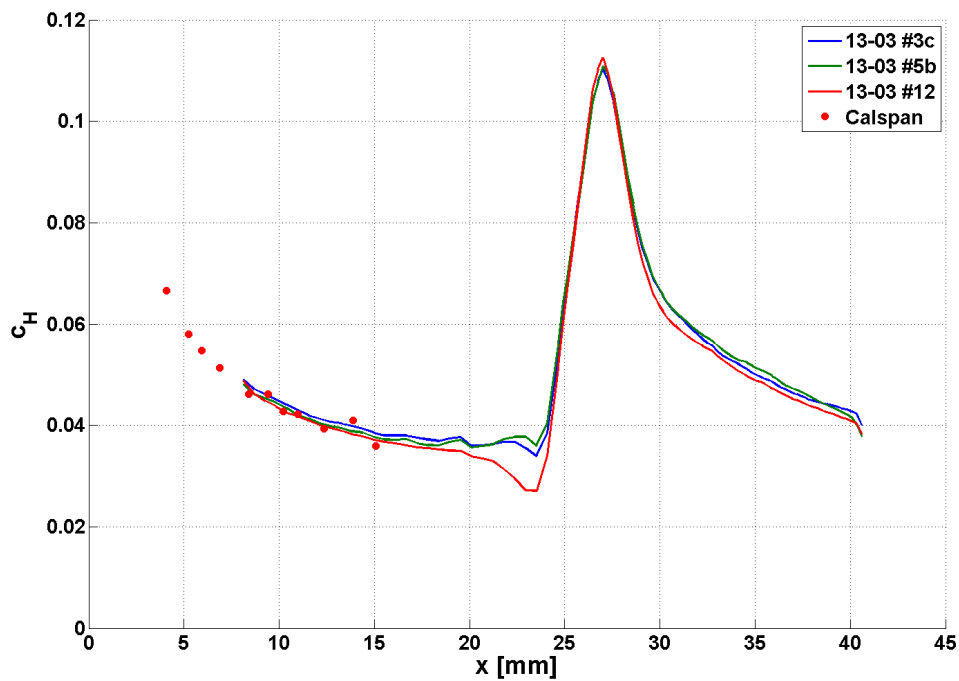


Figure 4.27: Stanton number along the axis of the model – family 1

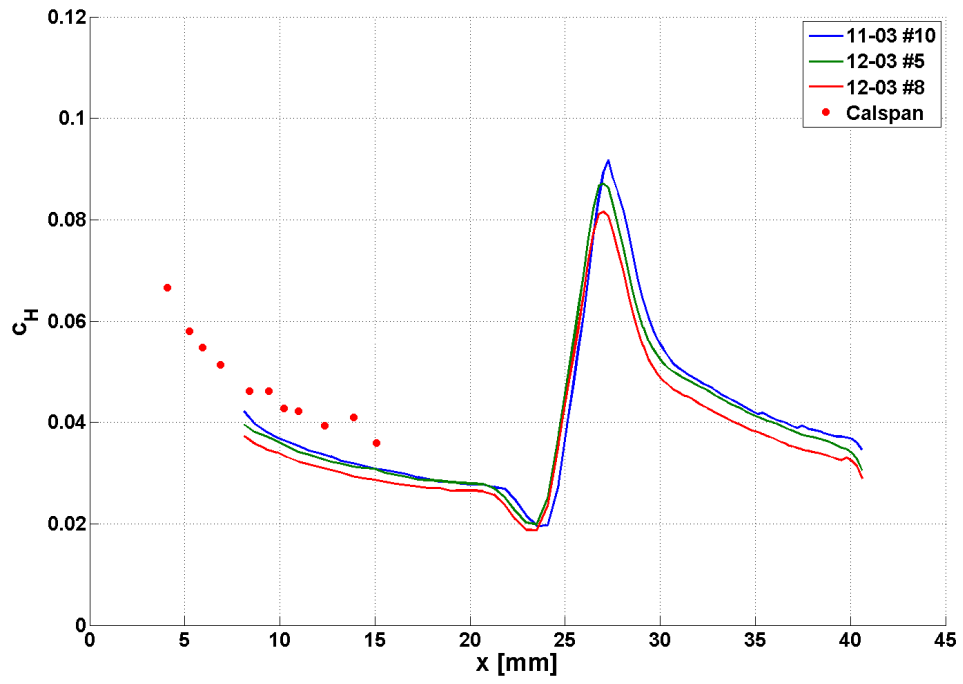


Figure 4.28: Stanton number along the axis of the model – family 2

4.12 Comparison with thin film

Heat fluxes estimated by the new heat flux sensor are here compared with the heat flux calculated by Alta with classic methods for two runs and shown in figures 4.29 and 4.30. It can be seen how that there is a good accordance between the two methods. As regarding the accuracy, the new heat flux sensor appears to be very accurate (see also §3.6) whereas classic thin film calculations present a higher degree of uncertainty.

The higher uncertainty of the classical thin film sensor is due to the problems it has in dealing with noisy data, as outlined in §3.2, §3.3. This particular test campaign has been characterized by high noise levels and by the time variation of the stagnation temperature; this flow characteristics favour the stability and accuracy of the whole domain estimations based on a physically realistic model adopted by the new heat flux sensor, against the smoothing techniques adopted by classical methods and based either on frequency analysis or on pre-imposed time variation of the temperature transient, which in test campaigns like this is unpredictable *a priori*.

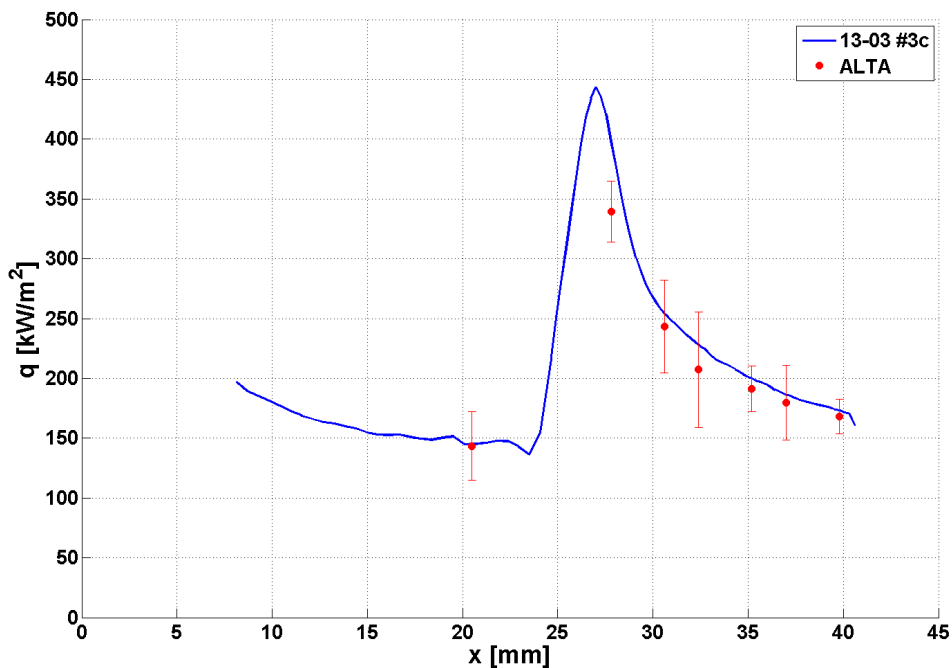


Figure 4.29: Run 13-3_#3; comparison between thin film and new heat flux sensor

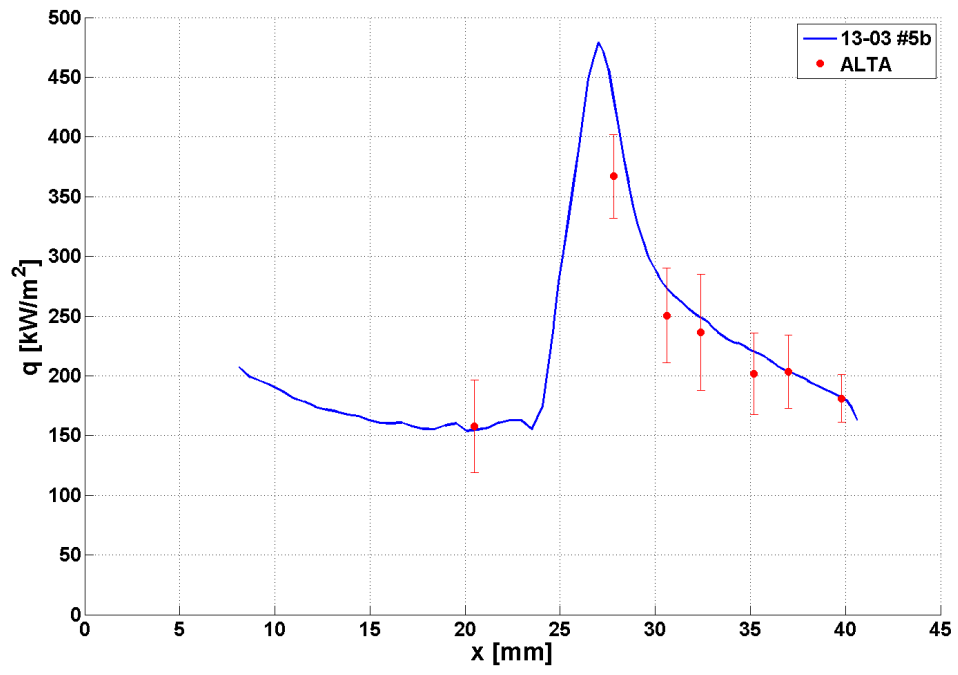


Figure 4.30: Run 13-3_#5; comparison between thin film and new heat flux sensor

4.13 Conclusions

The heat flux sensor proposed in chapter 3 has been used to calculate heat fluxes in a typical test case, and the test conditions have involved the use of the 1-parameter heat flux identification. The CAST TC1a has proved to be an ideal test ground for the experimental validation of the new heat flux sensor. In fact the selection of a classical test case and the appropriate choice of materials made possible and reliable the use of the thin film sensor.

Unexpected experimental problems, in particular the high noise in the test chamber and the non-constancy of the stagnation temperature have been encountered, and this latter problem has caused the need for an update of the heat flux sensor to include the time variability of stagnation temperature.

Despite the experimental problems, the new heat flux sensor has proved to be extremely stable and accurate, and comparisons with results from the thin film sensor have shown that even when the classical thin film is fully applicable, the new sensor has been capable to provide greater accuracy. Good agreement with previous experiments has also been found.

It is worthwhile to remind that smoothing and filtering techniques required for the use of classical thin film sensors rely either on known time dependence of the temperature transient or on filtering in the frequency domain. In both cases the noise reduction techniques are uncoupled from the physical reality of the problem, and cannot take into account unexpected temperature evolution as those seen, for example, when the stagnation temperature is not constant.

The new heat flux sensor, making use of a whole domain estimation based on a simple physical modelling of the flow and not only on its effect on the model, makes use of a "implicit" smoothing technique, and it proved to be extremely effective and not requiring any further filtering, neither of the temperature data, nor of the estimated heat flux.

CHAPTER 5: EXPERIMENTAL ANALYSIS – CLAE EXPERT

In this chapter a second experimental validation of the heat flux sensor is illustrated. The layout of the chapter will therefore be quite similar to the one of chapter 4 although, to avoid unnecessary repetitions, general descriptions will be reduced to the minimum and greater attention will be dedicated to the peculiarities of this test case. It is therefore advised to look at chapter 4 for more detailed explanations and background information.

5.1 Introduction: The EXPERT Program

This test has been performed within the EXPERT program, funded by the European Space Agency, and the CLAE Italian project. The purpose of this project is to perform a number of experiments and of numerical simulations to simulate the capsule flight conditions with respect to the shock wave boundary layer interaction phenomenon occurring around the 20° open flap. It is infact known that flow separation over the control surfaces of re-entry vehicles is a typical phenomenon caused by shock wave boundary layer interaction which can deteriorate the efficiency of the control surface and can cause high thermo-mechanical loads in the proximity of flow reattachment. As far as today only few studies have been performed to analyse the phenomenon in high enthalpy conditions.

The model that has been designed reproduces the full-scale EXPERT 20deg flap (see Muylaert et al., 2003), mounted on a holder composed by a flat plate with rounded leading edge (made of copper and actively cooled) and lateral protection rounded edges.

The test studied in this chapter has been the first experimental test within the project.

5.2 Experimental apparatus

5.2.1 The “Scirocco” Plasma Wind Tunnel



Figure 5.1: Aerial view of the Scirocco facility in CIRA (Capua)

The CLAE EXPERT case has been performed in the “Scirocco” Plasma Wind Tunnel (PWT). The PWT is operative since 2001 and, because of its characteristics, it is considered to be the world’s largest facility of this kind. It is a high enthalpy arc-heated facility whose arc can operate at very high powers, up to 70 MW , generating air temperatures up to $10,000\text{ K}$. Another important characteristic of this wind tunnel lies in the large dimension of its test chamber (5 meters of diameter, 7 meters high) which allows to test real-scale models, of dimensions up to 600 mm and weighing up to 150 kg . Five conical nozzle are available to realize different test conditions.



Figure 5.2: The conical nozzle

Along with all the available instrumentation, the PWT is provided also with two thermographs Agema Thermovision 900 which can simultaneously view the test chamber from different angles. Finally, the PWT is ideal for long duration tests, and every day three tests with a duration up to 25 minutes can be performed.

For a full description of the characteristics of the PWT, see De Filippis et al. (2001) and De Filippis et al. (2003).

5.2.2 The thermograph

An Agema Thermovision 900 thermograph has been used for temperature measurements. A list of the main characteristics of the Agema 900 can be found in §1.5. The thermograph has worked at its full frame maximum frequency of acquisition f_s of 15 Hz. It might be noticed that this frequency is much lower than the one used for the acquisitions described in the previous chapter, but the high duration of the test, $t_p \cong 80s$, implies the availability of a large number of temperature measurements, and for such long test durations it is in fact desirable to limit the f_s in order to reduce the computational load.

Given the large distance of the camera from the model (about 4.5 m), the thermograph has not been used with its standard optics but with a tele-lens, involving the reduced field of view of $10^\circ \times 5^\circ$. This choice implies the vision of just half of the model (see figure 5.6) but with better spatial resolution

The model is exposed to the flow at ambient temperature, and is expected to reach temperatures of the order of 1,000 K. The Agema 900 cannot measure such a wide temperature range, but it gives the possibility to select among a limited number of ranges (as is the case with many thermographs, see §1.4). The range 50-600 °C has been chosen because the surface temperature of the model is expected to be within that range most of the time, although this choice implies inaccurate measurements at the beginning of the test. It must be noticed that, given the limited emissivity of the surfaces ($\varepsilon \cong 0.85$) and given the presence of the tele-lens and of the access window on the optical path, the actual range of measurement of the thermograph will be shifted towards higher temperatures.

5.3 Test article design

5.3.1 Geometry

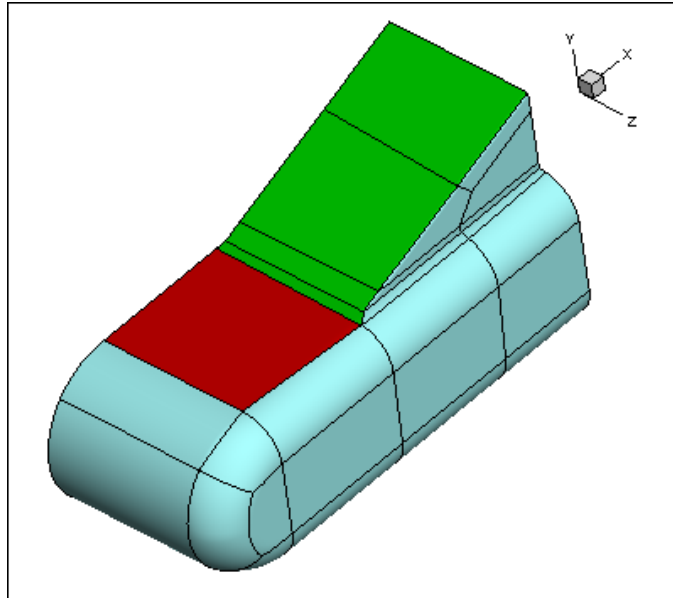


Figure 5.3: CAD drawing of the EXPERT model. The 20° flap and the flat plate in front of it are highlighted

As mentioned in §5.1, the model is a full-scale reproduction of the EXPERT flap. The thermographic measurements of interest are performed on the flat plate and on the ramp.

The flat plate is 400 mm wide and 200 mm long; the flap is as large as the flat plate, i.e. 400 mm, and 300 mm long. The leading edge has the same width of the flat plate, has a radius of 100 mm and is actively cooled; the lateral edges are rounded too in order to avoid localized overheatings.

5.3.2 Materials

Both the flat plate and the flap are relatively thin and slabs of metal mounted on thicker supports of insulating materials. The materials used for the model are the same of the real EXPERT flap.

In particular, the flat plate is made of Haynes H25 and is 2.5 mm thick, is mounted on a support of 22.5 mm of Promasil 1100. The flap is made of a C/SiC, it is 4 mm thick and is mounted on a thick support of SGL Grade R430H, which is a particular amorphous carbon.

All the properties of the materials have been given by the manufacturers, except for SGL Grade R430H which, at the moment of writing, has not been fully characterized yet. This problem has unfortunately implied the impossibility to estimate the heat flux on the flap,

as it will be seen later in this chapter. The properties of the materials are reported in the tables below.

ρ [kg/m ³]	9130	
-----------------------------	------	--

T [K]	c_p [J/kgK]	T [K]	K [W/mK]
293	426	293	8.6
773	506	773	18.7
873	523	873	20.7
973	540	973	22.6
1073	556	1073	24.7
1173	573	1173	26.9
1273	589	1273	29.2

Table 5.1: Manufacturer's characteristics of Haynes H25. Values in red are extrapolated

ρ [kg/m ³]	275	
-----------------------------	-----	--

c_p [J/kgK]	1,050	
---------------	-------	--

T [K]	K [W/mK]
273	0.04
473	0.07
673	0.10
873	0.14
1,073	0.18
1,273	0.18

Table 5.2: Manufacturer's characteristics of Promasil 1100. Values in red are extrapolated

ρ [kg/m ³]	2,100	
-----------------------------	-------	--

T [K]	c_p [J/kgK]	T [K]	K [W/mK]
293	690	293	2.0
473	1,080	473	2.8
673	1,320	673	3.2
873	1,470	873	3.3
1073	1,560	1073	3.4
1273	1,630	1273	3.5
1473	1,700	1473	3.7
1573	1,730	1573	3.8

Table 5.3: Manufacturer's characteristic of C/SiC

Values for SGL Grade R430H are given only at ambient temperature, as:

$$\rho = 1,640 \text{ [kg/m}^3\text{]}, K = 5 \text{ [W/mK]}.$$

The value of c_p is not known, but the value of 707 has been suggested by CIRA.

As regarding emissivity, the values given by manufacturers are $\varepsilon = 0.86$ for the flat plate and $\varepsilon = 0.85$ for the flap, although an experimental calibration has not been done.

From the design of the model and the tables above it is clear that in this test the classical thin film cannot be used: the test model is made of two superimposed materials of different characteristics which furthermore are, in most cases, temperature-dependent and consequently the analytical solution at the basis of the classical thin film cannot be used. A fully numerical method like the one proposed in this work is needed.

5.4 Design of the target

As explained in §4.5, the design of the target to be used with the pinhole model is strictly linked with the test in which it has to be used. The fundamental differences between this test and TC-1a lead to a completely different design for the target used in this case.

This test has been characterized by the great distance between the camera, about 4.5 *m*, imposed by the large test chamber. The constraint to have thermal markers of at least 4 pixels of diameter, along with the characteristics of the camera (see §1.5) and its lens (see §5.3.2), involved the choice of 10 *mm* for the diameter of the markers and final dimension of the target of 60×30 *cm* (for comparison, it is reminded that the target for TC-1a was 7×7 *cm*).

As mentioned in §4.5, for holes to behave as black bodies their depth must be at least 4 times the diameter, which in this case is not doable both because it would require the manufacturing of a very big and heavy target and because of the problems this would create in heating it.

These considerations lead to the choice to make a target of low emissivity thermal markers on a high emissivity slab; this has been achieved using a thin slab of steel painted in black with 10 *mm* diameters holes drilled in it; behind the shallow holes a low-emissivity sheet of steel has been placed. The steel sheet is heated by a printed circuit board; when the circuit board is switched on, both the steel sheet and the slab heat uniformly but, owing to the difference in emissivity between the two, the markers appear on the thermograph as cold spots on a hot background. A drawing of the target is shown in figure 5.4, the negative of its thermal map in figure 5.5

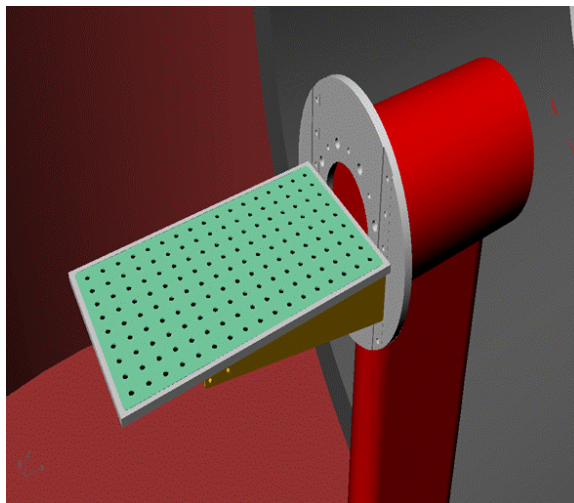


Figure 5.4: CAD drawing of the target mounted on the Model Support System.

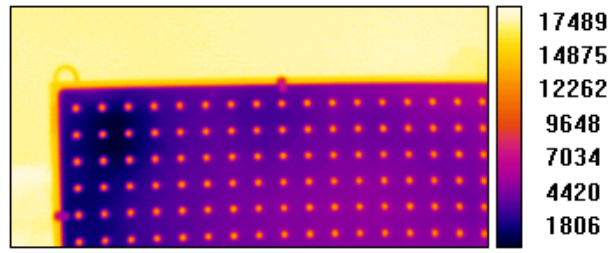


Figure 5.5: IR image of the target. This is actually the negative of the real thermogram, since the markers are seen as cold spots.

5.5 The test

A single experiment was performed, at the conditions reported below in a plasma flow.

Mach	h_0 [MJkg ⁻¹]	T_0 [K]	p_0 [bar]	p_∞ [mbar]	ρ_∞ [kgm ⁻³]	u_∞ [ms ⁻²]	Re_∞
7.3	9.1	6,700	9.6	66.8	6.2×10^{-4}	3,570	8.06×10^4

Table 5.4: Test conditions

The test time has been about $t_p = 80s$, and at time $t_{rot} = 15s$ the model has been rotated from 0° to 5° angle of attack.

5.6 Transient temperature measurement

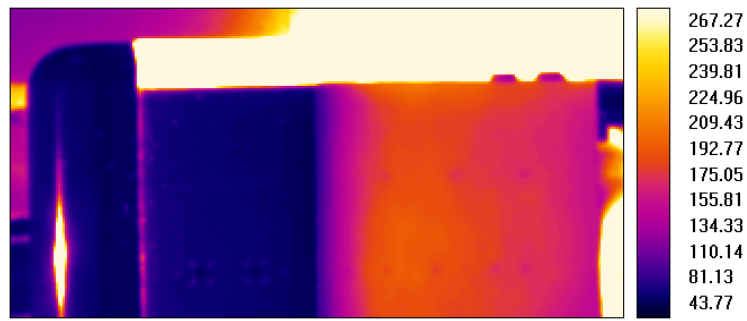
The steps followed to measure the temperature transient on the surface of the model are analogous to the ones already described in §4.8, with just a few differences: a different thermograph has been used, no calibration has been performed (because it is done by CIRA) and no map of emissivity has been made since the angles of view involved are always less than 30° , where no problems of reduced emissivity are encountered (see figure 1.11; although it is been calculated for MACOR[®], the results have general validity). The most significant variation with respect to §4.8 lies in the mesh generation, as described in point (3). The steps followed are briefly described below. Only peculiarities of this test case are highlighted; for a more detailed description of the general concepts involved refer to §4.8

- 1) *Acquisition of a time sequence of IR images.* These images are recorded by the Agema 900 thermograph at a frequency of 15 Hz; the thermograms in this case are 272×136 pixel. In figure 5.6 an IR image of the model is shown.
- 2) *Generation of a mesh on the surface of the model.* A mesh of square elements has been generated, following the same considerations of §4.8. To keep track of the rotation of the model from 0° to 5° two meshes have been generated: the mesh generated on the model at 0° angle of attack has been rotated of 5 degrees around the same axis of rotation of the model. The first mesh has obviously been used for $t < t_{rot}$, the second for $t > t_{rot}$. The result of this procedure is that each point of the mesh represents the same point of the model for the whole duration of the test, excepted during the rotation of the model, which took about a second in the wind tunnel and has obviously been instantaneous for the mesh. Of course during data reduction no rotation of the mesh is seen, but just the effects of the rotation on temperature rise, which becomes steeper.

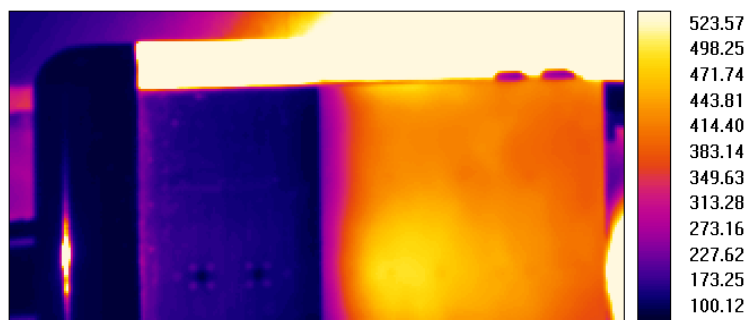
Figure 5.7 shows the mesh built on the model.

- 3) *Tsai calibration.* The target has been mounted model support holder (see figure 5.4), and images from 5 different planes have been taken.
- 4) *Geometrical resection.* the geometrical resection with the Tsai constants has been performed twice: once on the first mesh, and another time for the rotated mesh. Figure 5.8 shows the IR images of the model with the projection of the points of the mesh (figure 5.7) superimposed both before and after rotation.
- 5) *Temperature calculation:* Information gathered in steps (1)-(4) are used to calculate temperatures on each point of the mesh for each time step starting from the IR images

recorded in step (1) and using equation (1.10) with $\tau = 1$. It is reminded again that on each point of the mesh the temperature evolution of the same point of the model is shown, regardless of the rotation.



(a)



(b)

Figure 5.6: Thermogram of the model. (a) Before rotation, (b) After rotation

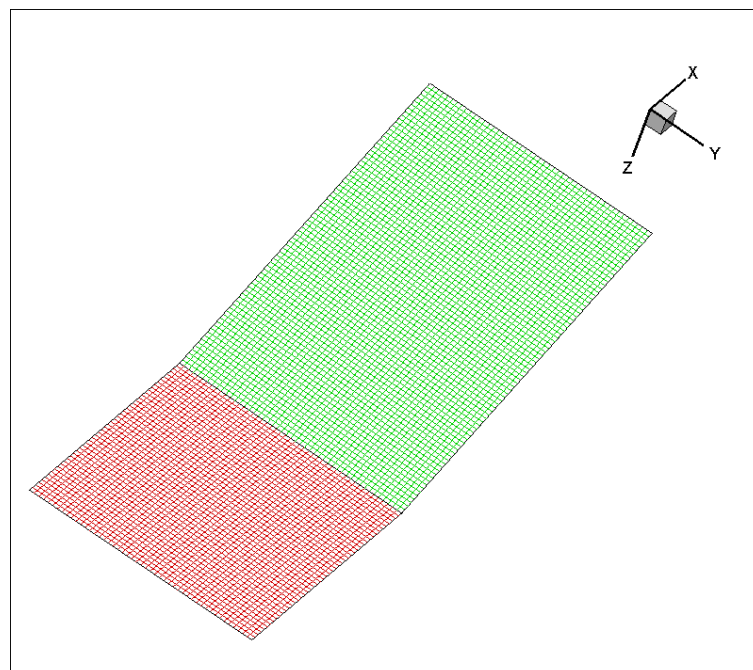
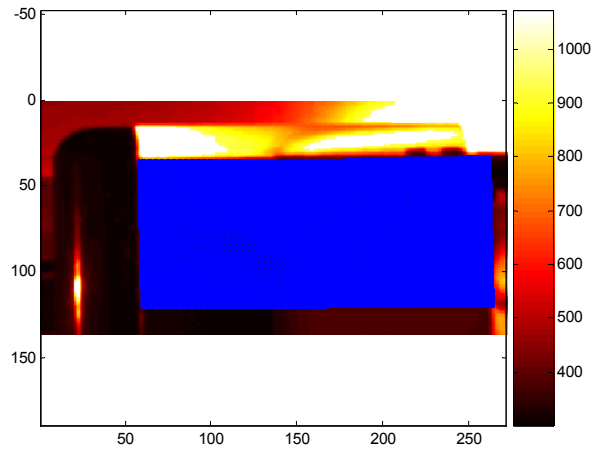
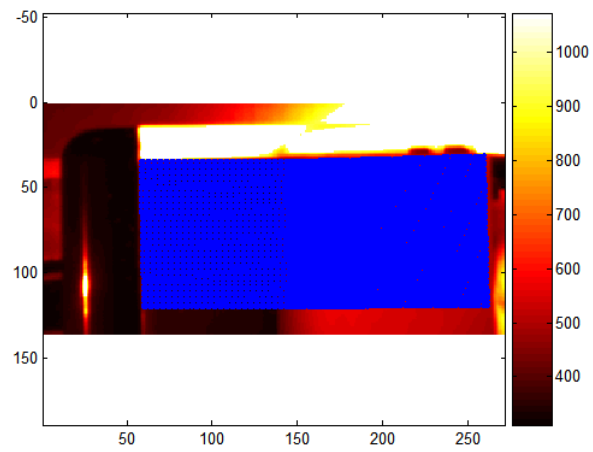


Figure 5.7:: Square mesh on the double model



(a)



(b)

Figure 5.8: The mesh of figure 5.7 projected on the plane of the IR image 5.6.
 (a) Before rotation, (b) After rotation

The temperature measurements performed with the method described in this paragraph will be illustrated in detail in §5.8.1.

5.7 Heat Flux measurement

Heat flux measurement has been somewhat hampered by lack of a complete characterization of the material (in particular, the thermal characteristics of the substrate of the flap are incomplete, and emissivity values are uncertain), but some interesting results have been reached anyway, as it will be shown later.

This particular test case has also been characterized by an interesting feature, namely the rotation of the model after about 15 seconds of test; this rotation involves a modification of the heat flux characteristics. In particular, with reference to equation (3.13), the heat flux coefficient h is not constant for the whole duration of the test. The mathematical model (3.12)-(3.13), on the contrary, considered h to be constant. As a consequence, the heat flux sensor couldn't be used as it is. Two routes could be followed to counter this problem:

- 1) Estimate the heat flux for $t < t_{rot}$ and, once the optimization has succeeded, estimate the heat flux for $t > t_{rot}$ using as initial temperature distribution inside the body the one calculated numerically during the previous optimization;
- 2) Modify the mathematical model in such a way to include the change of h . The heat flux would therefore build the numerical temperature rises estimating h for $t < t_{rot}$ and a different value, \tilde{h} , for $t > t_{rot}$.

The second method has been deemed more reliable and has been implemented.

5.8 Results

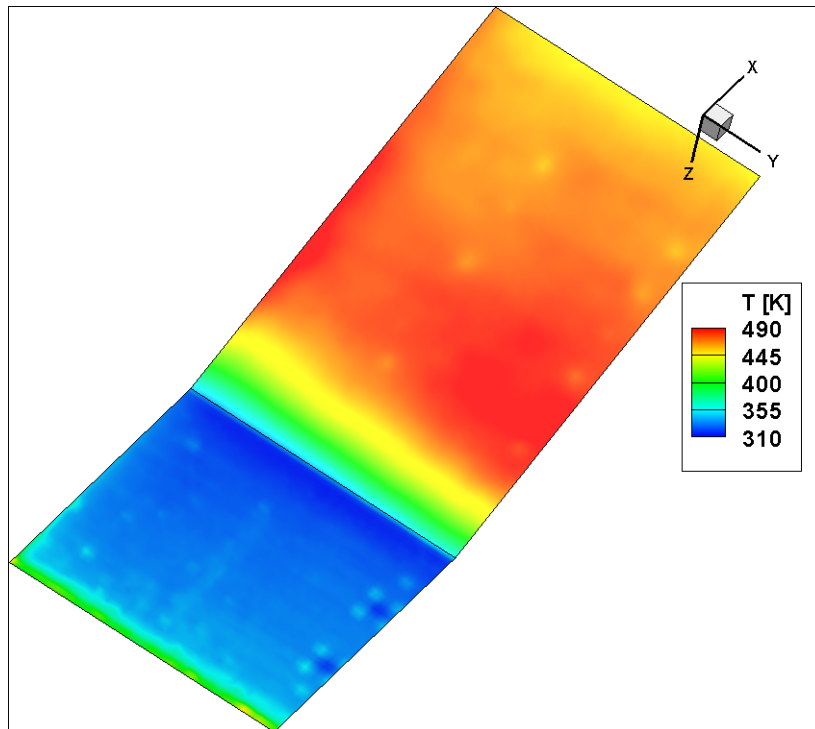
5.8.1 Temperature maps

Figure 5.9 shows the 3D surface temperature map at two different instants: before rotation and near the end of the test. Reattachment is clearly visible, but that there is not a reattachment peak as in the double cone, because the temperature decreases more smoothly after reattachment. At the end of the test the flow some two-dimensional effects are seen.

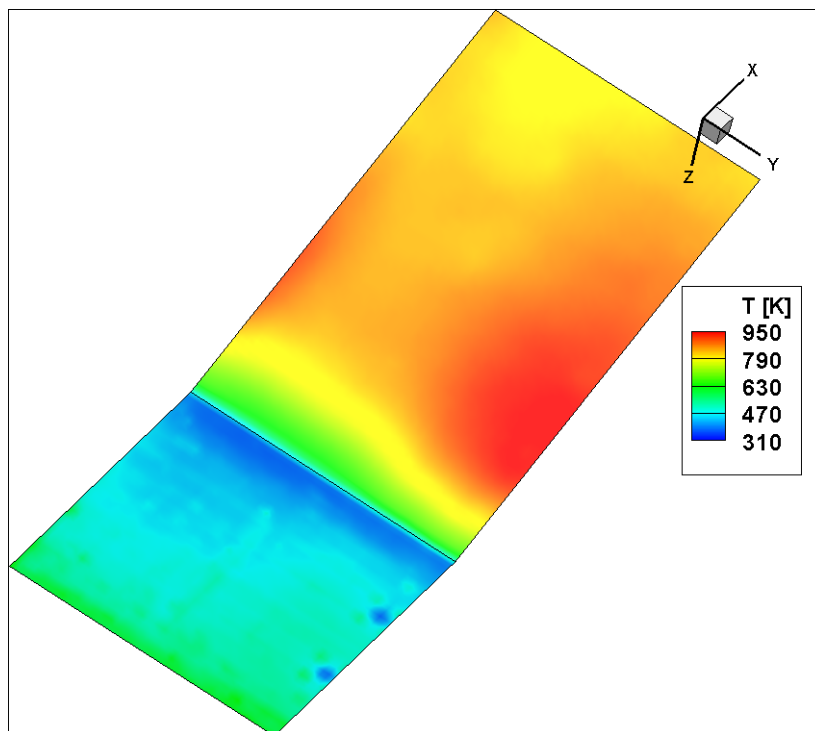
The two cold circles on the flat plate are measurements sensors.

A span-wise average of the measured temperatures is performed to get a one-dimensional view of temperature variations along the model; the average is not done on the whole width of the visible part of the model, to avoid the cold spots. The one-dimensional graph, which can give a better understanding of the phenomena involved, is shown in figure 5.10. Reattachment is always very visible, recirculation becomes evident only for higher times.

It might be worth to remind that no rotation of the mesh is seen in this figures: the mesh rotates with the model and the temperature maps are seen from the point of view of an observer placed on the mesh.

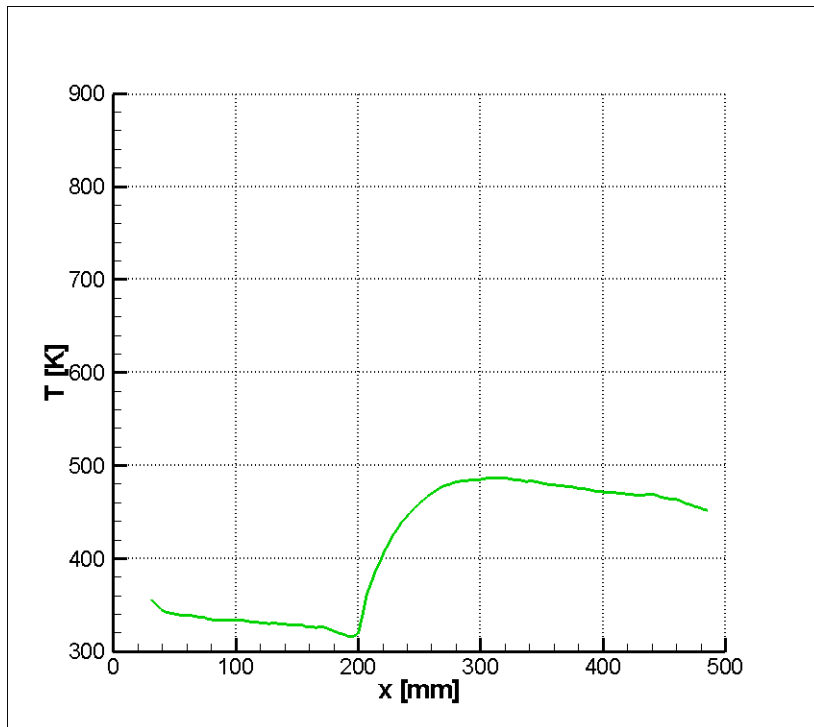


(a)

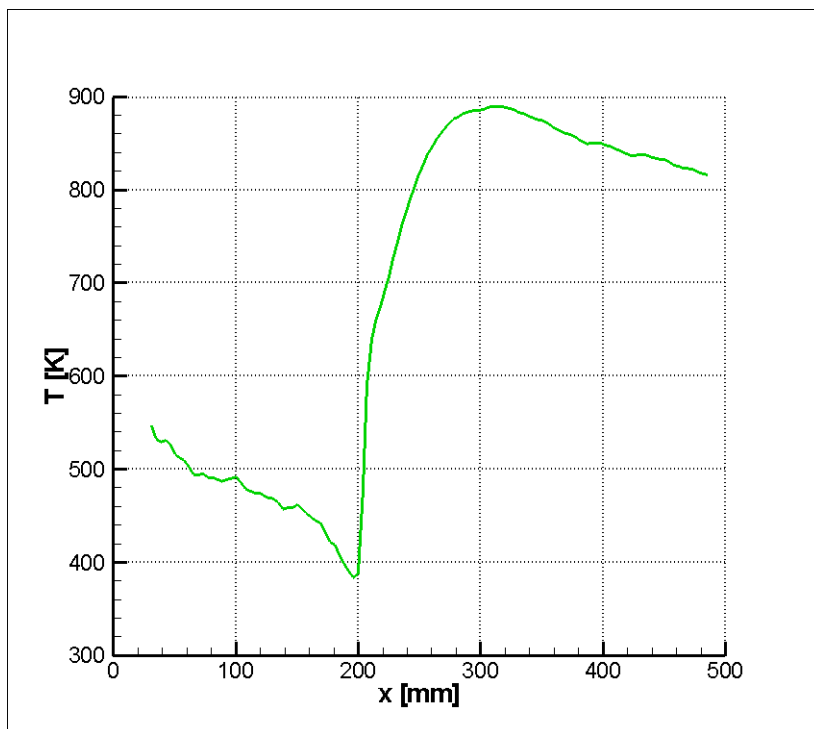


(b)

Figure 5.9: 3D surface temperature maps. (a) $t = 14.93 \text{ s}$, (b) $t = 64.13 \text{ s}$. The recirculation zone can be seen in both figures. *NOTE*: the temperature scales are different in the two figures, to view the temperature distribution better



(a)

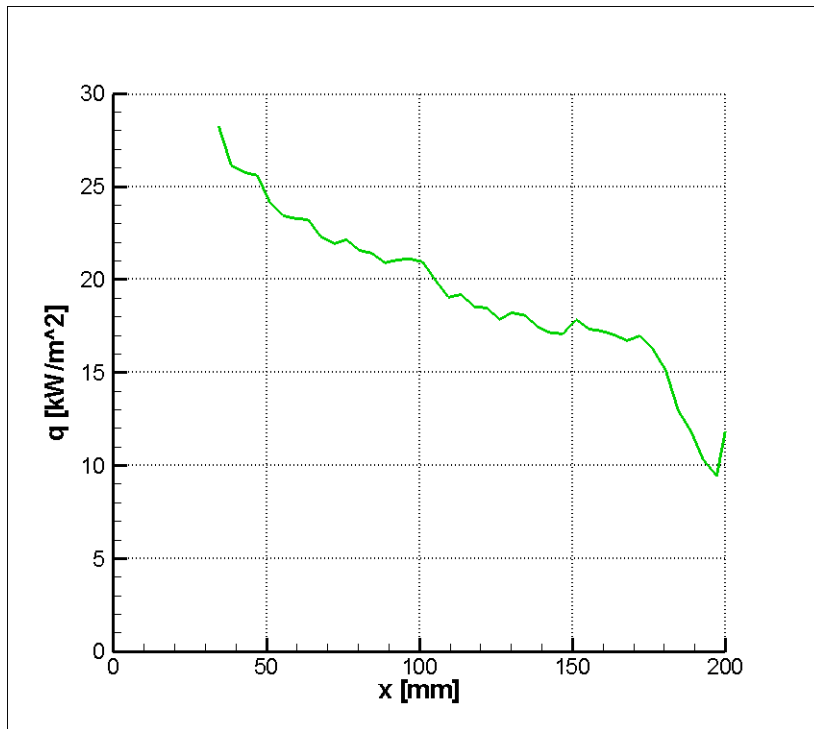


(b)

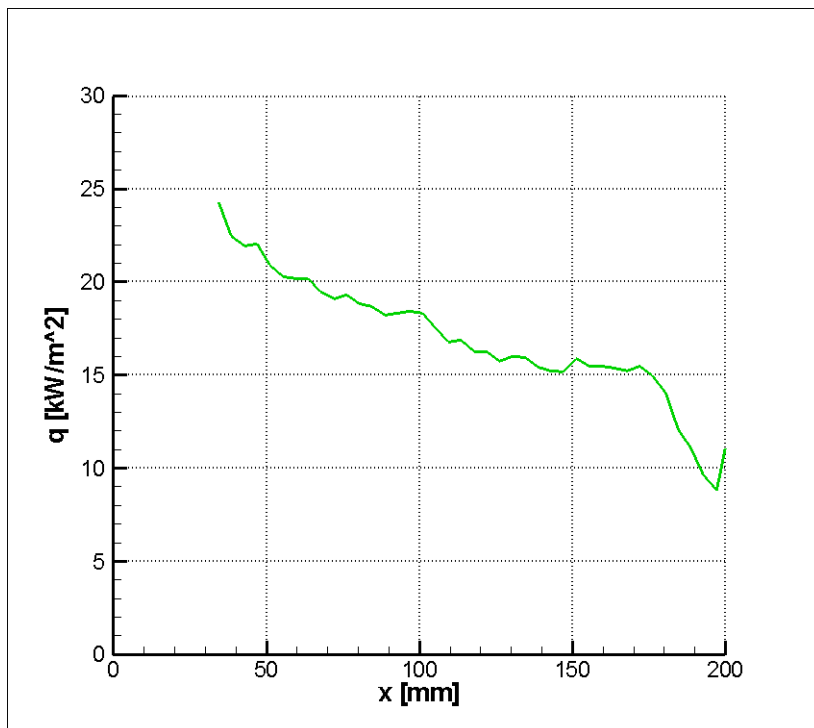
Figure 5.10: 1D temperature diagrams. (a) $t = 14.93$ s, (b) $t = 64.13$ s; these are the same instants of figure (5.9). Reattachment is evident, recirculation is still not marked in (a).

5.8.2 Heat flux maps

Only 1D heat flux have been calculated, and only on the flat plate, as mentioned earlier in this chapter. Figure 5.11 shows the 1D surface heat flux diagrams in the same instant where the temperature diagram of figure 5.10 was shown. It can be seen that the total heat flux decreases during the test, owing to its radiative component, which becomes non negligible as temperatures rise. Figure 5.12, showing the radiative heat flux at the same instants of figures 5.10 and 5.11, confirms this circumstance.

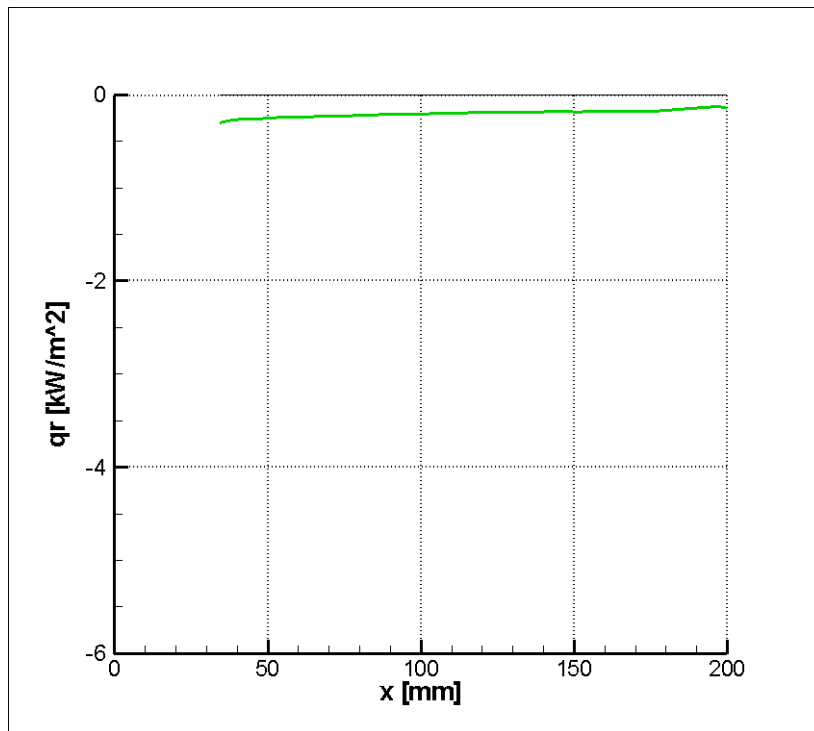


(a)

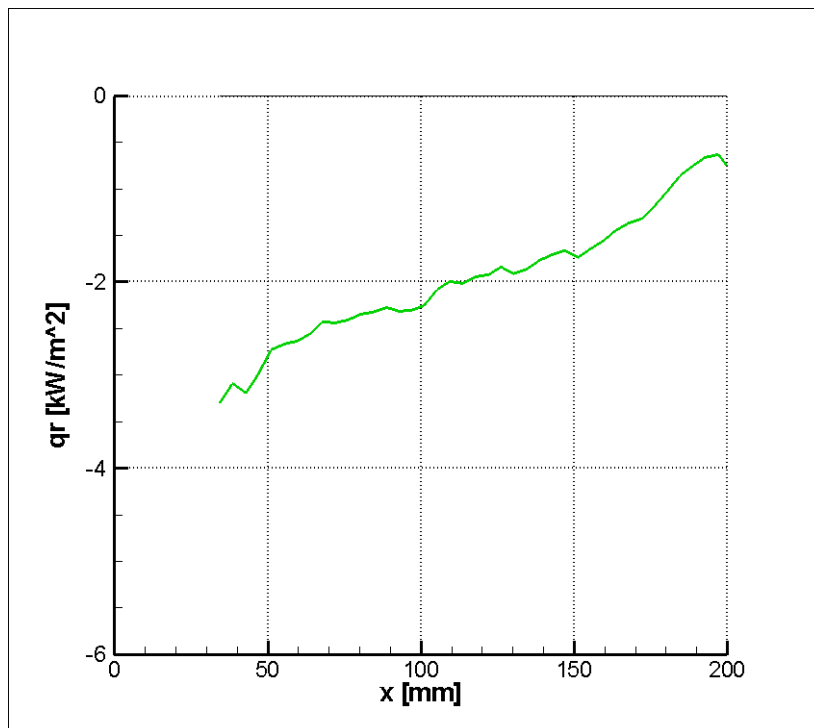


(b)

Figure 5.11: Heat flux maps on the flat plate. (a) $t = 14.93$ s, (b) $t = 64.13$ s; these are the same instants as figure 5.10. It can be seen that the flux decreases during the test, due to radiative effects



(a)



(b)

Figure 5.12: Radiative part of the heat flux. (a) $t = 14.93 \text{ s}$, (b) $t = 64.13$ these are the same instants as figure 5.10. It can be seen that in (a) the radiative flux is still negligible, in (b) it represents about 10% of the total flux

5.8.3 Time history temperature diagrams

In this paragraph a confrontation is shown between experimental and estimated temperature for 1D calculations.

Figure 5.13 shows the measured and the estimated temperature transients for a point on the flat plate.

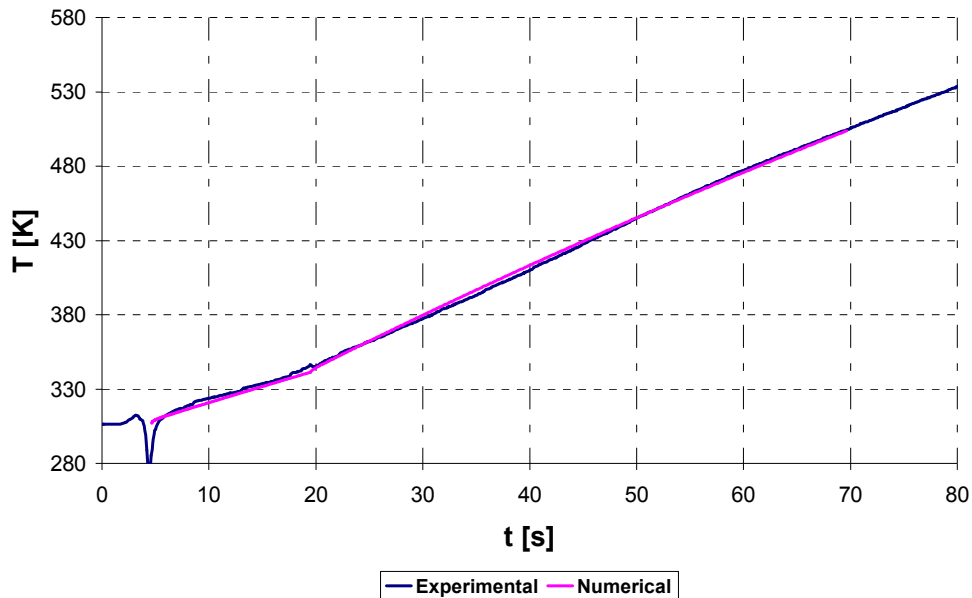


Figure 5.13: Experimental and numerical temperature rises for a point on the flat plate

Keeping in mind that at the beginning of the test surface temperatures are at the lower boundary of the range measurable by the thermograph, and that those measurements are therefore not accurate, it can be seen that the agreement is rather good. Several other interesting points can be noticed:

- 1) The weird evolution of experimental temperature at the beginning of the test is just the model being inserted into the wind tunnel; similarly the rotation can be seen just before $t = 20s$.
- 2) The temperature rise is almost linear, until around $t = 45s$ where radiative effects start to be visible. This linear evolution is typical of a calorimeter body and, infact, because the conductivity of Promasil 1100 is very low (see table 5.2), the only part of the model which ends up being heated is Haynes H25.
- 3) It has been set $t_{imm} = 7s$. As for other experiments, it can be seen how the optimizable parameter *delay* has worked very well.

- 4) The change in h imposed by the rotation is visible both in the experimental and in the numerical diagrams.

As regarding the temperature rises on the flap, the optimization program has not been able to generate any temperature rise resembling the experimental, confirming in this way that a better thermal characterization of the materials, in particular of the substrate of SGL Grade R4340H, would be needed. The experimental temperature rise showed in any case an almost linear evolution, especially in the first 18 s, before the rotation. This circumstance has suggested that the C/SiC might have separated from its substrate; with this suspect in mind, an optimization has been performed using air as a second material under the C/SiC slab. The results are shown in figure 5.14

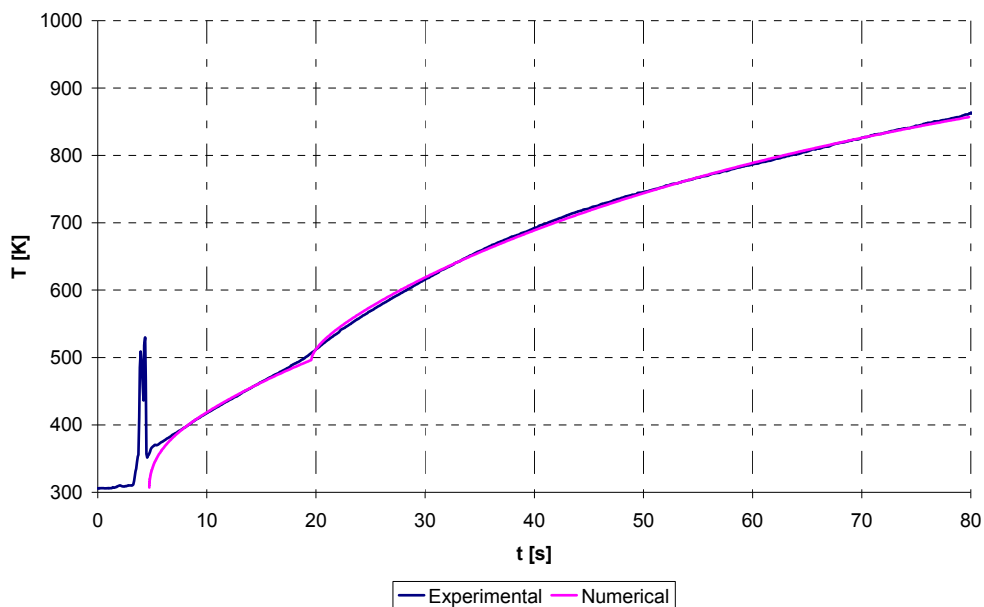


Figure 5.14: Experimental and numerical temperature rises for a point on the flap. The thermal properties of the SGL Grade R4340H have been set to extremely low values, different from those given by the manufacturer

Although the temperature reconstruction in this case is not perfect, there still is a good match, and the suspect that the C/SiC has separated from the metal slab seems to stand on solid grounds.

5.9 Conclusions

A second experimental validation for the heat flux sensor proposed in chapter 3 has been performed. The test has presented some problems especially because of the incomplete thermal and radiative characterization of some of the materials with which the model had been done. Furthermore there is no literature or previous experimental campaigns to compare the results of the estimation.

The experiment has proved to be in any case satisfactory, for several reasons. First of all, the rotation of the model has introduced new experimental difficulties which have been easily overcome both as regarding geometric reconstruction and as regarding heat flux estimation.

The resection algorithm has proven to be very solid and a very powerful method to calculate surface temperatures even in difficult test conditions.

The heat flux sensor, properly updated to deal with the variation in the heat flux coefficient, seems to be working properly, although there are no other solutions to check it against. Even in the case of optimization failure, possibly due to bad thermal characterization of the materials, the use of the optimization program in conjunction with the analysis of numerical temperature rises, has permitted to suggest routes of investigation to try to understand why heat fluxes have been different from expected.

CONCLUSION

A new experimental/numerical technique for the measurement of surface heat fluxes in high enthalpy wind tunnels has been developed and validated.

The transient temperature measurements needed to estimate heat fluxes have been performed by means of infrared thermography coupled by a new method of geometrical reconstruction whose purpose was to establish a precise correspondence between the points on the surface of the model and the points of the IR images. The advantage of using such a technique is twofold. First of all, it allows to calculate the angle of view between the model and the thermograph, allowing in such a way to take into account variations of emissivity with the angle of view ϑ ; such variations are negligible for smaller angles, but they become important when ϑ grows. The implementation of the dependence of emissivity on ϑ allows therefore precise thermographic measurements of surface temperatures even on complex three-dimensional bodies. The second advantage derived by the use of geometrical reconstruction is the possibility to locate on the test model those points in which fluid-dynamics phenomena identifiable by heat transfer measurements occur. For example, the extension of the recirculation zone on a double cone in hypersonic flow (see chapter 4) can be measured and the points of flow separation and reattachment can be located with precision, provided that a thermograph with a sufficiently high spatial resolution is used.

A new heat flux sensor has been proposed, to overcome the problems presented by the sensors currently used (typically, the classical thin film sensor): the high dependence of the sensor on the noise in temperature measurements and the impossibility to know the evolution of surface temperature at the beginning of the test; this latter circumstance is frequently verified in wind tunnel tests, both in those cases in which the model is inserted in the test chamber after the facility has started, and in those cases in which the flow reaches test conditions only after the beginning of the test.

The sensor, differently from others currently used, is based on a simple mathematical description of heat transfer which takes into account two physical parameters of the flow over the model surface; these parameters are the temperature of adiabatic wall T_{aw} (which depends on the stagnation pressure of the flow) and the heat transfer coefficient h . These parameters are estimated in a whole domain optimization process and directly allow to calculate surface heat flux. The use of physical parameters in heat flux estimation allows to numerically generate a meaningful temperature transient in those initial points in which temperature

measurements are not available; this has allowed to have proper heat flux identifications even for relatively high insertion times of the model in the test chamber.

The numerical validation of the sensor of the heat flux sensor has allowed to estimate its precision and limits of applicability. It has been shown that, in presence of the typical noise characterizing modern day thermographs, the heat flux sensor is very accurate, and its precision depends on the adimensional parameters $\pi_1 = h^2 t_p / I$ and $\pi_5 = \sigma \varepsilon T_{aw}^3 / h$, improving as π_1 and T_{aw} increase and as π_5 decreases. It has also been seen that, once an optimal value is reached for π_1 , the accuracy of the optimization doesn't improve any further if π_1 is further increased; this result can be used to infer optimal test durations or appropriate materials for the model. Finally, validations have shown that the sensor is reliable even in presence of higher noise, which in wind tunnel measurements can be related to the functioning of the facility.

It has been seen that when π_1 is too small, typically in short duration facilities and in all those test configuration which imply limited temperature rises, it is not possible to estimate both the parameters mentioned above. In such cases heat flux estimation is still possible and precise, but the single parameter h can be estimated, and an approximated value for T_{aw} must be given in input to the program; it is noted that chosen value for T_{aw} doesn't have effects on the results of the optimization, so it needn't be known with precision; in such situation, an optimal choice for T_{aw} is the stagnation temperature of the flow.

Finally, the effects that insertion time has on optimization has been evaluated, and it has been seen that the results depend on ratio between insertion time and duration of the test. For typical insertion times, which are usually at most 5% of the duration of the test, the sensor has shown a good performance.

The new heat flux sensor has been tested experimentally in two facilities, involving two widely different test configuration

The first experimental tests, illustrated in chapter 4, have taken place in the HEAT wind tunnel at Alta. This is a short duration arc heated wind tunnel. The test campaign was part of a series of test cases within the CAST program run with the purpose of numerically validating a program for the numerical simulation of hypersonic flows in re-entry conditions being developed at CIRA. The test model was a double cone; this geometry has been chosen because it is a classical configuration, implying a wide availability in literature of experimental and numerical results; the test model material and wall thickness have been

chosen to make the semi-infinite wall hypothesis applicable for the typical test durations of about 150 *ms*.

The test configuration has implied a good experimental validation of the heat flux sensor proposed in this work, because of the possibilities to compare results both with literature and with the heat fluxes calculated with thin film sensor on the same temperature measurements. The new heat flux sensor has shown good agreement both with existing literature and with the thin film sensor, showing a higher precision than the thin film sensor. This result is even more remarkable when consideration is given to the particular test conditions, which were characterized by high noise due to the presence of sparkles in the test chamber.

The second experimental test has taken place in the Scirocco Plasma Wind Tunnel at CIRA, and it has been illustrated in chapter 5. The test case was part of the EXPERT program and was performed to study shock wave boundary layer interaction on the full scale EXPERT 20deg flap; both model configuration and model material were therefore those to be used in real flight configuration of the EXPERT capsule. This circumstance presents a big difference from the CAST experiment, where an *ad hoc* designed model has been used, and it has consequently proven to be a good test for the application of the new heat flux sensor. The duration of the test has been of about 80 *s*.

Unfortunately there is no literature against which test results can be compared and, at the moment of writing of this thesis the EXPERT tests are still work in progress. The validity of the new heat flux sensor has therefore been checked, where materials were fully characterized, on the confrontation between the experimental temperature transient and the temperature rise generated numerically using estimated surface heat fluxes. The results, shown in chapter 5, have been encouraging and suggest heat flux estimation has been accurate.

The heat flux measurement technique presented in this work has proven to be accurate and stable and applicable to a wide variety of test configurations and of test facilities.

APPENDIX 1: NUMERICAL SOLUTION OF THE HEAT CONDUCTION EQUATION

The heat conduction problem (3.12)-(3.13) is shown here again:

$$K \frac{\partial^2 T}{\partial x^2} = \rho c_p \frac{\partial T}{\partial t}, \quad (\text{A1.1})$$

$$\text{B.C.} \begin{cases} T(x,0) = T_{wi} \\ K \frac{\partial T(x,t)}{\partial x} \Big|_{x=0} = q_w(t) = h(T_w - T_{aw}) + \sigma \varepsilon (T_w^4 - T_r^4) \\ K \frac{\partial T(x,t)}{\partial x} \Big|_{x=L} = q_L(t) \text{ or } T(L,t) = T_L(t) \end{cases} \quad (\text{A1.2})$$

In equation (A1.1) the coefficients K , ρ and c_p can depend on temperature. The problem (A1.1)-(A1.2) is therefore a non-linear differential equation with non-linear boundary conditions, and needs to be solved numerically.

The space discretization has been accomplished through a classical finite element volume; this method shall not be described here. A clear description, which has been followed by the author, is given in Beck (1985).

The time discretization requires greater attention, because it can be source of errors in the heat flux estimation. The matrix system deriving from the finite volume discretization is:

$$\underline{\underline{M}}(\underline{T}) \cdot \frac{\partial \underline{T}}{\partial t} + \underline{\underline{K}}(\underline{T}) \cdot \underline{T} = \underline{F}(\underline{T}) \quad (\text{A1.3})$$

This system, even if non-linear, could easily be solved with classical methods, as Euler Fully Implicit or Crank Nicholson, provided that Picard sub-iterations are performed within each iteration. With Euler method, for example, to find the solution at time $n+1$ all parameters depending on temperature are calculated using the known temperature at time n . Picard iterations imply the use of the newly calculated temperature to solve the system again and find a new solution for time $n+1$. This process is iterated until the difference between to consecutive temperature calculation is smaller than a given threshold.

Unfortunately the Euler method, although good for solving the direct problem has been found to cause significant bias errors in the estimation of heat flux, unless very little time steps are used, eliminating the advantage of using an implicit method.

The reason for this is to be found in the highly non-linear boundary condition, which can cause significant temperature increases in very small time steps for small times. In this situation tiny time steps are needed also if a second-order method is used.

These errors in early time steps, although go rapidly to zero as time is increased and they are therefore negligible in the calculation of transient temperatures everywhere but in the first few time steps. Unfortunately, as mentioned, these error have been found to be non-negligible when in the optimization process.

To solve this problem without increasing the computational load, a method for adaptive time step control has been implemented. It is the method proposed by Gresho (1980) and it is a predictor-corrector method which uses the difference between the predicted and the correct value to vary the time step for the next iteration. Within each iteration Picard iterations are used.

The method of Gresho uses an Adam Bashfort predictor:

$$\underline{T}_p^{n+1} = \underline{T}^n + \frac{\Delta t_n}{2} \left[\left(2 + \frac{\Delta t_n}{\Delta t_{n-1}} \right) \cdot \dot{\underline{T}}^n - \left(\frac{\Delta t_n}{\Delta t_{n-1}} \right) \cdot \dot{\underline{T}}^{n-1} \right] \quad (\text{A1.4})$$

where the two ‘‘acceleration’’ vectors are calculated from previous iterations by:

$$\dot{\underline{T}}^{n+1} = \frac{2}{\Delta t_n} (\underline{T}^{n+1} - \underline{T}^n) - \dot{\underline{T}}^n \quad (\text{A1.5})$$

The corrector step is an ‘‘inverted’’ Crank-Nicholson:

$$\left[\underline{M}(\underline{T}^a) + \frac{\Delta t_n}{2} \cdot \underline{K}(\underline{T}^a) \right] \cdot \underline{T}^{n+1} = \underline{M}(\underline{T}^a) \cdot \underline{T}^n + \frac{\Delta t_n}{2} \cdot \underline{F}(\underline{T}^a) \quad (\text{A1.6})$$

where the \underline{T}^a are the results of Picard’s iterations and the ‘‘first \underline{T}^a ’’ used in (A1.6) is \underline{T}_p^{n+1} from (A1.4).

The time step is finally updated by:

$$\Delta t_{n+1} = \Delta t_n \left(b \cdot \frac{\varepsilon}{d_{n+1}} \right)^{\frac{1}{3}} \quad (\text{A1.7})$$

where b is a parameter based on the ratio of the two previous time steps, d_{n+1} is a norm of the difference between the predictor and the corrector, and ε is a small number to be set to the wanted value.

It is here noted that the finite volume discretization ultimately leads to a tri-diagonal matrix system, no matter the time discretization technique used. The tri-diagonal system is quickly solved with the well known Thomas algorithm.

The method of Gresho has proven to be very effective with regular temperature rises, but not as much with highly irregular temperature rises like those presented in chapter 4. In these cases Euler method has proved to be more effective. The optimization program includes both methods.

APPENDIX 2: BUCKINGHAM π -THEOREM

In informal terms, Buckingham π -theorem states that:

A physical relationship between some dimensional quantity and several dimensional governing parameters can be rewritten as a relationship between a dimensionless parameter and several dimensionless products of the governing parameters; the number of dimensionless products is equal to the total number of governing parameters minus the number of governing parameters with fundamental dimensions

This formulation is given in very general terms to emphasize that is valid in any consistent system of units. If the SI system is used, the fundamental dimensions are the meter, kilogram, second, ampere and Kelvin (m, kg, s, A, K).

The π -theorem is a precious tool in that it helps to generate sets of dimensionless parameters from the given variables and, as mentioned in the text, it can be used to optimize experimental or numerical work, given its capabilities in reducing the number of parameters to keep under control or to study. Infact, different systems which share the same description in terms of these dimensionless numbers are equivalent.

The choice of the dimensionless parameters is not unique and it is the purpose of dimensional analysis to identify the most “physically meaningful” and the most useful for the experiment being examined

The π -theorem can be used to generate the dimensionless groups for a physical problem even when the equation governing the physical relationship is unknown, provided that the parameters on which the problem depends are properly recognized. Famous examples include the estimation of the mechanical effects of the atomic bomb made by G.I. Taylor only in terms of dimensional analysis and the derivation of the equation of the small oscillations of the pendulum, again only with the help of the π -theorem (Barenblatt, 2003).

For a mathematically rigorous formulation of the theorem, see the original paper from Buckingham (1914). Fascinating descriptions of dimensional analysis in general can be found in Barenblatt (2003), where also the π -theorem is described in detail, and Astarita (1997)

APPENDIX 3: DESCRIPTION OF THE CODE

Several thousands of lines of code in C and in MatLab have been developed in order to implement the readings of data from IR images, the geometrical reconstruction and the heat flux sensor described in this thesis. The estimation of the parameters of the Tsai model described in chapter 2 has been achieved with a code developed at DIAS

A very brief description of the capabilities of the code is given in this appendix.

MatLab code has been implemented to generate a grid on the model and to calculate the whole temperature history starting from the parameters estimated by the Tsai optimization program. Surface temperature can be calculated both on 1-dimensional, 2-dimensional and 3-dimensional surfaces and are saved in TecPlot .plt “time aware” data format.

The code for the heat flux sensor accepts in input both IR images and temperature files in the form of .plt TecPlot “Time aware” data format.

Two methods are used to solve the time-dependent heat conduction equation: the Euler Fully Implicit method and the method proposed by Gresho (1980) and described in Appendix 2.

Both the optimizations routines from Powell (as described in Press, 2007) and Brent (Brent, 1973) have been implemented.

The program gives in output temperature history in 1D and 3D, all the parameters object of optimization, calculation time and values of correlation between measure and estimated temperature rises.

The program is “user friendly” in the sense that all parameters of interest can be set through clear configuration files; for example the one-dimensional mesh including different materials and desired mesh size can be easily input as well as, for example, the tables indicating the variability of K , ρ and c_p with temperature.

Finally, it is possible to use the program just to quickly generate temperature rises with given parameters, to have an idea of how a the modification of a certain parameter influences the temperature evolution, as it has been done in chapter 5

Of course not all experimental condition can be predicted and, as happened in the course of this thesis, future modifications might be needed to implement new experimental challenges. Although such modifications are not straightforward, a certain flexibility has been thought in that two non-used optimizable parameters have been defined and can be easily implemented in the program which generates the temperature rises.

BIBLIOGRAPHY

- ACTON F.S. 1990, *Numerical Methods That Work, corrected edition*. Mathematical Association of America.
- ANDERSON J.D. Jr. 2006, *Hypersonic and High-Temperature Gas Dynamics, 2nd ed.*, Prentice Hall.
- ASTARITA G. 1997, Dimensional analysis, scaling, and orders of magnitude, *Chemical engineering Science*, **52** (24), 4681-4698.
- ASTARITA T., CARDONE G. & CARLOMAGNO G.M. 2006, Infrared thermography: An optical method in heat transfer and fluid flow visualization, *Optics and Lasers in Engineering* **44** (3-4), 261-281.
- BARENBLATT G.I. 2003, *Scaling*, Cambridge University Press.
- BECK J.W. 1985, *Inverse Heat Conduction. Ill-posed Problems*. Wiley-Interscience
- BOYD C.F. & HOWELL A. 1994, Numerical investigation of one-dimensional heat-flux calculations, *NWSCDD/TR-94/114*, Naval Surface Warfare Center Dahlgren Division.
- BRENT R.P. 1973, *Algorithms for Minimization without Derivatives*. Prentice Hall.
- BUKINGHAM E. 1914, On physically similar systems; illustrations of the use of dimensional equations, *Physical Review*, **4**, 345-376.
- CARDONE G. 2007, IR heat transfer measurements in hypersonic plasma flows, *QIRT Journal*, **4**, 233-251.
- CARDONE G., DISCETTI S. & DELLO IOIO G. 2008, Reconstruction of 3D surface temperatures from IR images, *QIRT 2008, 9th International Conference on Quantitative InfraRed Thermography*, Krakow, 2-5 July 2008.
- CAREDDA P., PASSARO A., BACCARELLA D., CARDONE G. & DELLO IOIO G. 2008, Experimental results on a sharp double cone in a Mach 9 non-equilibrium flow, *6th European Symposium on aerothermodynamics for Space Vehicles*, Versailles, 3-6 November 2008.
- CARSLAW H.S. & JAEGER J.C. 1959, *Conduction of Heat in Solids, 2nd ed.*. Oxford University Press
- COOK W.J. & FELDERMAN E.J. 1966, Reduction of data from thin film heat transfer gauges: a concise numerical technique, *AIAA Journal* **4** (3), 561-562.
- COSNIGNY H. & LE SANT Y. 1990, Détermination des échauffements cinétiques sur maquettes en souffleries par la méthode des températures superficielles, *Journées d'études, Mesures de Températures*, Paris, 19-20 juin 1990.
- DE FILIPPIS F., CARISTIA S., DEL VECCHIO A. & PURPURA C. 2001, The Scirocco facility: Qualification phase, *2nd International Symposium on Atmospheric Re-entry Vehicles and Systems*, Arcachon, 26-29 March 2001.
- DE FILIPPIS F., CARISTIA S., DEL VECCHIO A. & PURPURA C. 2001, The Scirocco PWT facility calibration activity, *3rd International Symposium on Atmospheric Re-entry Vehicles and Systems*, Arcachon, 24-27 March 2003.
- DE LUCA L., CARDONE G., DE LA CHAVALERIE D.A. & FONTENEAU A. 1995, Viscous Interaction Phenomena in Hypersonic Wedge Flow, *AIAA Journal* **33** (12), 2293-2298.

- DI CRISTINA V. 1970, Three-Dimensional Laminar Boundary-Layer Transition on a Sharp 8° Cone at Mach 10, *AIAA Journal*, **8** (5), 852-856.
- DRUGUET M.C., CANDLER G.V. & NOMPELIS I. 2005, Effect of Numerics on Navier-Stokes Computations of Hypersonic Double-Cone Flows, *AIAA Journal*, **43** (3), 616-623.
- FAY J.A. & RIDDELL F.R. 1958, Theory of Stagnation Point Heat Transfer in Dissociated Air, *Journal of the Aeronautical Sciences* **25** (2), 73-85.
- GAITONDE D.V., CANUPP P.W. & HOLDEN M.S. 2002, Heat Transfer Predictions in a Laminar Hypersonic Viscous/Inviscid Interaction, *Journal of Thermophysics and Heat Transfer*, **16** (4), 481-489.
- GIORDANO R. & ASTARITA T. 2008, Spatial resolution of the Stereo PIV technique, *Experiments in FLuids*, published online.
- GRESHO P.M. & LEE R.L. 1980, On the Time-Dependent Solution of the Incompressible Navier-Stokes Equations in Two and Three Dimensions, in *Recent Advances in Numerical Methods in Fluids, Vol. 1*. Pineridge Press.
- HOLDEN M.S. & WADHAMS T.P. 2001, Code validation study of laminar shock / boundary layer and shock/shock interactions in hypersonic flow. Part A: experimental measurements, *AIAA Paper 2001-1031A*.
- HOLDEN M.S. 2000, Experimental Studies of Laminar Separated Flows induced by Shock Wave/Boundary Layer and Shock/Shock Interaction in Hypersonic Flows for CFD validation, *AIAA Paper 2000-0930*.
- HOLLIS B.R. 1995, User's Manual for the One-Dimensional Hypersonic Experimental Aero-Thermodynamic (1DHEAT) Data Reduction Code, *NASA CR-4691*.
- LEVENBERG, K., 1944, A method for the solution of certain Problems in least squares, *Quarterly of Applied Mathematics*, **2**, 164-168.
- MARQUARDT D., 1963, An algorithm for least-squares estimation of nonlinear parameters, *SIAM Journal of Applied Mathematics*, **11**, 431-441.
- MUYLAERT J. et al. 2003, EXPERT System Requirement Documents (ESRD), *TOS-MPA/2745/JM Is. 2, Rev. 0*.
- NOMPELIS I., CANDLER G.V. & HOLDEN M.S. 2003, Effect of Vibrational Nonequilibrium on Hypersonic Double-Cone Experiments, *AIAA Journal*, **41** (11), 2162-2169.
- PRESS W.H., Teukolsky S.A., Vetterling W.T. & Flannery B.P. 2007, *Numerical Recipes, 3rd ed.*. Cambridge University Press.
- SCHETTINO A., BATTISTA F., RANUZZI G. & D'AMBROSIO D. 2008, Rebuilding of new experimental tests on a double cone at Mach 9, *6th European Symposium on aerothermodynamics for Space Vehicles*, Versailles, 3-6 November 2008.
- SIMEONIDES G. 1992, Hypersonic shock wave boundary layer interaction over compression corners, PhD Thesis, University of Bristol.
- SIMEONIDES G., HAASE W. & MANNA M. 1994, Experimental, Analytical, and Computational Methods Applied to Hypersonic Compression Ramp Flows, *AIAA Journal*, **32** (2), 301-310
- TSAI R.Y., 1987, A Versatile Camera Calibration Technique for High Accuracy 3D Machine Vision Metrology Using Off-the-Shelf TV Cameras and Lenses, *IEEE Journal of Robotics and Automation*, **RA-3** (4), 323-344.

- VAN DRIEST, F.R. 1952, Investigation of Laminar Boundary Layer in Compressible fluids using the Crocco method, *NACA TN 2597*, 1952.
- WADHAMS T.P. & HOLDEN M.S 2004, Summary of experimental studies for code validation in the LENS facility and comparison with recent NS and DSMC solutions for 2D-3D separated regions in hypervelocity flows, *42nd AIAA Aerospace Sciences Meeting and Exhibit*, Reno 5- January 2004, *AIAA Paper 2004-0917*.
- WILLERT C. 2006, Assessment of camera models for use in planar velocimetry calibration, *Experiments in Fluids*, **41**, 135-143.
- WRIGHT M.J., SINHA K. & OLEJNICZAK J., MAGRUDER T.D. & SMITS A.J. 2002, Numerical and Experimental Investigation of Double-Cone Shock Interactions, *AIAA Journal*, **38** (12), 2268-2276.